Approaches to Fines Production in the Walloons Subgroup, Surat Basin, Queensland

Leslie George Jenkinson

The Australian School of Petroleum

THE UNIVERSITY of ADELAIDE

This thesis is submitted in fulfilment of the requirement for the degree of

Master of Philosophy

in the Faculty of Engineering, Computer and Mathematical Sciences

List of Symbols

P_p	pore pressure
P_h	hydrostatic pressure
P_w	wellbore fluid Dowla et al. pressure
ΔP	difference between wellbore and pore pressure
P_f	fracture initiation pressure
g	acceleration due to gravity
z	depth
σ	applied stress tensor
σ'	effective stress tensor
σ_1	maximum principal stress
σ_2	intermediate principal stress
σ_3	minimum principal stress
σ_{ij}	stress component acting in the j direction in the plane normal to the i direction
σ_n	normal stress
σ_m	mean applied stress
σ_m'	mean effective stress
σv	vertical stress
σ_{Hmax}	maximum horizontal stress
σ_{hmin}	minimum horizontal stress
σ_{rr}	effective radial stress
$\sigma_{\theta\theta}$	effective circumferential stress
σ_{zz}	effective axial stress
σ_{tmax}	maximum effective stress tangential to the wellbore wall
σ_{tmin}	minimum effective stress tangential to the wellbore wall
φ	friction angle (º)
τ	shear stress
τ_{max}	maximum shear stress
τ_0	cohesive strength
$\tau_{\theta Z}$	tangential shear stress
ρ	density
ρ_f	fluid density
ρ_b	bulk density
ρ_{ma}	matrix density
Φ	shale porosity
Φ_{RHOB}	shale porosity estimated from the density log
$\Phi_{\Delta t}$	shale porosity estimated from the sonic log
Φ_{norm}	porosity of normally compacted shale
C_p	correction factor for the Wyllie time average equation
Δt	measured interval transit time
Δt_f	pore fluid interval transit time
Δt_{ma}	matrix interval transit time
Δt_{norm}	interval transit time of normally compacted shale
x	Eaton (1972) exponent
θ	angle around the wellbore wall relative to σ_{Hmax}
ω	angle between σ_{tmax} and the borehole axis
μ	coefficient of friction
C	compressive rock strength
C_0	unconfined compressive rock strength
C'	cohesion values (psi)
T	tensile strength
ν	Poisson's ratio

Abstract

This study characterises the root causes for fines generation in coal seam gas wells in the Walloons Subgroup of the Surat Basin, southeast Queensland, Eastern Australia. Fines production can be critical in causing erosion in downhole pumping equipment and disruption to surface facilities. The Surat Basin has, in places, exceptional coal permeabilities (>1 Darcy), and most high permeability wells are completed with pre-perforated liners. Fines that are captured in separators are usually generated from the interburden lithologies, not from coals (reservoir rocks).

Fines production characterisation and mitigation generically requires identification of the processes that lead to breakdown of cohesion in rocks that generate fines. Conventionally, fines production is dealt with using a geomechanical approach to understand the interaction of rock strength and in situ stresses in the context of reservoir production conditions. Significant factors that may control fines production are in-situ stresses, rock strength, drawdown and depletion as well as completion type and geometry. Geomechanical models were developed from log based, strain derived stress models, which are calibrated to rock strength testing of the core samples. Interestingly, fines production remains prevalent in areas with low differential stress and little variability in other parameters, such as flowing bottom hole pressure (FBHP).

Tests exposing interburden rocks to produced formation water were used to understand rock weakening, as well as a comprehensive program of mineralogy (XRD) and rock fluid sensitivity testing on selected sandstone, siltstone and mudstone core samples. Each sample was photographed initially dry (i.e., in its original state), and then in contact with synthetic brine or various clay stabiliser solutions, in order to qualitatively evaluate the change in both rock strength and stability over the duration of fluid exposure. Results suggest that volcanogenic sediments contribute to fines production in fields in the Walloons Subgroup. The results of the work presented here help to identify completion strategies, go forward development and future production optimisation opportunities.

Thesis Declaration

I certify that this work contains no material which has been accepted for the award of any other degree or diploma in any university or other tertiary institution and, to the best of my knowledge and belief, contains no material previously published or written by another person, except where due reference has been made in the text. In addition, I certify that no part of this work will, in the future, be used in a submission for any other degree or diploma in any university or other tertiary institution without the prior approval of the University of Adelaide and where applicable, any partner institution responsible for the joint-award of this degree.

I give consent to this copy of my thesis when deposited in the University Library, being made available for loan and photocopying, subject to the provisions of the Copyright Act 1968.

The author acknowledges that copyright of published works contained within this thesis resides with the copyright holder(s) of those works.

I also give permission for the digital version of my thesis to be made available on the web, via the University's digital research repository, the Library catalogue and also through web search engines, unless permission has been granted by the University to restrict access for a period of time.

Leslie George Jenkinson Date

Acknowledgements

I am extremely appreciative to my principal supervisor A/Prof. Mark Tingay (Australian School of Petroleum, Adelaide University) and industry supervisor, Dr Thomas Flottmann (Origin Energy). I am grateful for their feedback, guidance and patience to complete this thesis, having benefitted from both supervisors' interest and encouragement.

Thanks to all the staff at the Australian School of Petroleum. I am indebted to Professor Peter McCabe as well as the Post Graduate Coordinators Dr Simon Holford and Dr Kathryn Amos for overcoming the difficulties associated with a remote and part time student.

Thank you to Origin Energy for allowing me the opportunity to study part time as well as providing the resources and data necessary to complete the thesis. I am very grateful for the technical assistance from Andrew Aouad, Sam Brooke-Barnett, Brett Pidgeon and Amanda Murphy. Thank you to Steve Pickard for drafting figures.

I would also like to thank Dr Scott Mildren and Dr Jerry Meyer from Ikon Science for their assistance to understand and model the results of the core analysis. Thank you to Brian Lee from Geolog (Paradigm) who assisted me with the petrophysical interpretation and Multimin analysis.

Thank you to the examiners, A/Prof. Gideon Rosenbaum and Dr Dave Dewhurst. Thank you both for your time to review the thesis and provide detailed feedback which has helped improve my work.

Last but by no means least, I would like to thank my wife Elena and my son Lachlan. Without their love, understanding and encouragement, none of this would have been possible.

Chapter 1 - Introduction

1.1 Objectives of Work

Coal Seam Gas (CSG) has been produced from the middle Jurassic Walloons Subgroup (WSG) in the Surat Basin, Queensland for around 10 years. WSG CSG production is often accompanied with generation of 'fines' from clastic successions, which form the interburden of the coal measures. Fines production is evident in the deposition of fine-grained sediment in separators (Figure 1) during both the initial dewatering phase of CSG production and later gas production itself. Analysis of the sediment in the separators was compared to analysis from core and showed a difference in grain size and composition. The objective of this work is to understand fines producing mechanisms and root causes with a view to offer fines mitigation strategies for ongoing and future CSG development.

The work presented here uses subsurface data to analyse the depositional environment, rock composition and geomechanical properties to evaluate the Surat Basin succession units in the context of fines production. Based on the results from this work, recommendations for completion strategies can be made to mitigate fines generation during CSG production.

1.2 Fines Production

Productivity decline is often observed in gas wells producing reservoir fines (Zeinijahromi et al. 2012). Root causes of fines production in many reservoirs are analysed in a geomechanical context, including examination of rock strength and flowing bottom hole pressures, ambient tectonic stresses, stress and pore pressure changes due to reservoir depletion, as well as fluid compatibility (Zoback, 2007; Rahmati et al., 2013; Khaksar et al., 2015). There is a dearth of published work on geomechanics and fines production in the Surat Basin that focuses on the WSG. The aim of this work is to understand the root causes of fines production as well as the interaction and impact on fines production of rock properties and geomechanical attributes in key lithologies or facies of the WSG.

Figure 1: Fines produced from Condabri South 19 which has accumulated in the separator.

Fines production is obviously manifest in separators in some WSG wells (Figure 1). Increased fines production has led to additional wearing of equipment and premature reduction in the life of downhole equipment and surface facilities, thus impacting productivity and profitability of wells. Interestingly, fines production in WSG is also observed in non-producing wells with static fluid columns. This observation is exemplified from three separate caliper runs in a well over a three year period to measure the degradation of the wellbore over time (Figure 2). The initial caliper run was conducted for the initial open hole evaluation. The logging tools made TD (937.71 mRT) without hindrance and the caliper measured the wellbore to be in gauge. A second caliper run was conducted after approximately 18 months and tagged fill at 835.78 mRT. After a further 14 months (approximately three years after drilling), a third caliper run was conducted which tagged fill at 711.00 mRT. The third caliper was a four arm caliper, which also gives the geometry of the disaggregation of the wellbore.

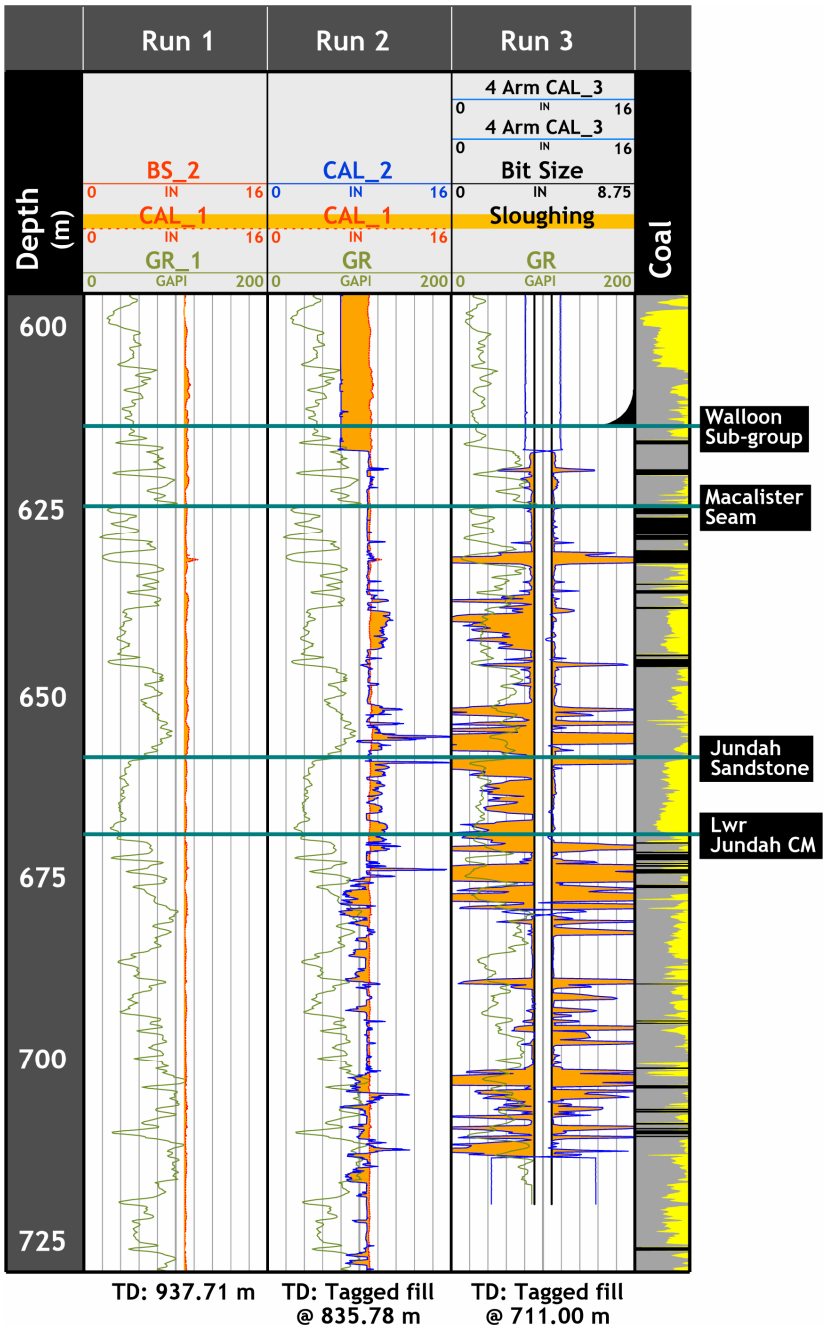

Figure 2: Three caliper runs of a WSG well showing the disaggregation of the wellbore over an approximately three-year period. Run 1 was made shortly after drilling, run 2 was made at approximately 18 months after drilling, and run 3 was made at approximately 32 months after drilling.

1.3 Fines production mechanisms

In the context of this work, ‘fines’ are understood to be small grainsize, disintegrated rocks. Other workers refer to similarly disintegrated rocks as solids (production) or sanding (if the disintegrated rock product is mainly made up of sand). WSG ‘fines’ are mainly clay-like components, which occur predominantly in the interburden.

Fines production may reduce overall well production. It may also cause erosion in downhole pumping equipment and cause disruption to surface facilities (Qui et al. 2006). Significant factors that may lead to fines production are stresses, rock strength, flowing bottom hole pressure (FBHP) and depletion. The completion type and geometry may also lead to fines production (Qui et al. 2006).

The formation of fines or solids (in the broader sense) indicate production disintegration i.e. a reduction in strength that ultimately results in fines. Rock strength depends on the interaction between extrinsic and intrinsic factors.

The most important extrinsic factors governing rock strength are confining pressure, strain rate and, to a lesser extent, temperature. Important intrinsic geologic factors include porosity, grain size, mineralogical rock composition and types of cement. Porosity, clay content and the degree of cementation all have a significant influence on the unconfined compressive strength of clastic rocks (Plumb 1994).

Fines production characterisation and mitigation is classically dealt with from a geomechanical point of view to understand the interaction of rock strength and in situ stresses. Understanding the current state of stress is fundamental for a comprehensive geomechanical model and reservoir production. There may be beneficial or detrimental effects to production due to depletion in the reservoir caused by changes to the stress state (Zoback 2007).

XRD analysis of the sediments in the separators showed a difference to the same analysis from the core. These data do not correlate due to clays in solution and the related variation in grain size distribution.

The present properties of a sedimentary rock are determined by the entire cycle from erosion of rock fragments to transportation, deposition, compaction, lithification and exhumation. Some knowledge of these processes is therefore valuable when trying to assess the mechanical properties of a rock (Fjaer et al. 2008). Evaluating rock composition and rock strength from geophysical measurements is fundamental to the analysis of rock strength associated with fines production (Plumb 1994). Specifically, the evaluation of wireline logs can be helpful in attempting to understand and even predict rock mineralogy and the potential of rocks to disintegrate to produce fines.

1.4 Outline and structure of this work

Guided by key observations presented above, this work has been structured as follows:

1. Geological summary (Chapter 2): Geological context and background of the volcanic influence to sedimentation.
2. Rock Dissolution and stabilisation analysis (Chapter 3): Highlights likely key rock-disintegration mechanism from the saturation effects on rock integrity.
3. Core facies log and petrographic analysis (Chapter 4): Shows the depositional models from core facies to understand if disintegration is facies related.
4. Petrophysical analysis (Chapter 5): This chapter looks at various methods of calculating v-shale and incorporates XRD core data and ECS wireline data to identify any petrophysical parameters controlling disintegration.
5. Rock strength testing (Chapter 6): Incorporating various rock strength testing methods with fluid saturation.
6. Geomechanics (Chapter 7): To identify a stress - rock strength influence from image log analysis and stress profiles to combine the rock strength data with regional trends.
7. Discussion, implications and conclusions (Chapter 8).

Chapter 2 - Geological Summary

2.1 Tectonic Framework

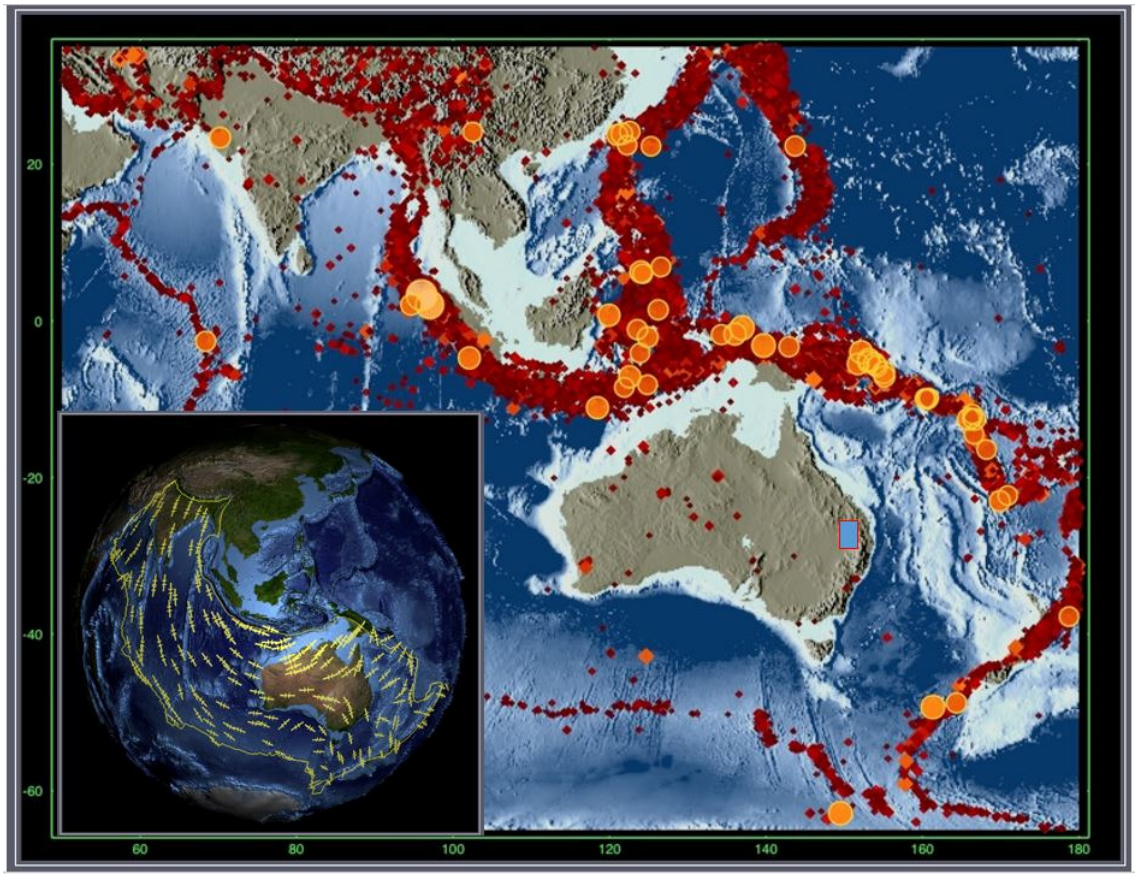

Figure 3: The Indo-Australian Plate and surrounding plate margins. The plate margins are identified as red circles displaying seismicity. The study area is highlighted in blue in eastern Australia. The Australian continent sits within the Indo-Australian Plate and is moving north to north-northeast. Adapted from Sandiford 2016.

The present-day Australian continent is bracketed by the Indo-Australian Plate and is moving north to north-northeast at a rate of ~56mm/year (Figure 3, Sandiford 2016). Unlike most major tectonic plates, the absolute motion of the Australian plate is not parallel with the intracontinental stress orientations (Richardson, 1992; Rajabi et al., 2017).

The regional pattern of stress orientation in the Australian continent is consistent with a first order control being exerted by plate-boundary forces (Hillis and Reynolds 2003). However there are complex local anomalous stress orientations which are influenced by second and third order sources of stress such as structure, topography, pre-existing structural grain and density heterogeneities (Hillis and Reynolds, 2003; Rajabi et al., 2017).

During the Permian and Triassic, eastern Australia was part of an active convergent plate margin on Gondwanaland (Korsch et al. 2009b). Initial extension formed significant half-graben structures which were subject to compressional deformation during the mid-Cretaceous deformation that fragments the Surat Basin into a number of remnant basins (Elliott 1993). This dominant structural style was thrusting from the east, and is considered to contribute to the initial uplift that has given rise to the present basin outlines. The following gives a brief outline of the tectonic development and key structural elements of Eastern Australia.

2.2 Basement

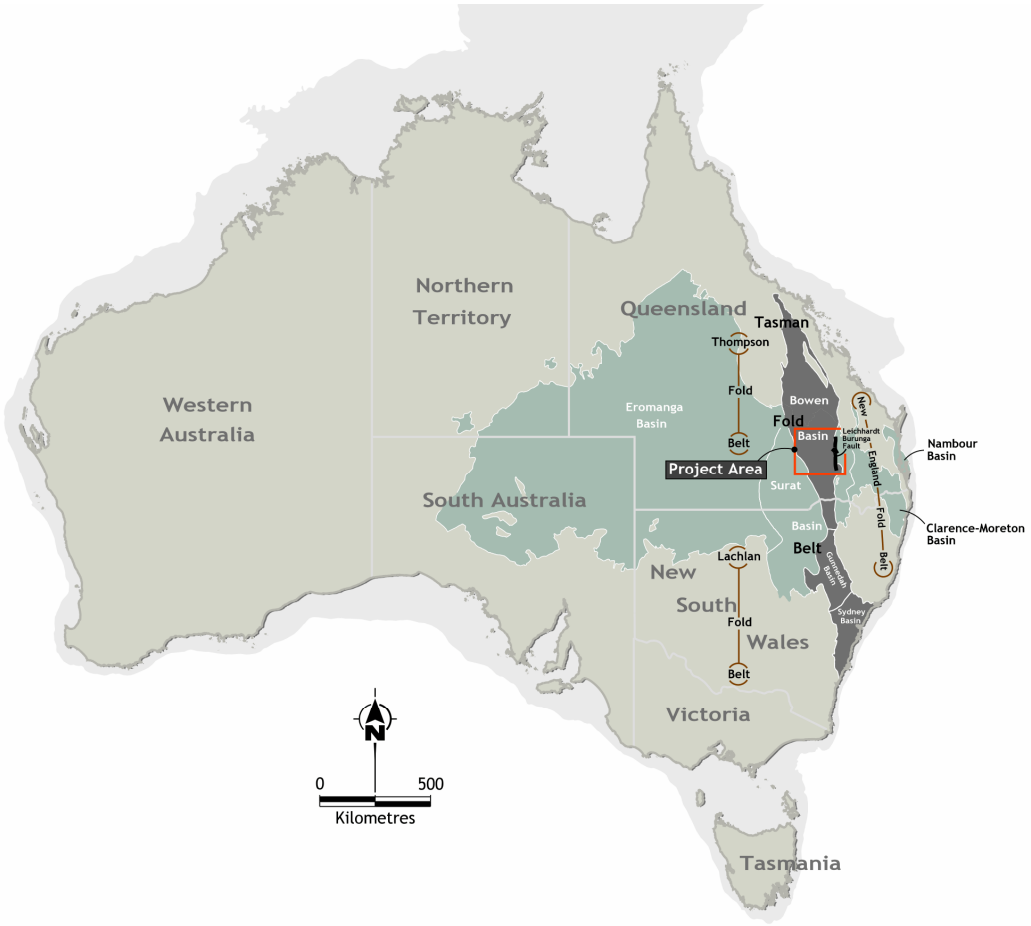

Figure 4: Major tectonic elements and framework of the Bowen and Surat Basins as part of the Tasman Fold Belt System which occupies the eastern third of the Australian continent. The New England Fold Belt is the easternmost and youngest part of the Tasman Fold Belt System. The Thompson Fold Belt System and the Lachlan Fold Belt System are separated from the New England Fold Belt System by the Gunnedah-Sydney Basin. Adapted from Murray (1997); Cook and Draper (2013); Jell et al (2013).

The basement rocks that underlie the Bowen and Surat Basins are part of the complex Tasman Fold Belt System and occupy the eastern third of the Australian continent (Figure 4). The New England Fold Belt is part of a Devonian-Carboniferous subduction (Figure 5) and is the easternmost and youngest part of the Tasman Fold Belt System. The Thompson Fold Belt and the Lachlan Fold Belt Systems are

separated from the New England Fold Belt System by the Permian age Bowen-Gunnedah-Sydney Basin (Murray 1997). The New England Fold Belt (Figure 4) consists of arc and arc related rocks produced by plate convergence which originated in the Late Devonian and continued until the Early Cretaceous (Korsch et al., 2009; Waschbusch et al., 2009).

During the Mid-Devonian, central eastern Queensland was close to the eastern margin of Gondwana, with the contemporaneous coastline located in a more stable interior of the craton than it is today (Caritat and Braun 1992). A Late Devonian arc collided with the continent (Figure 5) resulting in a reversal of subduction direction and the formation of a west dipping subduction zone along a convergent margin on the eastern edge of Gondwana (Donchak 2013).

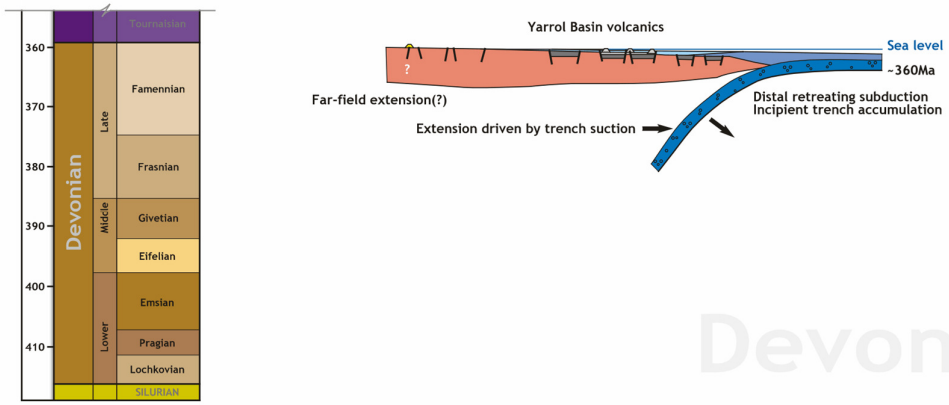

Figure 5: The tectonic evolution during the Devonian in the northern New England Orogen as part of the Tasman Fold Belt System. The extension event was driven by trench subduction along a convergent margin on the eastern edge of Gondwana (Donchak 2013). Adapted from Holcombe (2013).

The Kanimblan Orogeny formulated an accretionary wedge during the extension phase of the mid-Carboniferous (Figure 6). During the Pennsylvanian to early Permian, Eastern Gondwanaland was dominated by a back-arc extension, creating a number of sedimentary basins within the New England Orogen accretionary belt (Donchak 2013).

The Timbury Hills Formation and Roma Granites have been identified as the two prominent basement units in the area. The Combarngo Volcanics are considered petroleum economic basement although they are actually the basal unit of the Bowen Basin succession (Murray 1997).

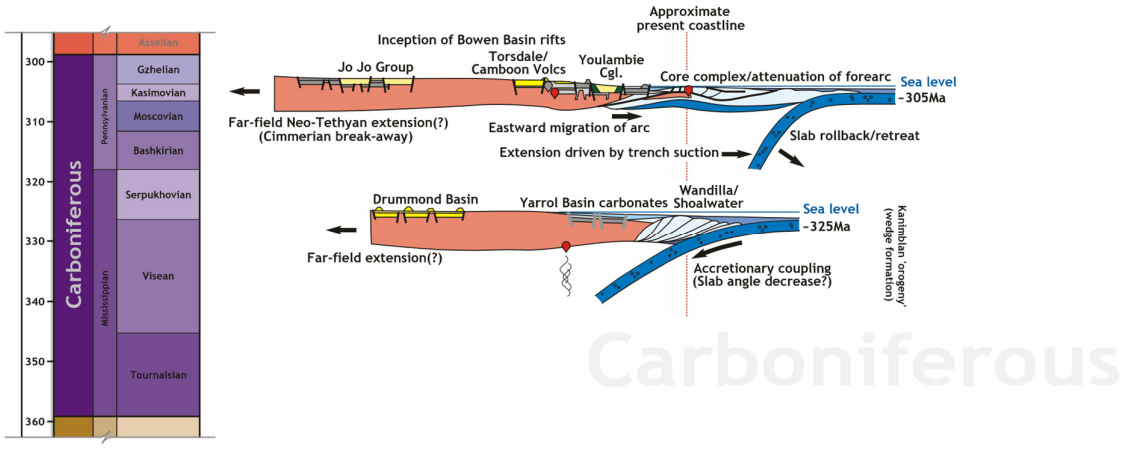

Figure 6: Following earlier accretion, the late-Carboniferous was an extensional phase. Accretionary coupling and slab rollback led to extension and the inception of the Bowen Basin rifts. The Pennsylvanian to early Permian transition involved a back arc extension of a number of sedimentary basins within the New England Orogen accretionary belt. Adapted from Donchak (2013); Holcombe (2013).

2.3 Basin Setting – Bowen Basin

The Bowen Basin forms the northern extension of the Bowen-Gunnedah-Sydney Basin system in eastern Australia. The southern part of the Bowen Basin is covered by the mid-Jurassic Surat Basin in Queensland (Figure 7). Sedimentary rocks of shallow marine and terrestrial origin and volcanics of Permian-Triassic age compromise the Bowen Basin, which obtain thicknesses up to 10 km in the Taroom and Denison Troughs (Green et al. 1997).

In the Early Permian, subsidence was driven by extensional tectonics. The extension and initial rapid subsidence formed a series of half-grabens, resulting in widespread Bowen Basin rifting (Draper, 2013). The half-grabens were formed along the western margin of the Bowen and Gunnedah Basins (Figure 8) (Korsch and Totterdell 2009). Korsch et al (1998) identified this as the Denison Event. Half-graben development occurred in a small number of separated troughs that have allowed fluviolacustrine sediments (including coal) to accumulate (Brakel et al. 2009). The rifting ceased around 280 Ma and was succeeded by a phase of passive thermal subsidence that resulted in more widespread, uniform sedimentation (Korsch and Totterdell 2009).

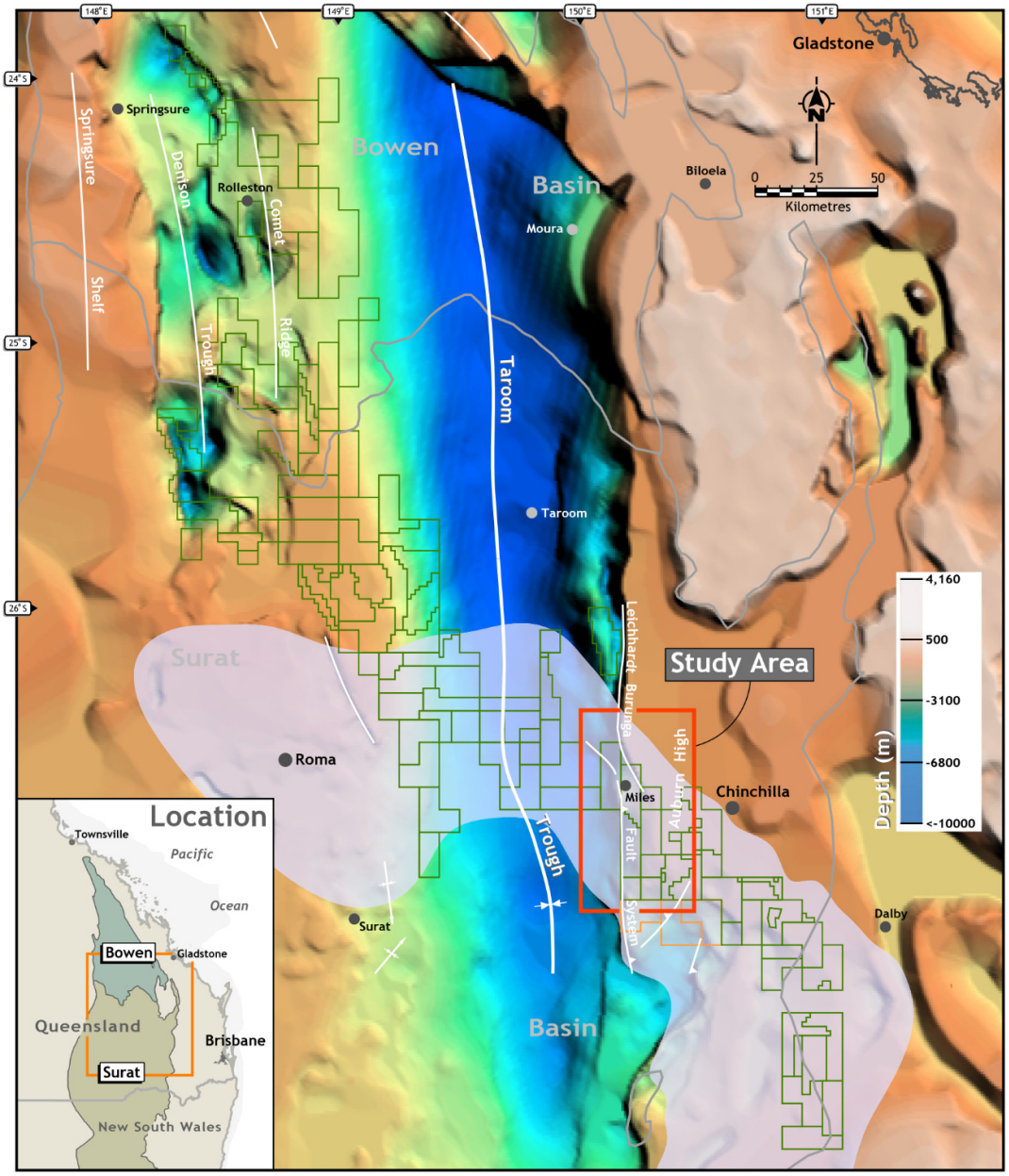

Figure 7: Structural elements of the Bowen Basin with the overlying mid-Jurassic Surat Basin sediments to the south. The Taroom Trough is shown in blue corresponding to depth. The background image is the OzSEEBASE™ (2005) to basement. The SEEBASE maps used throughout this study show an approximate depth to basement. The maps are useful to depict the overall basement structures as they are based on multiple data sets.

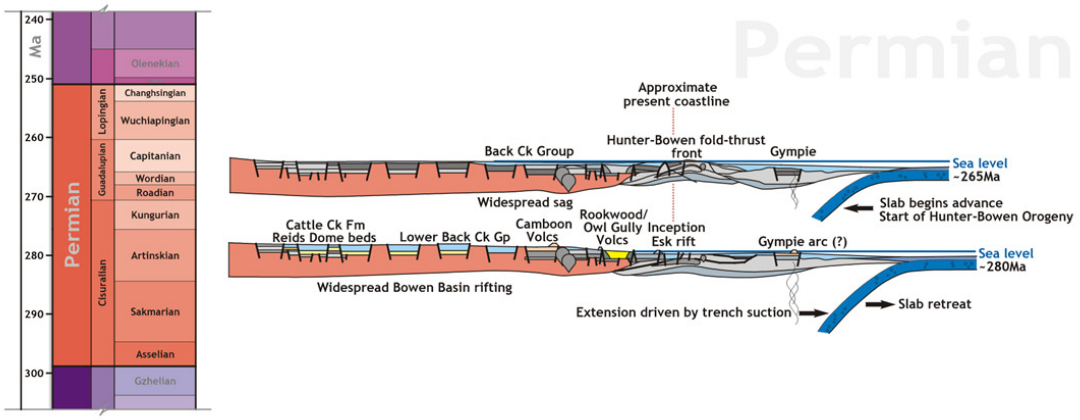

Figure 8: The Early Permian extensional phase was driven by trench suction, which caused widespread rifting. The extensional phase developed a series of half-grabens. The Late Permian saw the slab advancing which begins the Hunter-Bowen Orogeny as a contractional event (Donchak 2013). Adapted from Holcombe (2013).

During the Hunter-Bowen Orogeny (ca 265 Ma to ca 230 Ma), rocks in the New England Orogeny, including the lower Permian rift-related sedimentary rocks, were subject to multiple episodes of contractional deformation (Holcombe et al. 1997; Korsch et al. 2009b). The passive thermal subsidence phase at the start of the Late Permian was interrupted by the onset of lithospheric flexure due to convergence and thrust loading to the east in the New England Orogen which resulted in a foreland basin (Korsch and Totterdell 2009). In the Denison Trough, the local rift development, as well as the volcanism in the Taroom Trough, was followed by a period of thermal subsidence, and then by a phase of subsidence driven by foreland loading (Figure 9) (Brakel et al. 2009).

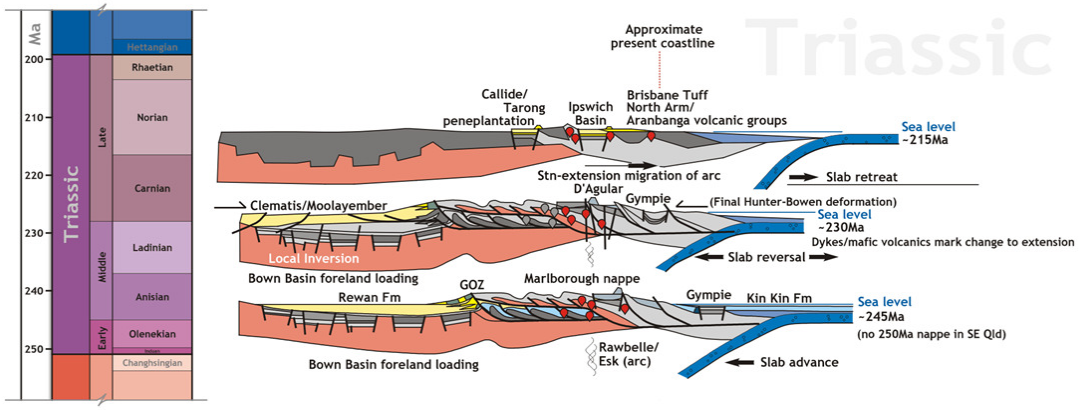

Figure 9: The tectonic evolution during the Triassic. Slab advancement has continued from the Late Permian with the Bowen Basin foreland loading. Adapted from Holcombe (2013).

During the Middle-Late Triassic (Figure 9) a major compression deformation event (referred to as the Goondiwind Event by Korsh et al., 1998; Korsch et al., 2009b) occurred that resulted in regional uplift, folding and the erosion of up to 3000 m of section (Fielding et al. 1990). This event was also responsible for the activation and reactivation of a series of reverse faults on the western margin of the New England

Orogen. Extensive erosion and peneplanation during the Middle to Late Triassic was followed by deposition of the Surat Basin in the Early Jurassic to Early Cretaceous (Waschbusch et al. 2009).

The depositional histories of the Bowen Basin and Surat Basin are subdivided into several basinal phases (Figure 10). From the regional tectonic summary, the Bowen Basin was deposited during a periods of mechanical extension, passive thermal subsidence and foreland crustal loading, whilst the overlying Surat Basin was deposited during periods of thermal subsidence and flexure (Korsch et al. 2009a).

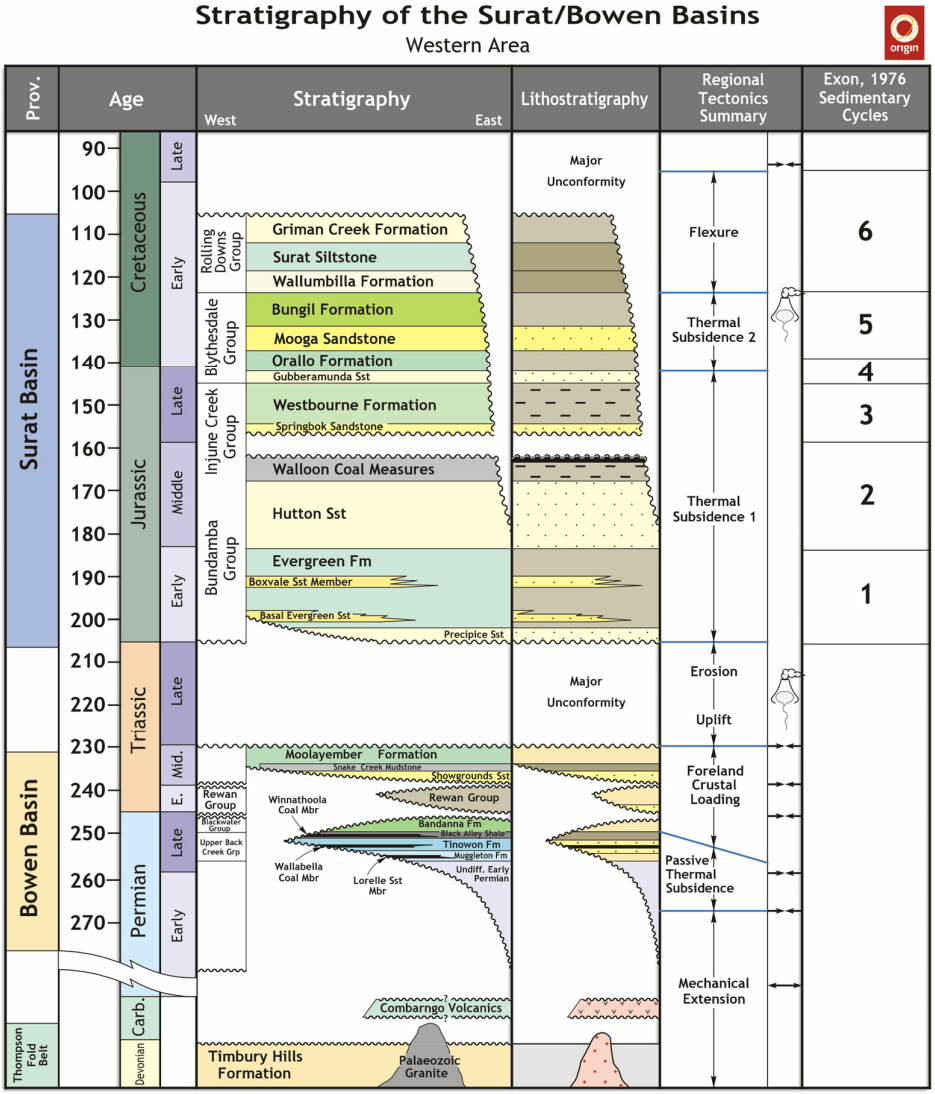

Figure 10: The stratigraphy and lithostratigraphy of the western area Bowen and Surat Basins which show the relationships between lithostratigraphy, sedimentary cycles and regional tectonic events. Adapted from Exon, (1976); Korsch et al (2009a).

2.4 Basin Setting - Surat Basin

The Surat Basin is part of the large inland Queensland basins that make up the main part of the Great Australian Superbasin (Jell et al. 2013). The Surat Basin has long been a target for petroleum and gas exploration and is now the centre of intense exploration and development for CSG resources (Cook and Draper 2013).
The large intra-cratonic Jurassic Surat Basin covers approximately 300,000 km^2 in eastern Australia (Exon 1976). The Surat Basin extends across south-east Queensland into New South Wales and unconformably overlies the Bowen and Gunnedah Basin (Green et al. 1997).

The Surat and Eromanga Basins developed in a back-arc setting inboard of the continental margin volcanic arc which, at times, provided considerable amounts of ash and volcanic material to the basins (Waschbusch et al. 2009). The Surat Basin formed from passive thermal subsidence following the Hunter-Bowen Orogeny in the underlying Bowen Basin (Fielding et al., 1996; McKellar, 1998).

The younger mid-Jurassic Surat Basin overlays the southern part of the Triassic to Permian Bowen Basin (Figure 10, Figure 15, Figure 17) (Green et al. 1997). The Surat Basin succession consists of up to 2500 metres (m) of sediments deposited in predominantly fluvio-lacustrine environments in the latest Triassic-Jurassic and coastal plain and shallow marine environments during the Cretaceous. The sedimentary sections of the Surat Basin are composed almost entirely of clastic rocks, with minor limestone and volcanics. The basin underwent continued thermal subsidence and was infilled by fluvial, lacustrine and mire (coal) sediments, with no recorded marine influence (Exon, 1976; Elliott, 1989; Hoffman et al. 2009).

Subsidence recommenced in the Early Jurassic, which led to the deposition of the sediment pile in the Surat Basin. In comparison to the underlying Bowen Basin, the Surat Basin rate of subsidence was much slower, with a much thinner package of sediment (usually < 2000 m) accumulated over a much longer ~100 Ma time period (ca 202 to 101 Ma) (Korsch and Totterdell 2009).

2.5 Structure – Surat Basin

The eastern boundary of the Surat Basin is the Auburn Province and the Texas Subprovince of the New England Orogen, between which lies the Kumbarilla Ridge (Cook and Draper 2013). To the west, it grades into the less coaly Birkhead Formation of the Eromanga Basin (Hamilton et al. 2014). Separating the Eromanga and Surat Basins is the broad basement high of the Nebine Ridge. The Mesozoic sediments of both basins onlap onto the Nebine Ridge, indicating that it was a positive feature since early in the basin history (Harrington 1989).

Yago (1996) emphasised the Great Artesian Basin as an intracratonic basin, and not a foreland basin (Figure 12). Palaeocurrent data indicated the dominant sediment dispersal direction was westerly (from the east) during the accumulation of the WSG. It was suggested that the principal controls on stratigraphic architecture were the passive style of subsidence and the variable rates of coarse sediment supply.

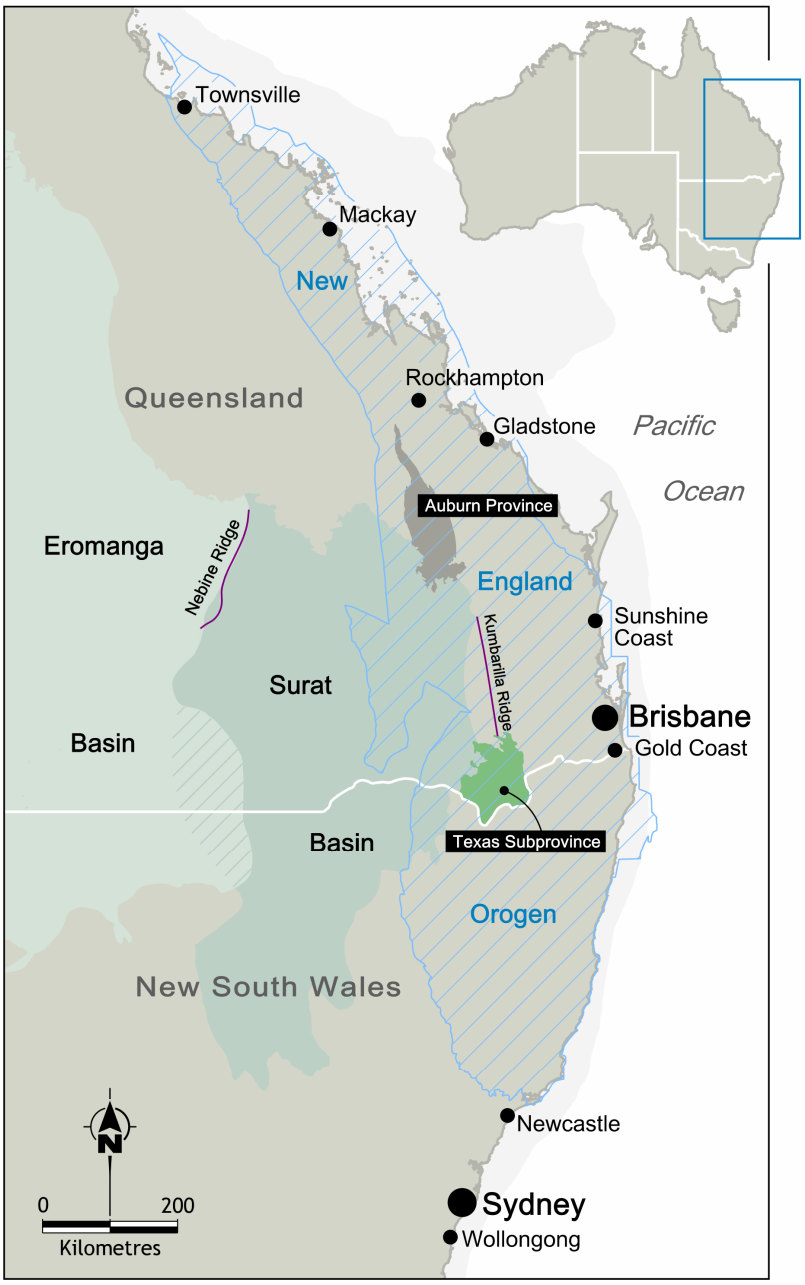

Figure 11: The eastern boundary of the Surat Basin is the Auburn Province and the Texas Subprovince of the New England Orogen.

Boult et al (1998) propose the deposition of sediments into the adjacent Eromanga Basin was dependent upon the sediment supply being controlled by a shifting balance between uplift on the eastern and south-western boundaries of the Australian plate (Figure 13). When uplift on the rifting margin to the southwest was greatest, cleaner reservoir quality sediments were deposited. However, when uplift and volcanic activity on the subducting margin to the east were greatest, a combination of the raising drainage base levels and the spread of highly labile volcanic arc derived material across the basin provided both the source rocks and seals (Boult et al. 1998).

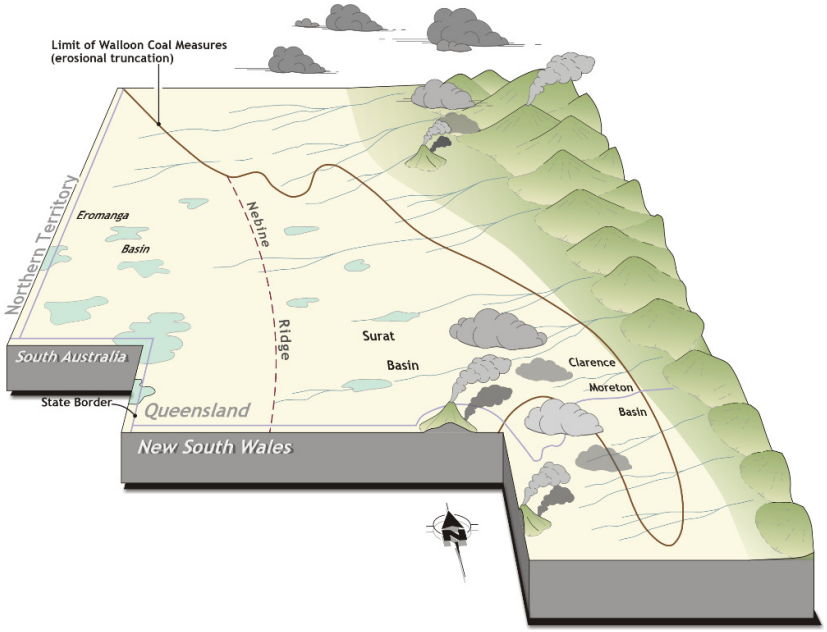

Figure 12: The Surat Basin is constrained by the Clarence Moreton to the east and the Eromanga Basin to the west. The Nebine Ridge sits between the Eromanga Basin and the Surat Basin. Adapted from Yago (1996).

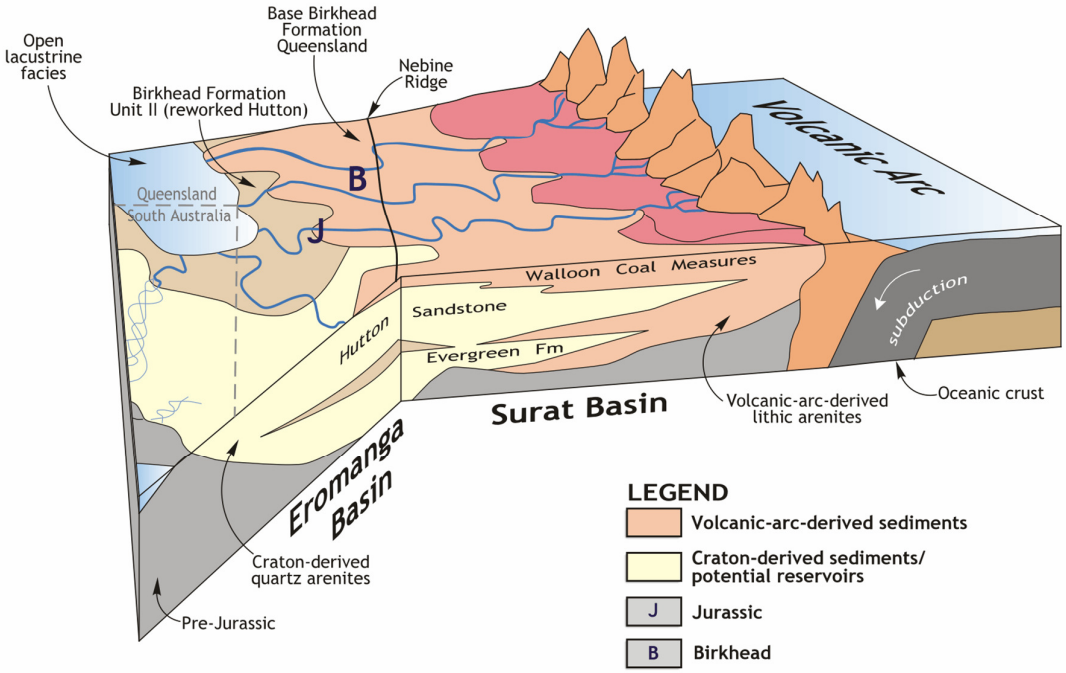

Figure 13: The volcanic arc derived sediments of the Walloon Subgroup and the deposition model of the Surat Basin. Adapted from Boult et al (1998).

2.6 Tectonic Evolution of Early Jurassic Basins

Almost all of eastern Australia was in a back-arc setting from the Early Jurassic to Early Cretaceous with only minor remnants of the magmatic arc being preserved near the coast in Queensland (Waschbusch et al. 2009).

The Great Australian Basin was initiated after a long period of erosion and peneplanation during the Late Jurassic which led to a large intracratonic sag. The intracratonic sag occurred within the continental interior, away from the plate margin which had undergone differential subsidence relative to the surrounding areas. There are a number of shallow platform basins that make up the Great Australian Basin including the Surat, Carpentaria, Clarence-Moreton and Eromanga Basins (Green et al. 1997).

There are a number of hypotheses on the formation of these basins:

1. Thermal sag after the cessation of rifting from the Camboon Volcanic Arc has been suggested as one theory of the basins' formation (Jell 2013)
2. Sag due to tension from divergent plate motion. A second theory which has been offered depicts similar extensive intracratonic sags developing under a tensional regime which has resulted from divergent plate motion (Green et al. 1997).
3. Pericratonic – basin formed near or accreted to the margins of the craton
4. Epicratonic – active on the surface of the craton (i.e. passive thermal subsidence).

The Walloon Subgroup may have recorded a failed (incipient) rift event along the present East Coast of Australia. A north-south elongated depocentre in the east, which covers much of the Clarence-Moreton Basin, coincides approximately with a zone that encompasses the greatest concentration of volcanic ash deposits, as well as eruptive and intrusive rocks. The bimodal mafic / felsic composition of the igneous rocks also indicate that this north-south belt may represent the site of a failed incipient rift (Yago and Fielding 1996).

Rifting around the southern and western margins of the Australian continent began during the late Middle-Late Jurassic as Gondwana began to break up. This rifting event did not commence until the Late Cretaceous along the eastern margins. As such, divergent plate motion is unlikely to be the driving force behind the inception of these Mesozoic basins (Green et al. 1997).

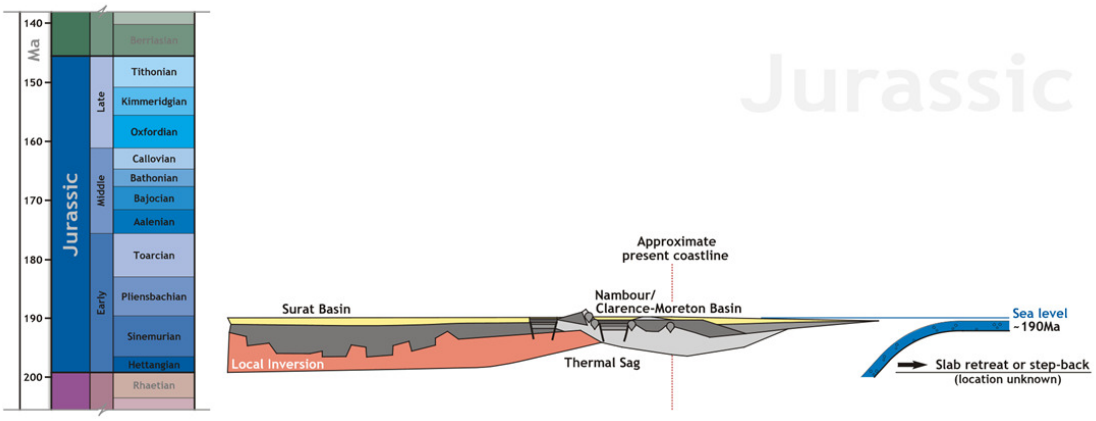

Figure 14: showing the tectonic evolution during the Early Jurassic. As the slab retreats, intracratonic sags are potentially developed under a tensional regime (Green et al. 1997). Adapted from Holcombe (2013).

A third theory concluded from Exon and Senior (1976) and Veevers et al. (1982) is the Mesozoic basins were pericratonic basins situated well to the east of the earlier Camboon Volcanic Arc active during Bowen Basin time and behind a final volcanic arc system. This was evidenced by the presence of tuffs and volcanogenic sediments (Exon and Senior, 1976; Veevers et al. 1982).

From their work on subsidence histories, Gallagher et al. (1994), explain that the subsidence of the Mesozoic basins was controlled by sublithospheric convection related to subduction along the eastern margin. This work supports the view that the basins were pericratonic (Green et al. 1997).

A fourth hypothesis proposes that the Surat Basin represents a period of dominantly passive, thermal subsidence within an epicratonic crustal setting (Exon, 1976; Gallagher, 1990; De Caritat and Braun, 1992). The basin began to subside during the Early Jurassic period, following the termination of the Hunter-Bowen Orogeny and a period of widespread erosion (Fielding et al. 1996).

For the Surat and Eromanga basin systems, the Jurassic to earliest Cretaceous was a period of entirely non-marine deposition. The lower package, which consists of the Hutton Sandstone to Walloon Subgroup (Figure 19), was determined by Hoffman et al. (2009) as Supersequence K (Figure 16), which is presented in more detail in the following section (Waschbusch et al. 2009).

Irrespective of the tectonic model used for the basin formation, all the hypotheses require it to be a terrestrial basin. For the Surat and Eromanga basin systems, the Jurassic to earliest Cretaceous was a period of entirely non-marine deposition.

2.7 Walloon Subgroup

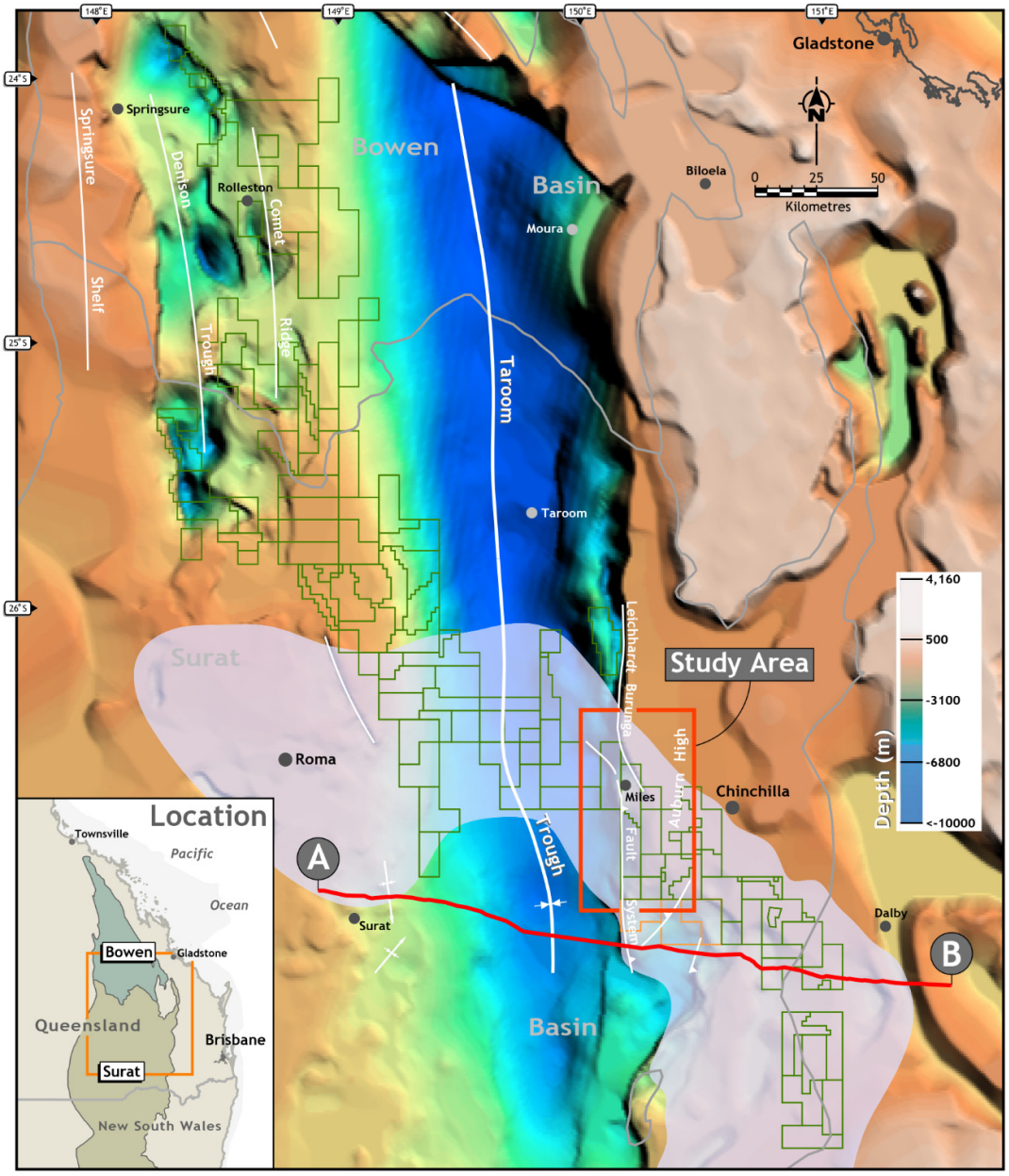

Figure 15: The study area within the Surat Basin (inset) showing the 'Walloon Fairway' (SEEBASE™ 2005), as shown in Figure 7 with the addition of the seismic line (A-B) as shown in Figure 16.

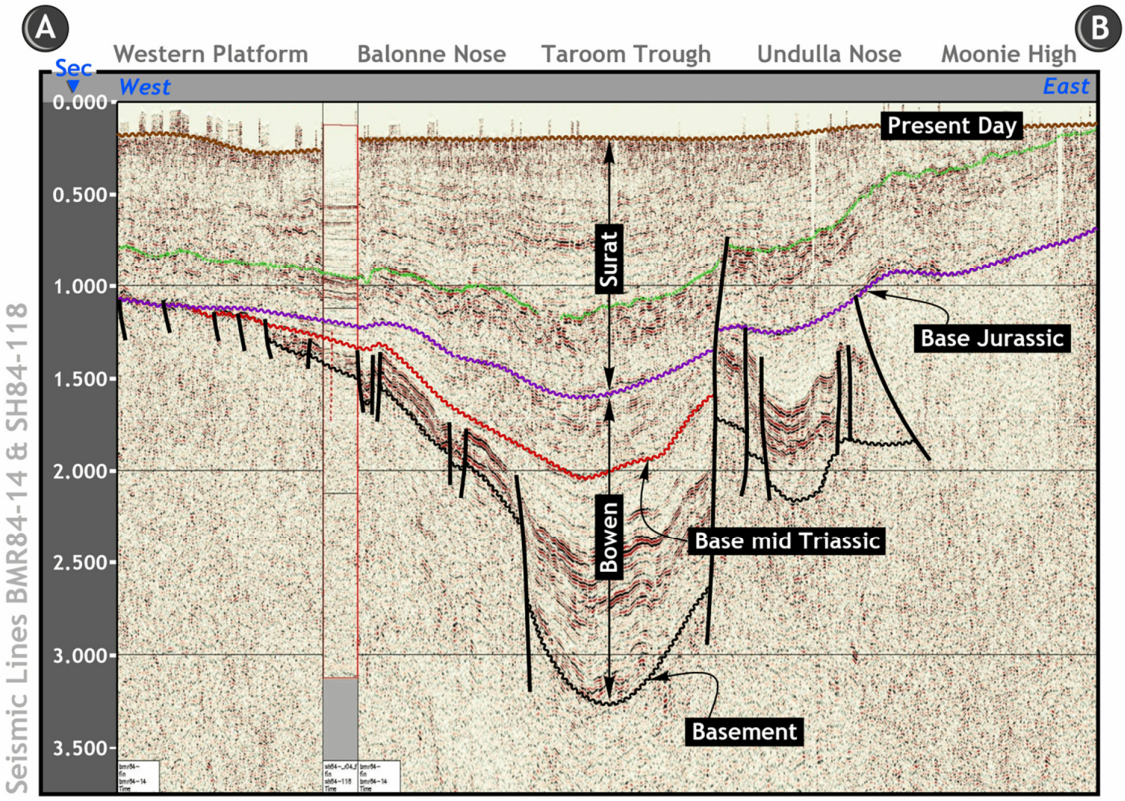

Figure 16: Seismic lines BMR84-14 and SH84-118 with interpretation showing the Bowen Basin overlain by the Surat Basin. The section location is displayed above (Figure 15).

Basement structures (Figure 16) appear to have significant influence on regional *in situ* stresses in the Permian to Triassic Bowen Basin and the Mesozoic Surat Basin and in turn, influence coal permeability (Brooke-Barnett et al. 2012). This work shows a correlation between variations of the horizontal stress orientation and magnitude with proximity to significant basement structures (Brooke-Barnett et al. 2012).

2.7.1 Depositional Environment – Walloon Subgroup

The Walloon Subgroup (WSG) (Figure 18) has a complex sediment distribution which is mainly influenced by the constant switching of alluvial channels influenced by differential, compaction-induced subsidence of peat and clastic sediments (Yago 1996). With the absence of outcrop, the coal and clastic features exhibit a high degree of complexity which makes interpretation difficult, even in closely spaced wells (Leblang et al. 1981).

The WSG are deposits of a vast alluvial plain that accumulated in a slow, passively subsiding intracratonic basin (Yago 1996). The sequence is interpreted as the deposits of an extensive alluvial plain, which was crossed by meandering channels of variable dimensions (Fielding 1993).

As deposited from an extensive alluvial plain (Figure 18), the WSG is interpreted as rivers that were separated by floodplains and discontinuous peat-forming wetland environments. These environments were affected by overbank sand deposition and reworking by channel migration (Yago 1996). The channel geometry of the Walloon Coal Measures can be classified as broad and shallow with complex fill geometry to sheet-like, and essentially unchannelised. The Tangalooma Sandstone of the WSG is interpreted as a major alluvial channel sandstone that exhibits sheet-like geometry with a width to thickness ratio exceeding 100 (Yago 1996).

Volcanic ash from numerous contemporaneous volcanic events has been preserved within the WSG. The ash was preferentially preserved in peat-swamp environments and, to a lesser amount, on proximal floodplain environments. These volcanic deposits are preserved as layers of bentonite and clay pellets isolated within the coals. The petrography of the sands shows the influence of volcanics. The sands are volcanic lithic and have a large portion of smectite in the matrix fraction of the sandstones. A possible source for these volcanic eruptions could be in North Eastern New South Wales during the Mesozoic which is regarded as an area of widespread volcanism (Yago 1996).

Hoffman et al (2009) refer to the WSG, Eurombah Fm and Hutton Sandstone as part of Supersequence K (Figure 17). The Hutton Sandstone and Eurombah Formation are from meandering fluvial deposition environments whilst the WSG is from fluvial, swampy and lacustrine depositional environments.

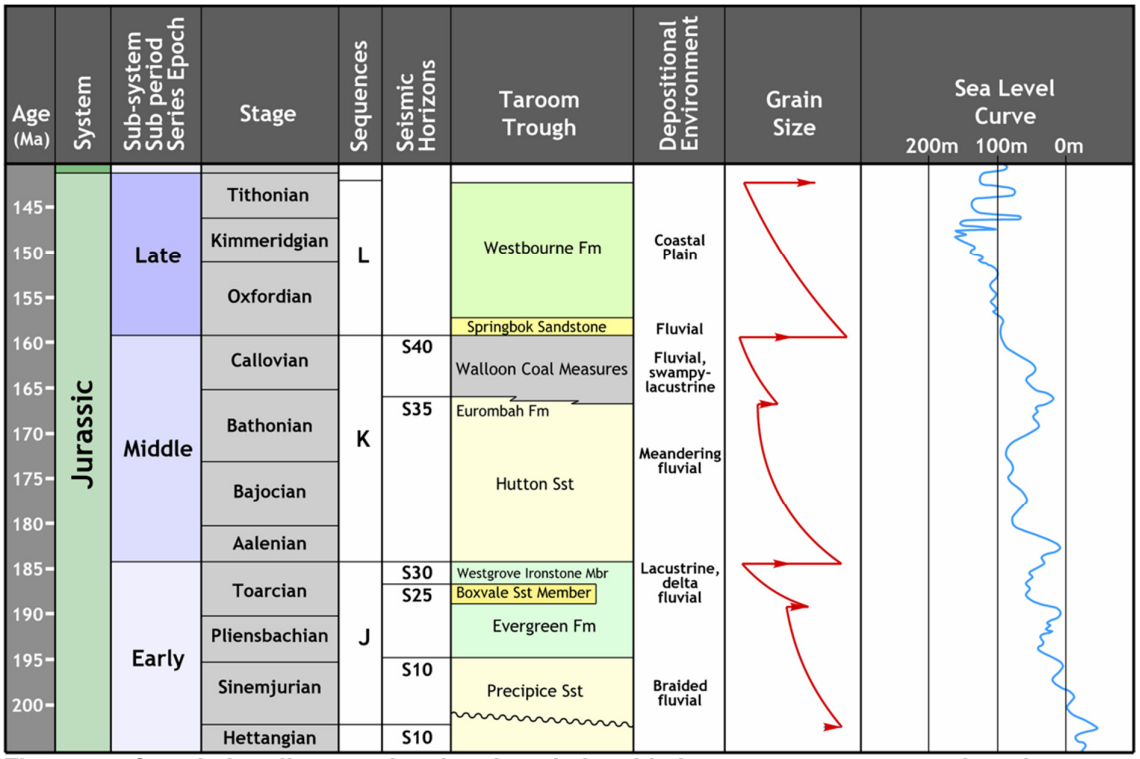

Figure 17: Correlation diagram showing the relationship between sequence stratigraphy, lithostratigraphy and sea-level for the Jurassic section within Supersequences J, K and L. Supersequence K consists of the Hutton Sandstone to the Walloon Coal Measures

Supersequence K (Figure 17) consists of a fining-upward succession of three lithofacies which approximately equate with the Hutton sandstone (Lithofacies K1), Eurombah Formation (Lithofacies K2) and the Walloon Coal Measures (Lithofacies K3) (Hoffman et al. 2009).

Lithofacies K2 (Figure 17) is the equivalent to the Eurombah Formation and consists of lithic conglomeratic sandstone with some conglomerate, siltstone and mudstone beds that were deposited by meandering streams. The unit is up to 100 m thick and is conformable with both the Hutton Sandstone below and the WSG above (Exon 1976). The Eurombah Formation is not laterally extensive and interfingers with the base of the WSG (Hoffman et al. 2009). The Eurombah Formation is deposited in sluggish meandering streams (Exon 1976).

Lithofacies K3 (Figure 17) is equivalent to the WSG and consists of sandstone, siltstone, mudstone and rare to abundant coal seams. The deposits are extensive, with a maximum thickness of 650 m. The contact with the underlying strata is transitional. Palynological data indicates that the base of the WSG becomes younger to the west (Hoffman et al. 2009).

Compositionally the sandstone is lithic consisting of abundant montmorillonite and volcanic debris, which suggests the volcanic activity was contemporaneous. Sandstones inter-bedded with rare coals in the lower part of the formation imply stream deposition. The abundance of coal indicates that the rest of the unit was laid down in poorly drained floodplains (Exon 1976).

Sedimentation in the Surat Basin ceased in the middle Cretaceous. The cessation coincided with a compressional event that was responsible for the uplift and erosion of the Bowen and Surat Basins and their associated volcanic arcs. Phases of deformation also occurred during the Late Cretaceous and Tertiary due to epeirogenic movements, as well as forces relating to divergent plate motion during the break up of Gondwana (Exon, 1976; Veevers et al. 1982; Fielding et al. 1990; Elliot, 1993; Green et al. 1997).

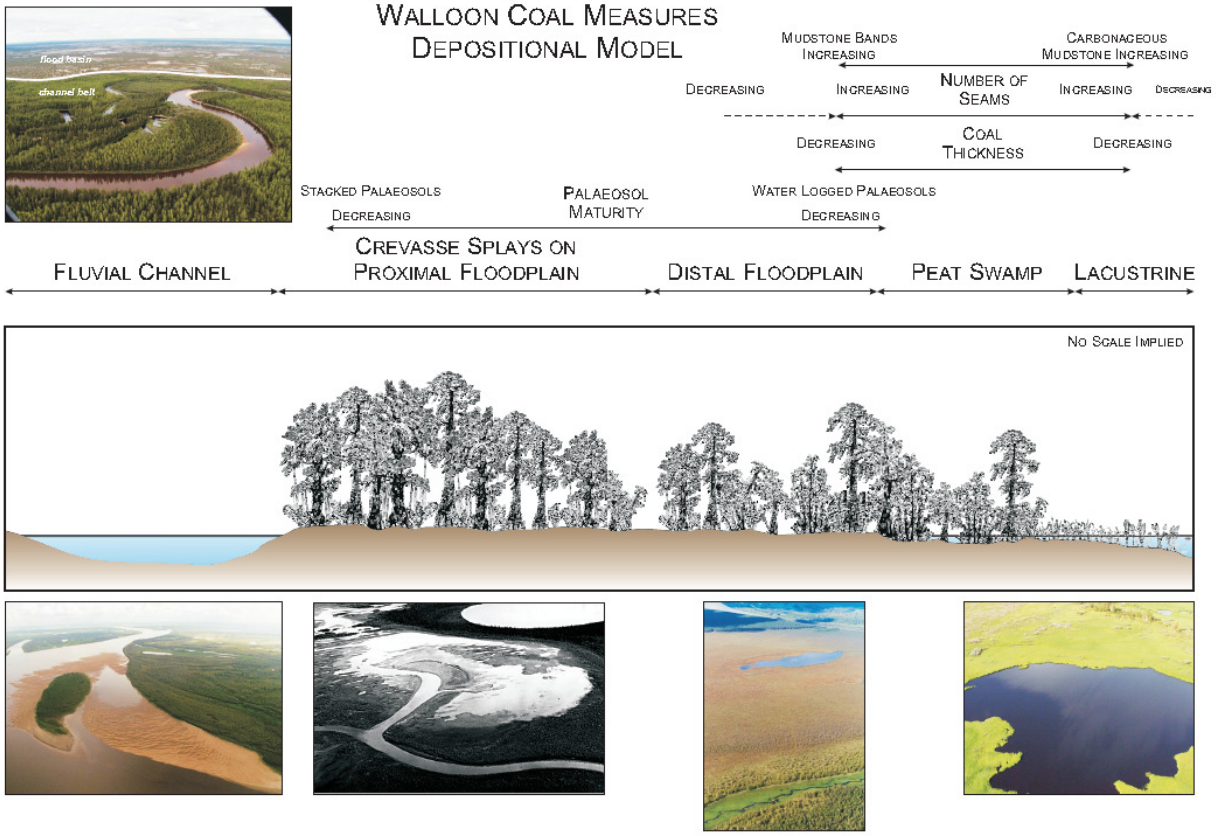

Figure 18: A deposition model of the Walloon Subgroup (Pidgeon 2012) showing the five main facies types and respective deposition environments. This deposition model highlights the changing energy environments for deposition and dfifficulties for correlation.

2.7.2 Sequence Stratigraphy – Walloon Subgroup

The original work by Jones and Patrick (1981) presented the WSG as regionally extensive, which was then later interpreted to be a local occurrence by Green et al (1997), and then later reinstated by Scott et al (2004) as being regionally extensive (Figure 19). Hoffman et al (2009) have applied the principles of non-marine sequence stratigraphy (Figure 21) to the Jurassic strata in the lower part of the Surat Basin. The recognition of sequence boundaries is more problematic in interior basins where the depositional system may be entirely fluvial. This detailed work has been done to understand the Jurassic strata in the lower part of the Surat Basin (Hoffman et al. 2009).

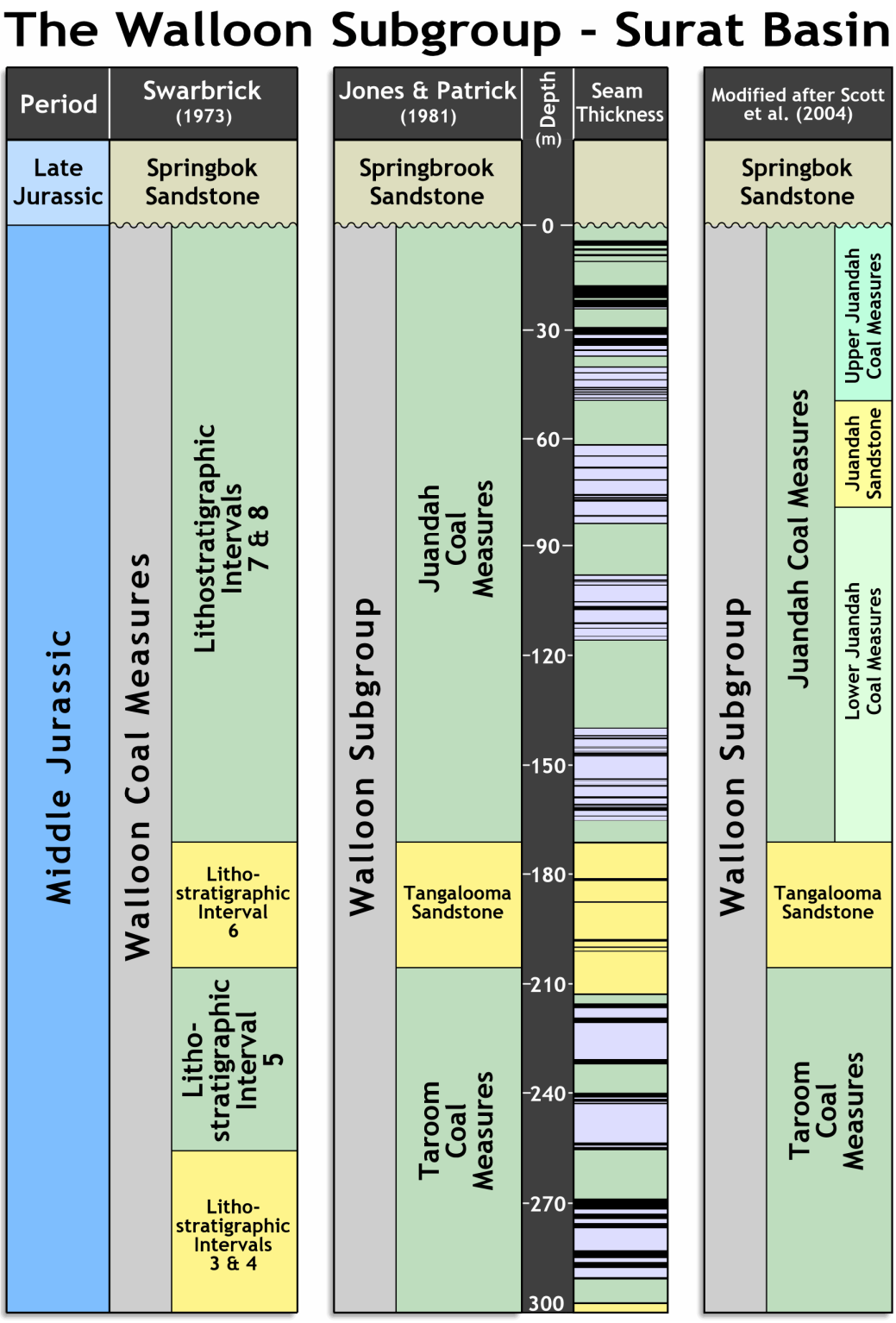

Figure 19: From left to right, the stratigraphy of the Mid-Jurassic Walloon Subgroup, as detailed in Swarbrick (1973), Jones and Patrick (1981) and the contemporary stratigraphy utilised by Origin Energy that includes the Juandah Sandstone. The Walloons Subgroup has a reported maximum thickness of 650 m (Hoffman et al. 2009). Adapted from Scott et al (2004).

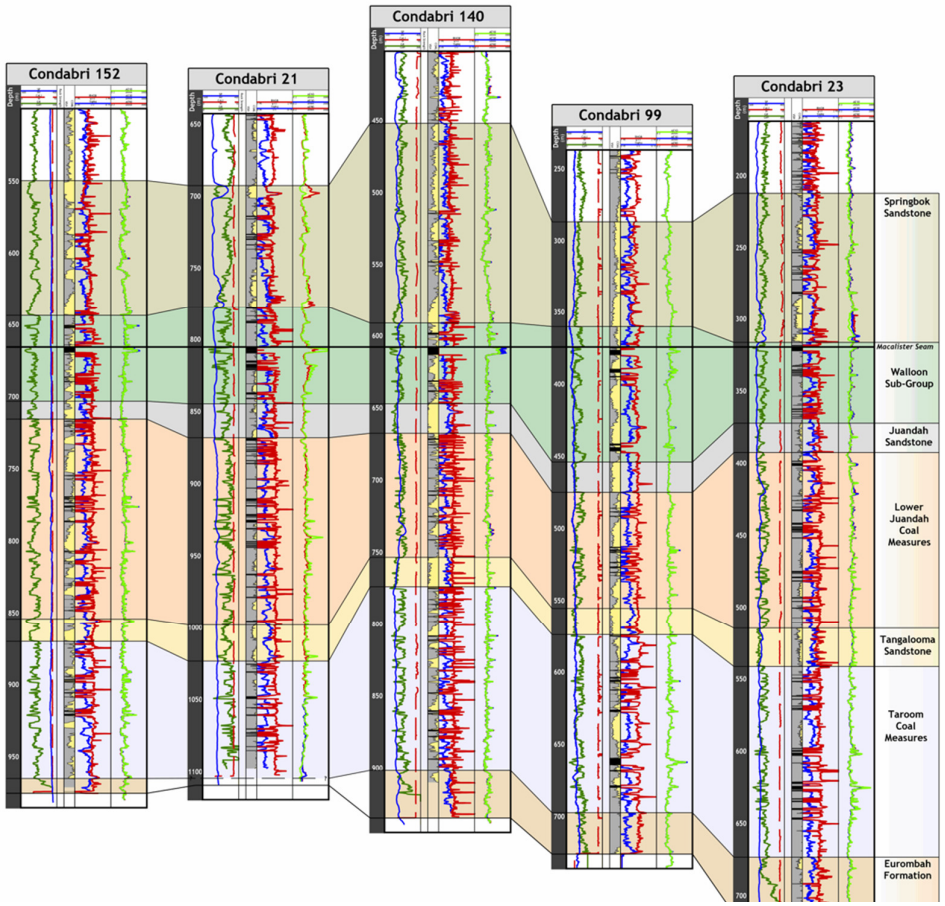

Figure 20: A correlation of five wells prepared from Origin well data for the area of this study to give an indication of the heterogeneity of the WSG.

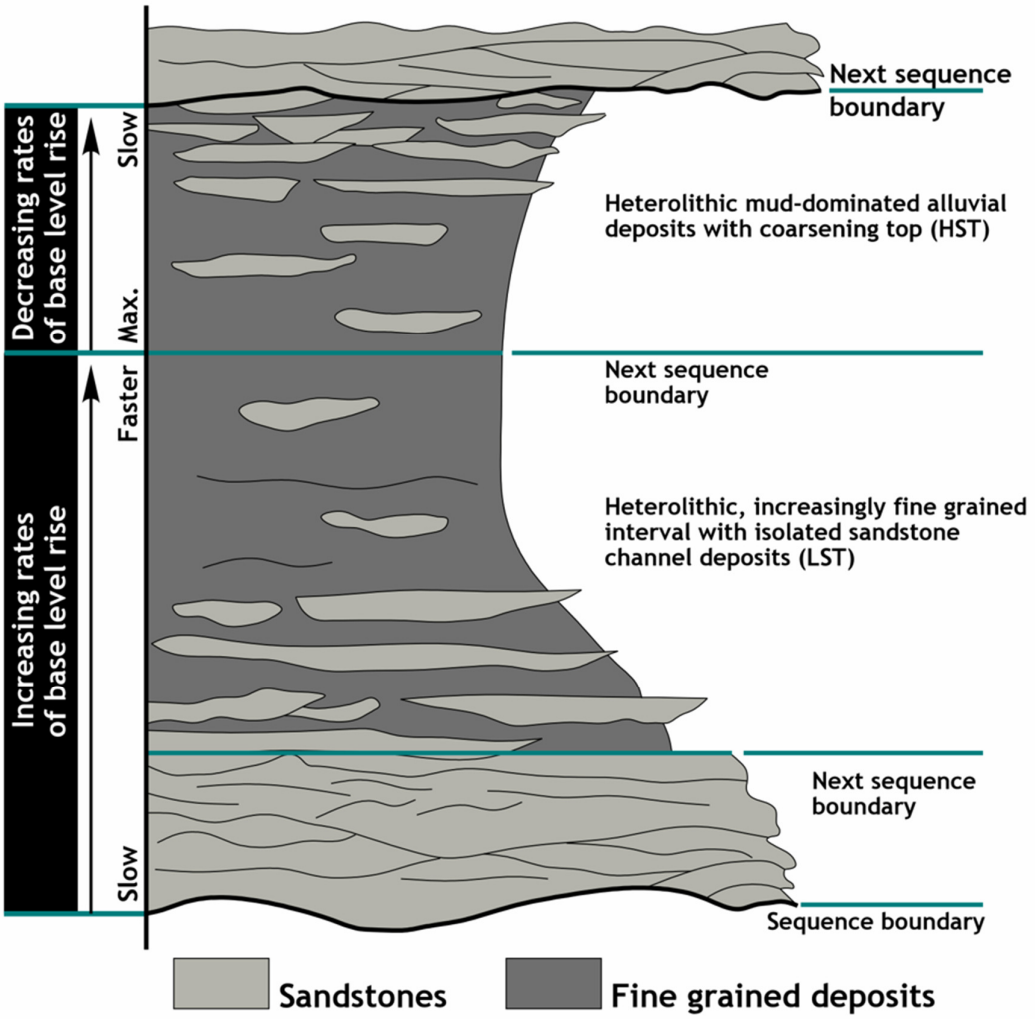

Figure 21: The idealised non-marine sequence commences with the regionally extensive erosion surface caused by a fall in base-level is referred to as the Lowstand System Tract (LST) (Hoffman et al., 2009). Adapted from Olsen et al (1995).

Recognition of sequence boundaries within interior basins, where the depositional system may be entirely fluvial, can be problematic (Shanley and McCabe 1994). The Surat Basin is an interior basin located considerable distance from the sea, and the depositional system is entirely fluvial (Hoffman et al. 2009). As the accommodation space is driven by tectonic and / or climatic cycles, the role of relative sea level change in influencing depositional systems is of little importance (Shanley and McCabe 1994), thereby diminishing the applicability of sequence stratigraphic approaches.

In coastal environments, a sequence boundary can be recognised by an abrupt basinward shift in facies, such as fluvial deposits overlying marine shales or nearshore facies. The recognition of these sequence boundaries in interior basins depends almost entirely on changes in alluvial stacking patterns (Shanley and McCabe 1994) (Figure 21).

In general, the accommodation cycles for the Jurassic Surat basin supersequences do not show any direct correlation with the eustatic sea-level curve (Hoffman et al. 2009). It is estimated that the Jurassic coast was more than 300 km from the eastern edge of the Surat Basin (Bradshaw and Yeung 1992). This would make it unlikely that sea-level fluctuations could have directly influenced deposition (Hoffman et al. 2009).

Due to the easterly initiation of the sag of Eastern Australia during the Early Jurassic, the sediments of the Surat Basin were deposited with onlap to the west (Elliott 1993). Exon (1976) suggests a general westerly source during the Jurassic with streams flowing east or southeast.

Sedimentation within the Surat Basin was controlled primarily by a steady subsidence rate with sediment input from cratonic or volcanic sources (Fielding et al. 1996). Yago (1996) shows that the sediment dispersal pattern was dominantly westward. Yago (1996) also proposed that the sandstone was a complex unit due to constant avulsion. This can also be demonstrated by the low coal abundance to the west, where the sediment flow was directed (Yago 1996). The WSG is laterally continuous with the Birkhead Formation of the Eromanga Basin, but the Birkhead has little or no coal (Green et al. 1997).

2.7.3 Volcanic influence to sedimentation

There is variation of the composition of the clastic sediments in the basin (Waschbusch et al., 2009). The sediments fluctuate from quartz-dominated to volcanogenic dominant. There is a progressive increase in the proportion of volcanogenic material eastward from the Eurombah Basin across the Surat Basin and into the Maryborough Basin, which now sits on the present day Queensland coast. Thus, the inferred contemporaneous volcanic arc is located off what is now the present-day east coast of Queensland (Waschbusch et al. 2009).

There is evidence of montmorillonite (bentonites) in the Walloon Subgroup and overlying Springbok Sandstone (Exon 1976; Veevers 1984; Hawlader 1990; He et al. 1994; Hoffman et al. 2009). This is considered to be an indication of the continued volcanism associated with a subducting plate margin to the east during the Mid-Late Jurassic (Hoffman et al. 2009).

In contrast to Hoffman et al. (2009), Fielding (1996) and Yago (1996) present the distribution of volcanic ash beds in the Walloon Coal Measures as an intra-basinal Jurassic volcanic source. Both Fielding (1996) and Yago (1996) indicate that the accumulations of the Walloon Subgroup coincided with the emplacement of voluminous and extensive mafic intrusions in New South Wales, Tasmania and West Antarctica. These events have been interpreted to record the early stages of rifting of the south-eastern Australian continental margin (Hoffman et al. 2009).

Specific studies on the Tangalooma Sandstone of the Walloon Subgroup have been completed by Rohead-O'Brien (2011) to understand the reservoir potential. From this work, the Tangalooma Sandstone reportedly contains significant clay content. Understanding the extent of these clays, and how they will influence fines production, are critical for future production of CSG reserves within the Surat Basin.

Martin et al. (2013) have focussed on the sedimentology and stratigraphy of the WSG to recognise the relationships of the coals and associated facies to identify fluctuations in accommodation space. Understanding these relationships may give an understanding of the scale of the coal bodies and their potential to correlate. This work also presents the petrology of a number of samples to show the composition was proved to be immature lith-arenites (Martin et al. 2013). This composition will have some influence on the geomechanical properties of these formations.

2.8 Summary

In essence the Surat Basin is an intra-continental basin, its internal structure was influenced by a long-lasting tectonic history of convergence and extension. This led to the deposition of 'stacked' basins - dominantly in continental depositional environments. The rock content of the Surat Basin, and the Walloons Sub Group in particular are clearly dominated by fluvio-lacustrine depositional environment with a significant volcanic over-print. The WSG contains 20-40m of coal in 300-400 m of interburden, resulting in an average net/gross ratio of 0.08. Coals are the obvious target for gas extraction in the WSG. Given the Surat Basin is a typical intracontinental Basin, sequence stratigraphic models (typically based on eustatic sea-level changes) appear of limited applicability here.

Both, depositional facies and volcaniclastic overprint are key considerations in the following analyses and interpretations of the WSG. The volcaniclastically influenced interburden, appears to be the main contributor of fines in gas wells in the WSG. Consequently, interburden successions, are the focus of the present study.

To demonstrate the impact of volcaniclastic clays on fines production the following chapter examines simple rock -fluid interaction experiments. The outcomes will guide and frame other analyses presented in this thesis.

Chapter 3 - Rock Dissolution and Stabilisation Analysis

3.1 Introduction

The WSG is a terrestrial deposition environment with volcanic influence and has a low net to gross ratio (25 – 35 m of net coal over a 350 m section) with vertical and lateral heterogeneity. CSG production requires water extraction to lower pore pressure for gas desorption from the coal. The interburden are exposed to interaction with fluids during production. The formation water of the WSG is considered the same composition within the coals and the interburden. During the production life, formation water is exposed to clastics in the wellbore (Figure 1, Figure 2).

Chemical effects may be observed in minerals of a rock framework reacting with the pore fluid. In particular, chalk and clay minerals become soft, or even dissolve, if the water is not in chemical equilibrium with the mineral. This implies that fluid substitution may actually change the framework moduli due to chemical effects (Fjaer et al. 2008).

3.2 Objectives

The produced solids in the majority of wells are from the interburden, not coal (Figure 1). From this observation, the testing and characterisation is focused on the interburden. A comprehensive program of mineralogy and rock fluid sensitivity testing was conducted on selected sandstone, siltstone and mudstone core material from Condabri 23, Zig Zag 6 and Combabula 23. Samples from Zig Zag 6 and Combabula 23 were selected to better understand the lateral extent of the interburden.

The rock dissolution and stabilisation analyses were designed to simulate wellbore conditions during production. Most WSG CSG wells are completed with a pre-perforated liner, which allows interaction between the produced fluids and the exposed clastics. This continues during dewatering whilst the fluid level is pumped off. When the interaction of interburden and water is occurring, downhole pumps can wear and require workover and re-completion, which often results in direct observation of the amount of fines production (Figure 22).

The aim of this chapter is to:

a. establish the root cause of interburden disaggregation (fines production);
b. potentially identify a particular lithology or formation that may be more susceptible to solids production, and;
c. show results of trials that have attempted to stabilise disaggregation.

Figure 22: The slotted intake from a Condabri production well which was worked over for produced solids.

Interburden rocks were exposed to four fluids to test both disintegration and stabilization.

1. Synthetic brine (produced formation fluid).
2. Potassium chlorides (KCl) and clay stabilisers (commercially available clay stabilisation products).
3. Clay stabilisers (24 hours and 5 days).
4. Calcium chloride ($CaCl_2$) at various time intervals up to 33 days.

The purpose of the testing was to:

1. define which depth intervals and corresponding lithologies are susceptible to water weakening following brine re-saturation;
2. establish the mineralogy of the various lithologies that are stable or susceptible to weakening following saturation with synthetic brine, and;
3. provide parameters to aid in understanding down-hole wellbore stability and sanding issues.

The tests were designed to simulate static downhole conditions. Test 1 (synthetic brine) was designed to test the effects of produced water on the interburden. Test 2 (clay stabilisers) was to test the effectiveness of the commercially available clay stabilisation products. Test 3 was to test the same stabilisers from Test 2 over 24 hours and 5 days. Test 4 was designed to test $CaCl_2$ at various time intervals up to 33 days.

The fluids were selected from a range of commercially available clay stabilisation products, as well as for their compatibility with current drilling fluids. The products had to have been utilized in previous drilling, completions and subsequent workover operations.

The samples were prepared by conducting a wireline to core depth shift using a high resolution image log and correlating to the first logging run (Platform Express). For the depth intervals where multiple tests were conducted, sister samples were used from the same interval. This method used a 3.5” diameter core cut into quarters. All depths indicated within this chapter are measured depths taken directly from the received material as core depth.

When relating core information to log response, the scale of measurement being used must be considered. Core samples are directly representative of the formation and the analysis directly measures discrete physical properties of the core. The spatial resolution of the core must be considered relative to that of the formation as well as the vertical resolution and depth of investigation of the logging response used in the analysis (Morton-Thompson and Woods 1993).

For example, the depth of investigation of the formation density tool is approximately six inches when collected in a wellbore with a diameter of eight and a three-quarter inches (Figure 23). The volume of rock actually seen by the tool is restricted to one quadrant, with a penetration depth of six inches and a height of eight inches. This equates to more than 300 in^3 of material measured. When this compares to a one inch wide by two inch long core plug, the log measures almost 200 times the volume represented by the core plug (Morton-Thompson and Woods 1993).

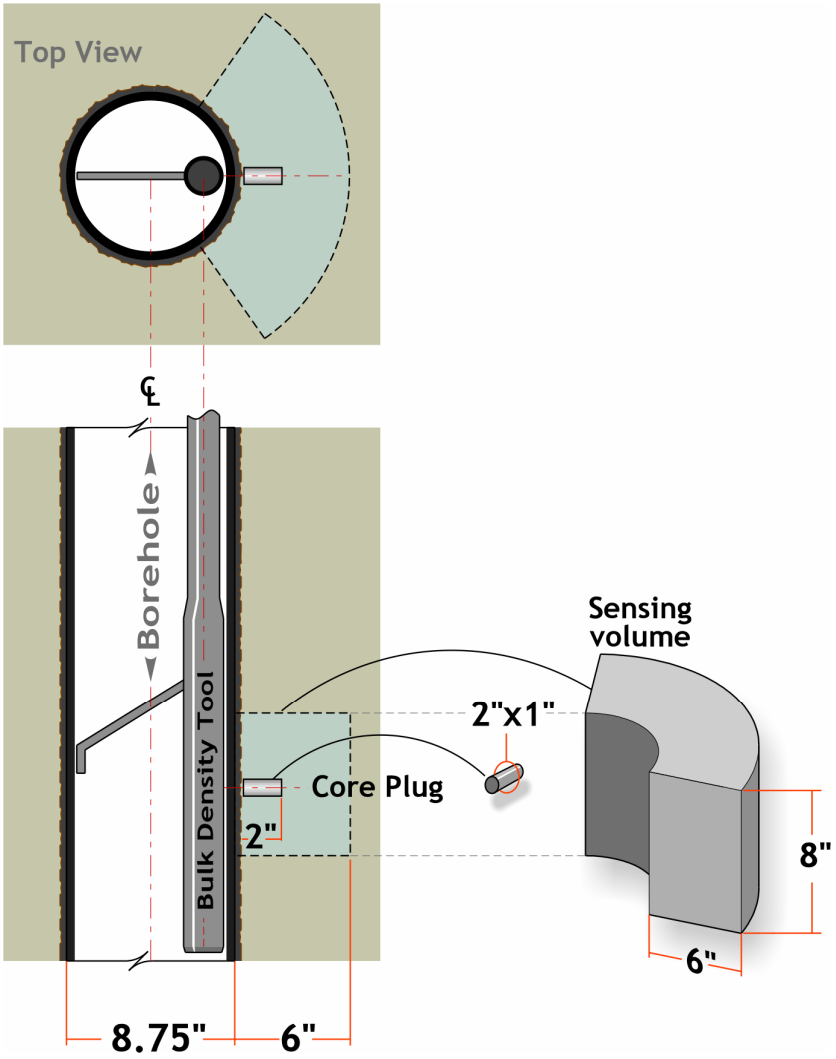

Figure 23: The comparison of the volume of the formation measured by the bulk density tool relative to the volume obtained from a core plug. The log measures almost 200 times the volume measured by the core plug (Morton-Thompson and Woods 1993).

3.3 Saturation Effects on Rock Integrity

3.3.1 Saturation Effects Using Synthetic Brine (produced fluid)

Fluid-rock interaction was investigated using competent rock samples taken using a two-inch sample of a quarter of the whole core sections and photographed prior to testing (Figure 24). The original (pre-saturation) core sample was tested as received in their effective room dry condition. A vacuum saturation was then performed by immersion of the sample in the synthetic formation fluid and holding under moderate vacuum for approximately one hour, with the sample then allowed to soak for a minimum five days. The samples were then saturated in 200 ml of an ionic

composition similar to the produced formation water from Condabri 16. The synthetic brine contained approximately 3600 mg / litre of total dissolved solids (Table 1).

Table 1: Synthetic brine ionic composition based on samples of produced water from Condabri 16.

Grams / litre	Compound
1.820	NaCl
0.014	KCl
2.150	$NaHCO_3$
0.022	$CaCl_2.2H_2O$
0.020	$MgCl_2.6H_2O$

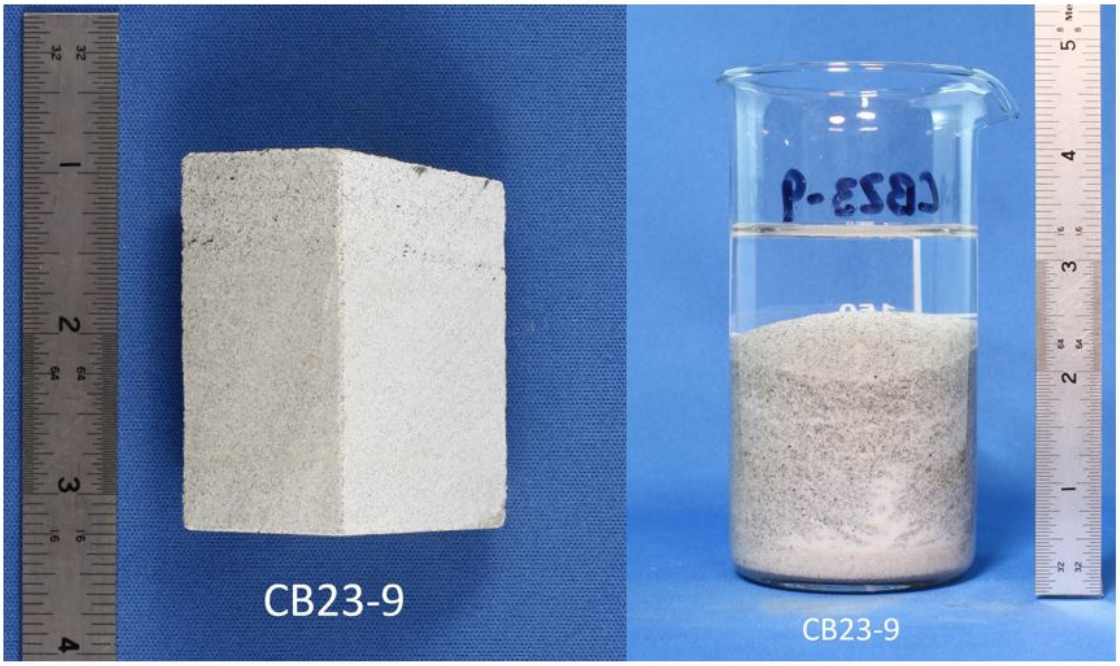

Figure 24: Pre (left) and post (right) samples from Condabri 23 (CB23-9). The post analysis sample (right) has disaggregated following the 5 day synthetic brine re-saturation.

Each sample was photographed initially dry (original state) then in contact with synthetic brine or various clay stabiliser solutions in order to qualitatively evaluate the change in both rock strength and stability over the duration of fluid exposure (Figure 24).

3.3.2 Results

From a total of 32 samples tested from Condabri 23, 22 were completely disaggregated, 7 were partially disaggregated and 3 were mostly intact (Figure 25). A total of 22 samples were tested on Combabula 23; of which 19 were completely disaggregated, 2 were partially disaggregated and 1 was mostly intact. Zig Zag 6 had a total of 11 samples tested; of which 8 were completely disaggregated, 2 were partially disaggregated and 1 was mostly intact. Hence, out of the 65 samples tested, over 93% of the samples experienced some degree of disaggregation, with over 75% of samples being completely disaggregated (Table 2). Disaggregation was not confined to any particular lithology in any well. Six sister samples from each well were also selected for XRD analysis, based on the degree of disaggregation, such that samples exhibiting total, partial disaggregation and intact samples were tested to define mineralogy.

Table 2: Results of dissolution analysis using synthetic brine. From the results presented, disaggregation was not confined to a particular lithology.

Well Name	Total Number of Samples	Disaggregation	Partial	Mostly Intact
Condabri 23	32	22	7	3
Combabula 23	22	19	3	1
Zig Zag 6	11	8	2	1

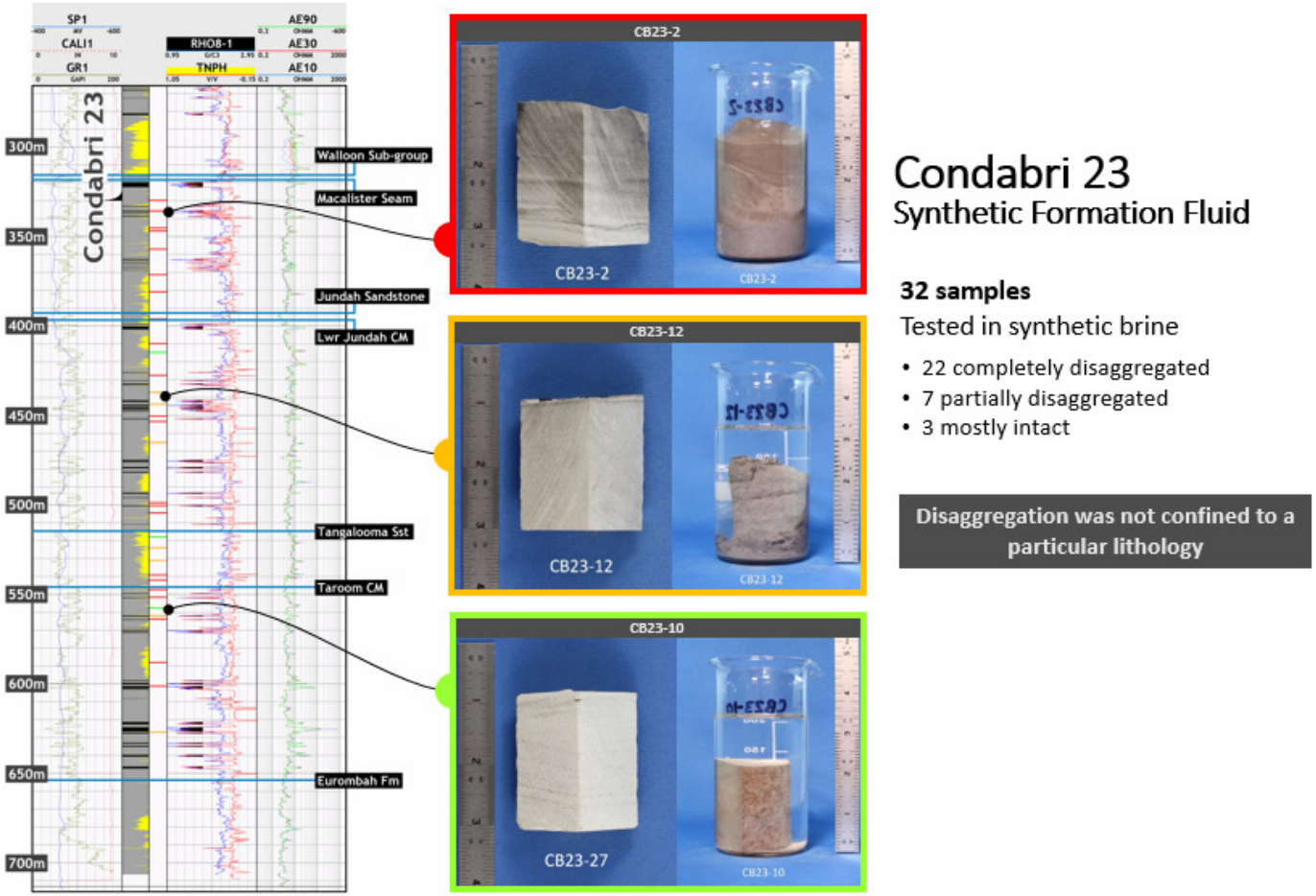

Figure 25: The distribution of the 32 core samples from Condabri 23 in the dissolution trials using the synthetic formation fluid. The sample in the red box indicates total disaggregation (22 samples), the orange box (middle) represents partially disaggregation (7 samples) and the green box (bottom) shows the sample as mostly intact (3 samples).

3.3.3 Saturation Effects Using 5% KCl and Clay Stabilisation Fluids

From the results of the dissolution analysis using the synthetic brine, one depth interval that displayed total disaggregation, was selected from each of the wells Condabri 23, Combabula 23 and Zig Zag 6. These intervals were selected to test a 5% KCl solution and four different commercially available clay stabilisation products. A synthetic brine was also used on one sample as a control. The methodology was similar to the previous produced fluid saturation analysis. Pre-test digital images were also recorded.

The vacuum saturation was performed on six sister samples under moderate vacuum for approximately one hour in synthetic formation water (control), 5% KCl and the four clay stabilisation solutions. All samples were allowed to soak for a minimum of five days. The control sample was saturated in 200 ml of brine with an ionic composition similar to that of the produced formation water (Table 1).

The synthetic brine, 5% KCl and the four clay stabiliser solutions are listed in Table 3 using manufacturer recommended dose rates with 200ml per sample. The pre and post saturation sample photographs showing the sample condition pre-saturation and post-saturation are presented in this chapter.

Table 3: The six samples showing the composition of the five clay stabilisation products and synthetic brine.

Stabiliser	Composition
Synthetic Brine	As shown in Table 1
KCl 5% (by weight)	5g KCl added to 100 ml deionised water
L042 2%	2 ml L042 added to 100ml deionised water
L064 0.2%	0.2 ml L064 added to 100ml deionised water
L071 0.2%	0.2 ml L071 added to 100 ml deionised water
NH_4Cl 1%	1 g NH_4Cl added to 100 ml deionised water

3.3.4 Results

The samples exposed to synthetic brine (control) and the L042, L064 and L071 clay stabiliser solutions exhibited significant disaggregation. The exception was the 5% potassium chloride (KCl). In this case the samples from Condabri 23, Combabula 23 and Zig Zag 6 remained mostly intact following the saturation period. The samples saturated with 1% ammonium chloride (NH4Cl) exhibited partial disaggregation (Figure 26).

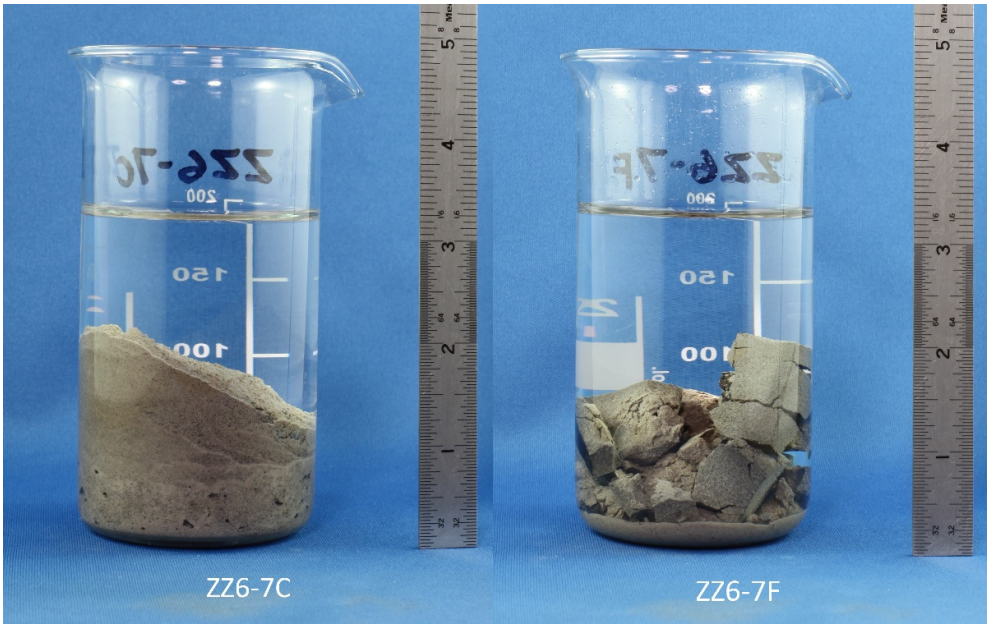

Figure 26: Zig Zag 6 samples showed total disaggregation using 2% L042 and a 5 day saturation period whilst the 1% NH4Cl had partial disaggregation over the same time.

3.3.5 Saturation Effects Using Various KCl Concentrations and L042 Clay Stabilisation Fluid

The depth interval that showed total disaggregation in synthetic brine was used from Condabri 23. The sister samples were one quarter whole core sections, approximately two inches in length. A total of seven samples were tested using two combinations of KCl with L042, as well as five different concentrations of KCl to define its concentration threshold.

The core condition was recorded using pre-test digital images. A moderate vacuum was applied for vacuum saturation for approximately one hour for the various clay stabilisation fluids (Table 4). The samples were then allowed to soak for a minimum of five days.

To simulate wellbore conditions for the two KCl + L042 samples, the stabilisation solution was replaced with synthetic brine to dilute the original concentration of stabilisation solution. These two samples were photographed after 24 hours and the remaining samples were photographed after five days. A pre and post saturation

sample photograph showing the sample condition pre-saturation and post-saturation are shown above (Figure 24).

Table 4: KCl and L042 clay stabiliser solution composition.

Stabiliser	Composition
KCl 5% + L042 2%	5g KCl and 2 ml L042 added to 100ml deionised water
KCl 1% + L042 2%	1g KCl and 2 ml L042 added to 100ml deionised water
KCl 2%	2g KCl added to 100ml deionised water
KCl 1%	1g KCl added to 100ml deionised water
KCl 0.5%	0.5g KCl added to 100ml deionised water
KCl 0.1%	0.1g KCl added to 100ml deionised water
KCl 0.01%	0.01g KCl added to 100ml deionised water

3.3.6 Results

After the initial 24 hours of soak time, the two samples saturated in KCL + L042 were partially disaggregated. Once the original concentration of L042 was diluted, the sample was totally disaggregated following five days submersion in synthetic brine. The samples saturated in 2% and 1% KCl solutions exhibited partial disaggregation whereas the lower concentrations (0.5%, 0.1% and 0.01%) totally disaggregated during the soak period.

3.3.7 Saturation Effects Using $CaCl_2$ Clay Stabilisation Fluids

The same depth interval from Condabri 23, which showed total disaggregation, was selected to test the $CaCl_2$ solutions as an alternative clay stabiliser. A control of synthetic brine (Table 1) was used, as well as three samples of $CaCl_2$ using various concentrations of 5%, 10% and 15% (Table 5). The pre-saturation core condition was recorded using a pre-test digital image of the intact samples. A moderate vacuum was applied for vacuum saturation and samples were allowed to soak for five days.

To simulate wellbore conditions of dilution by formation fluid, the $CaCl_2$ solutions were replaced with synthetic brine after an initial five days of soak time. A second brine replacement was performed after a further five days (progressively ten days) of soak time. The final photographs were performed after 33 days in the third brine solution replacement.

Table 5: Clay stabiliser solution composition.

Stabiliser	Composition
Synthetic Brine	As shown in Table 1
$CaCl_2$ 5%	5g $CaCl_2$ added to 100ml deionised water
$CaCl_2$ 10%	10g $CaCl_2$ added to 100ml deionised water
$CaCl_2$ 15%	15g $CaCl_2$ added to 100ml deionised water

3.3.8 Results

As observed in previous analysis, the synthetic brine saturated sample displayed total disaggregation. The remaining samples saturated in various concentrations of $CaCl_2$ solution (progressively replaced with three batches of synthetic brine) displayed only partial disaggregation following 33 days in the third batch of synthetic brine. From the partial disaggregation displayed, there was some separation that occurred between existing fractures and bedding planes.

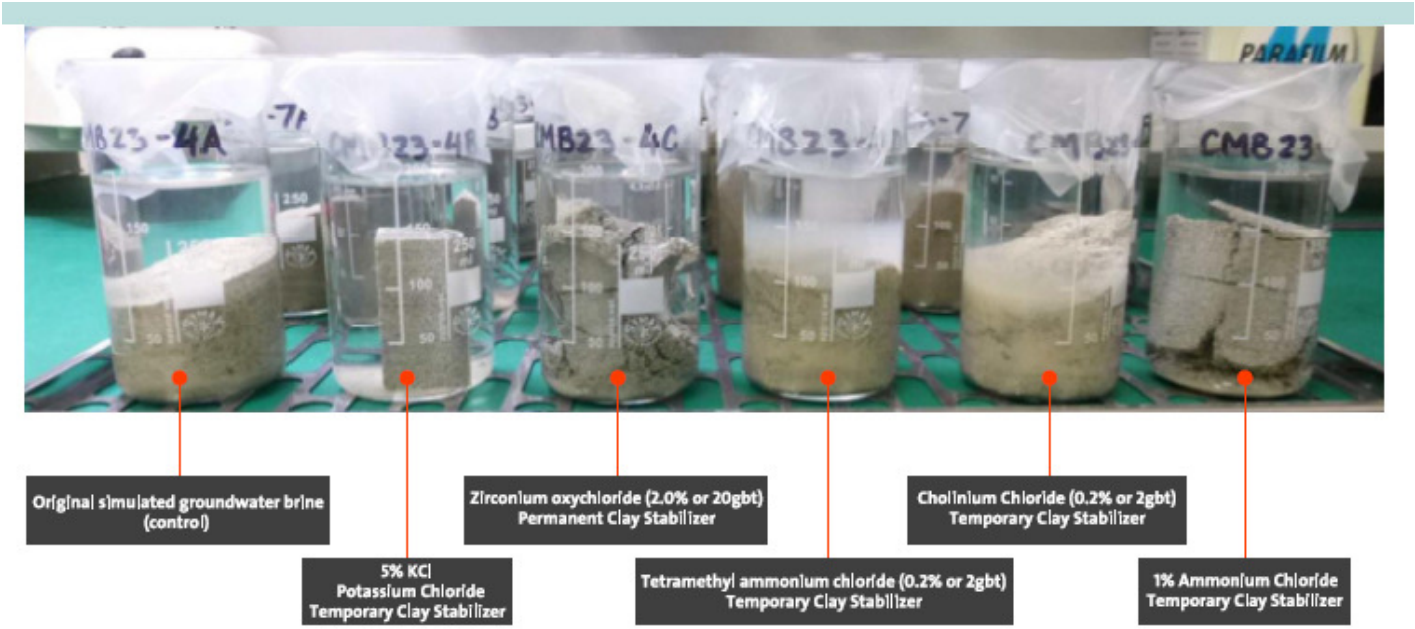

Figure 27: The samples after 5 days of saturation various clay stabilisation products. From left to right: Produced fluid, KCl (5%), L042 (2%), L064 (0.2%), L071 (0.2%) and ammonium chloride (1%). The L042, L064 and L071 are commercially available clay stabilisation products from Schlumberger. From the results, the KCl (5%) shows a mostly intact sample compared to the others, which range from total disaggregation (produced fluid, L071 and L064) to partial disaggregation (ammonium chloride and L042).

3.4 Discussion

One of the initial aims of this chapter was to establish root cause of solids production, which was undertaken using a total of eight tests and 81 samples. Although the number of samples is relatively small, the results appear convincingly indicative of the root cause of fines production. It becomes apparent that rock-fluid interaction is the most likely significant contributor to solids production. The key observation to support that supposition is that most rocks disintegrate in contact with produced water (re-constituted brine).

In the conditions under which rocks disaggregated to simulate well production, the samples became worse with all of the diluted solutions moving samples from partial disaggregation to total disaggregation. Importantly, observations from Condabri 23 (Figure 25) could not identify a specific lithology of the formation that may be more susceptible to solids production.

Consistently in all analyses, the samples exposed to synthetic brine experienced total disaggregation, whilst the samples exposed to 5% KCl were consistently relatively intact. KCl is easily deployable, as it is in use for most CSG drilling and completion operations.

More complex, commercially available clay stabilisation products showed mixed results from partial disaggregation to some total disaggregation of samples. Reducing the concentration of these solutions resulted in more samples experiencing total disaggregation, and thus suggesting these may have some potential benefit, however, benefits were not as significant as apparent for KCl.

The WSG has a significant volcanic overprint with volcaniclastics containing a large portion of smectite and swelling clays. The dissolution analysis suggests that the disaggregation may be dominantly due to dissolution from fluid-rock interaction. However, conventionally rock disintegration leading to fines production (or ‘sanding’) is analysed in a geomechanical context (i.e. stress around wellbore, rock-mechanical properties, uniaxial compressive strength (UCS) and FBHP (flowing bottom hole pressure)). The potential geomechanical contribution to fines production will be examined in Chapter 6 and Chapter 7.

The immediately following chapter will examine the basics of core facies, petrographic analyses and expand a little on the deposition model to potentially constrain the results we have seen in the rock-fluid interaction analysis.

Chapter 4 - Core and Petrographic Analysis

4.1 Introduction

The rock-fluid interaction is shown in the previous chapter to be the likely root cause of solids production. From the dissolution analysis (Chapter 3), the disaggregation of a number of samples was observed both vertically and laterally within the WSG when exposed to produced formation water.

From the dissolution analysis of 32 samples in Condabri 23 (Figure 25), 22 were completely disaggregated, 7 were partially disaggregated and 3 were mostly intact. The disaggregation was not confined to one particular lithology or formation. In order to establish any potential correlations and potential predictions, this chapter will investigate the stratigraphic framework using a detailed facies analysis to potentially understand and predict the dissolution.

The WSG is divided into the Juandah Coal measures, Tangalooma Sandstone and the Taroom Coal Measures. The upper and lower units are locally further subdivided. The WSG consists of a fluvio-lacustrine clastic succession with interspersed coal measures (Martin et al. 2013).

The majority of rocks in the WSG are coals, siltstones, mudstones and sandstones with abundant carbonaceous material, as well as a significant volcanic overprint (Martin et al. 2013). Volcanics are also evident in the petrography of the sands, which are volcanic lithic and contain a large portion of smectite in the matrix fraction (Yago 1996).

Most models for coal successions are derived from coastal settings or sections with marine influence. However, the WSG is entirely non-marine, which makes many depositional models inappropriate. In particular, sequence stratigraphic concepts developed for marine settings are difficult to apply to fluvio-lacustrine settings (Exon and Burger 1981).

As presented in the Geological Summary (Chapter 2), Boult et al (1998) propose that the deposition of the age equivalent Eromanga Basin, located further west of the Nebine Ridge (Figure 13), was dependent upon the sediment supply being controlled by a shifting balance between uplift on the eastern and south-western boundaries of the Australian plate (Boult et al. 1998). Cleaner reservoir quality sands were deposited when uplift on the rifting margin to the southwest was greatest. However, source rocks and sealing lithologies were primarily deposited when uplift and volcanic activity on the subducting margin to the east were greatest, which resulted in raising of drainage base levels and the spread of highly labile volcanic arc derived material across the basin (Boult et al. 1998).

Almost all of eastern Australia was in a backarc setting from the Early Jurassic to Early Cretaceous, with only minor remnants of the magmatic arc being preserved near the coast in Queensland (Waschbusch et al. 2009). Volcanism was pervasive

throughout the deposition of the WSG and overlying formations, whether this was intrabasinal (Fielding, 1996; Yago 1996) or extrabasinal (Boult et al. 1998) from the mid-Late Jurassic subduction-plate margin and arc to the east (Exon, 1976, Veevers, 1984, Hawlader, 1990, He and Conaghan, 1994, Turner et al., 2009).

Six sedimentary cycles were identified as a series of fining upwards cycles within the Surat Basin (Exon and Burger 1981). Each cycle consists of an upward succession of stratigraphy deposited by:

1. braided streams;
2. meandering streams, and;
3. Swamp lakes and deltas.

The effects of these modes of deposition varied from cycle to cycle.

4.2 Objective

This chapter aims to address the following key uncertainties with regards to the deposition of the WSG:

1. What is the variability in chemical and mineralogical rock composition, (both coals and interburden)?
2. What impact does rock composition have on fines production?
3. What is the proportion of swellable clays?
4. What is the in-principal type of grain cementation?
5. Do different lithologies correspond to different facies?
6. Are different rock compositions reflected in wireline log data?
7. What impact does rock composition have on:
    - strength;
    - propensity to produce fines;
    - porosity, and;
    - permeability.

Textural characteristics revealed by detailed petrologic analysis have a bearing on mechanical behaviour, rock strength and other rock properties. The purpose of the petrographic testing herein was to characterise the interburden using detailed petrology for textural characterisation. With adequate measurements of strength on core samples, and the available supplementary information (e.g. clay content), logging based predictions of rock strength may be possible. With such information, predictions of fines production and / or borehole stability, can be subsequently performed.

To address the above objective, five types of petrographic analysis were conducted using core samples from Condabri 21, Condabri 23, Condabri 140, Combabula 23 and Zig Zag 6.

1. X-ray diffraction (XRD).
2. Scanning electron microscope (SEM).
3. Thin section analyses (TSA).
4. Petrologic analyses and textural characterisation.
5. Grain size analyses and histograms by laser particle size analysis (LPSA).

4.3 Data Used

Core data were analysed from five CSG wells from the Walloons Fairway in the Surat Basin. When acquiring the core during drilling operations, the coal core was separated for desorption, and later re-united with the main core post slabbing and maceral analysis. Petrophysical data was collected using a high-resolution basic logging suite consisting of spontaneous potential (SP), density, gamma ray, array induction and two-arm caliper. Coal was distinguished from other lithologies on petrophysical logs by applying a density cut-off of less than 1.75 g / cc. Image logs were also run using Schlumberger's Formation Micro-Imager (FMI) tool at a high resolution acquisition rate (0.2 inch).

4.4 Facies

Three broad facies associations were identified within the WSG (Martin et al. 2013):

1. Primary channel facies association including massive sandstones, current rippled sandstones, laminated sandstones, conglomerates and slumped / distorted sandstones.
2. Overbank facies association which includes rippled sandstones and siltstones, laminated sandstone, diffused sandy heterolithics.
3. Volcanic extrusives.

These groups provide a robust stratigraphic framework that is used herein. More detailed work was done by Boyd et al (2016), but is outside the scope of this study. For this study, the five main facies types to characterise the depositional environments were selected from an internal report by Murphy (2012). The five facies types are shown in Chapter 2 (Figure 18) and are the following (Murphy 2012):

1. Fluvial channel.
2. Proximal floodplain – crevasse splay.
3. Distal floodplain – crevasse splay.
4. Peat swamps.
5. Lacustrine.

4.4.1 Fluvial Channel

Channel sandstone belt facies are characterised by a number of stacked fine to medium grained sandstone fluvial channels deposited with low sinuosity and densely vegetated banks. Coal spars, angular pebble clasts, irregular rip up clasts and rounded sideritised mud clasts can be found at the base of each individual deposit. The channels have abundant carbonaceous material and minimal preservation of overbank sediments (Murphy 2012).

The wireline response of the fluvial channel belt facies is characterised by a relatively high density (approximately 2.5 g / cm^3) and low gamma ray count (average of 60 API from the normalised gamma ray log) (Figure 33). This facies generally exhibits a gamma ray log response with a sharp base and, frequently, a

sharp top. The gamma log has a relatively consistent baseline over each multistorey channel sequence, which only shifts significantly in the presence of strongly carbonated cemented sandstone. The two types of the multistorey channel sequences are recognized on the resistivity logs: a resistivity response that shows no shift from the baseline resistivity and a higher resistivity sequence. No visible separation of the deep and the shallow resistivity curves is observed (Murphy 2012).

4.4.2 Proximal floodplain - Crevasse Splays

Proximal floodplain facies are interpreted from interbedded siltstone, sandstone and mudstone sediments deposited by crevasse splays (breaches of the fluvial channel margin that divert sediment onto the floodplain), splay channels, minor fluvial channels or sediments deposited during abrupt abandonment of a channel. Erosive splays deposit thin beds of very fine to medium grained sandstone often containing large rip-up clasts, coal spars and sideritised mudstone clasts (Murphy 2012).

Thinly bedded splay deposits are typically overlain by finer grained current ripple cross bedding, flaser bedding and horizontal planar lamination. Sections with thicker sandstone beds may represent abandoned channels, or may represent splay channels if there is significant variation in flow conditions over the sequence (large variation in grain size and sedimentary structures). Proximal floodplain facies exhibit soft sediment deformation in the form of synsedimentary faulting and convoluted bedding. Burrows and bioturbation can also be present (Murphy 2012).

Proximal floodplain facies are characterized by wireline logs as having:

1. Relatively high density (approximately 2.5 g /cm3).
2. Medium GR count (~80 API from normalised GR).
3. GR response is slightly jagged appearance.

4.4.3 Distal floodplain - Crevasse splays

Distal floodplain facies are characterised by mudstone and siltstone. Bedding can exhibit current ripple lamination, horizontal planar lamination, flaser and lenticular bedding with occasional ripple scale sand lenses. Paleosols are common and features include dispersive textures, pedogenetic slickensides, strongly rooted horizons, disturbed bedding, mottling, lightening in colour towards the top of the soil horizon and abundant carbonaceous material. Burrows and soft sediment deformation such as synsedimentary faulting are also frequently observed (Murphy 2012).

Distal floodplain facies are interpreted as sediments deposited during flooding and well developed densely vegetated water logged paleosols. Distal floodplain facies are predominantly comprised of mudstones deposited during flooding events and developed with densely vegetated water logged paleosols. Mature paleosols developed in a well vegetated water logged environments and can also include sediments deposited in floodplain lakes (Murphy 2012).

Distal floodplains facies are characterised by wireline logs as having:

1. Relatively high GR (average of 90 API from normalised GR).
2. Density log response is typically ~2.5 g/cm^3 but can vary between 1.75 – 2.5 g/cm^3 when carbonaceous mudstone is present.

4.4.4 Peat Swamps

Peat swamp facies are characterised by coal, often in association with tuff bands. Coals show considerable internal variability in colouring, cleat development and ash content. Calcite filling of cleats is common where coal cleats are well developed (Murphy 2012).

The presence of tuff bands within the coal indicates a volcanically active regional setting. Pyroclastic debris has a much higher chance of preservation within the low energy peat swamp environments (tuff washed away or mixed with other sediments in other facies) (Murphy 2012).

The wireline log response for peat swamp facies is usually a relatively low gamma log (average of 60 API for the nomalised gamma log) and a low density response (average of approximately 1.70 g / cm^3) (Murphy 2012).

4.4.5 Lacustrine (lake environment)

Lacustrine facies are characterised by fine grained sediments with flat bedding and a lack of roots as well as profuse carbonaceous material. The wireline log response is usually a relatively high gamma log (average of 90 API for the normalized gamma log and a relatively high density log response (approximately 2.5 g / cm^3) (Murphy 2012).

The facies often occur in the following chronological (depositionally upwards) sequence (Figure 21):

1. Stacked channel belt facies.
2. Proximal floodplain with isolated channel facies.
3. Peat facies.
4. Distal floodplain.
5. Often a second peat unit at the top.

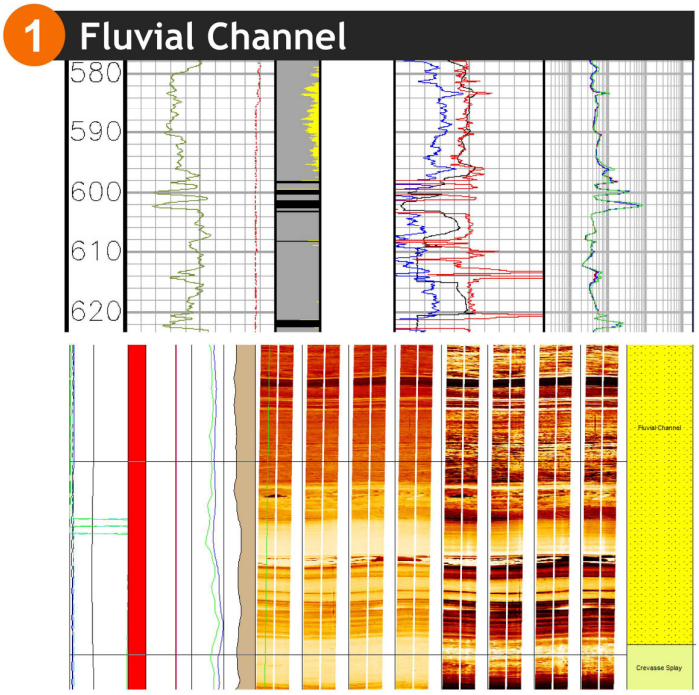

Figure 28: Fluvial channel facies interpreted from wireline logs with the following features: relatively high density (~2.5g/cm^3) and low GR (~60API). The GR shows a sharp base and sharp top. The image log display shows the bedding orientation.

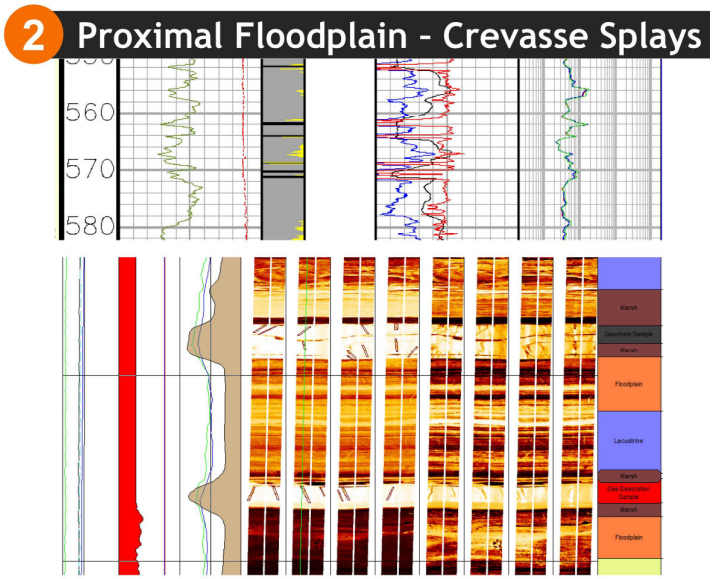

Figure 29: A proximal floodplain (crevasse splay) interpreted from wireline logs with the following features: relatively high density (~2.5g/cm^3) and medium range GR (~80API). The GR log is slightly jagged in appearance. The image log displays the bed boundary.

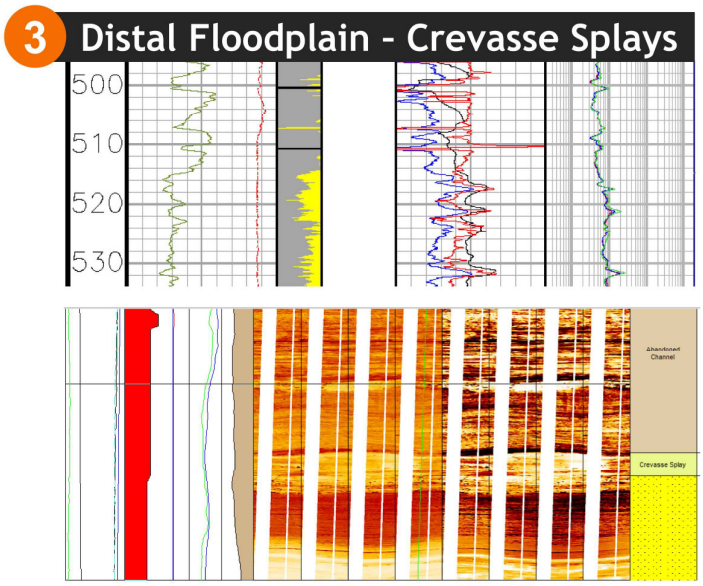

Figure 30: The distal floodplain (crevasse splay) interpreted from wireline logs with the following features: varying density values (~1.75 g/cm^3 - 2.5g/cm^3) and high range GR (~90API). The low density is influenced by carbonaceous material. The image log displays the bed boundary.

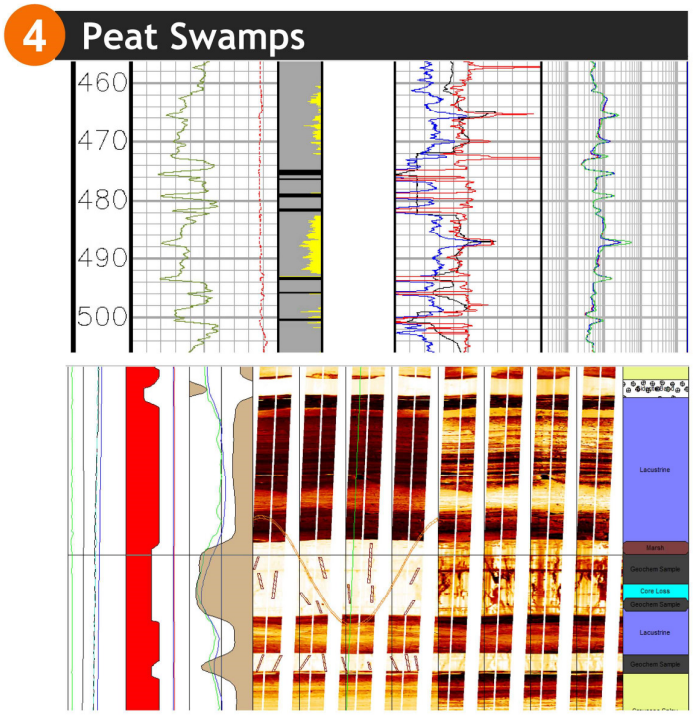

Figure 31: Peat swamp facies interpreted from wireline logs with the following features: low density (average 1.70 g/cm^3) and low GR (~60API). There are some tuff bands observed (higher GR) in low energy peat swamps. The image log shows coals and tuff bands (volcanics).

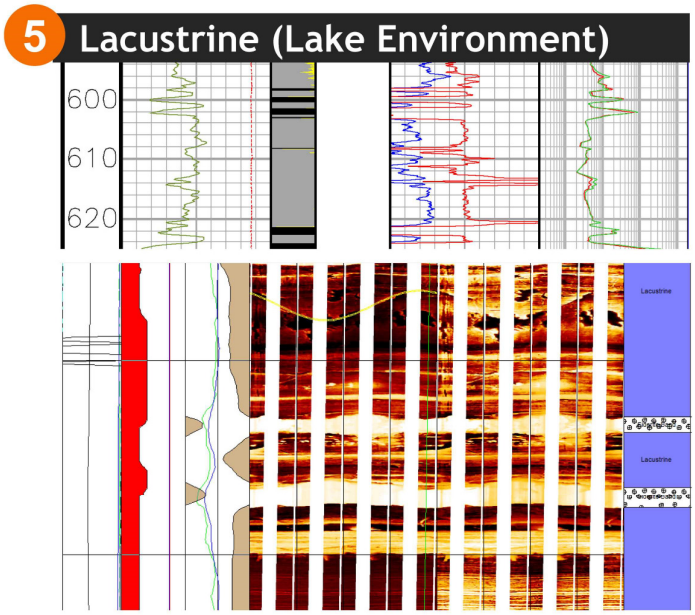

Figure 32: Lacustrine (lake environment) facies are interpreted from wireline with the following features: relatively high density (~2.5g/cm^3) and high GR (~90 API). The GR shows a sharp base and a sharp top. The image log is interpreted as flat bedding indicating a low energy deposition environment.

4.5 Petrographic Analysis - X-Ray Diffraction (XRD)

The purpose of petrographic testing was to characterise the interburden with detailed petrology to look at any potential areas which may be conducive to fines production. Coal samples were not analysed for this work. The samples were selected to characterise the facies observed in the WSG.

To address the objectives outlined earlier in the chapter, the following five petrographic analyses were conducted using core samples from Condabri 21, Condabri 23 and Condabri 140:

1. X-ray diffraction (XRD).
2. Scanning electron microscopy (SEM).
3. Thin section analyses (TSA).
4. Petrologic analyses and textural characterisation.
5. Grain size analyses and histograms (LPSA).

Whole core samples were provided from Condabri 21, Condabri 23 and Condabri 140 from within the Condabri Field. Additional data was used from Combabula 23, Zig Zag 6 and Ramyard 19IS to examine lateral extent.

Table 6: Table of petrologic samples from Condabri 21, Condabri 23 and Condabri 140.

Well	Sample ID	Depth (m RT)	Facies	Lithotype	TS[1]	SEM[2]	XRD[3]	Comment
Condabri 21	CB21-1	699.54	Fluvial Channel				X	Springbok SST
	CB21-2	804.45	Lacustrine				X	
	CB21-3	804.45	Lacustrine	Litharenite	X	X		
	CB21-4	858.90	Peat				X	
	CB21-5	917.90	Crevasse Splay				X	
	CB21-6	917.90	Crevasse Splay	Litharenite	X	X		
	CB21-7	987.47	Fluvial Channel				X	
	CB21-8	1053.86	Lacustrine				X	
	CB21-9	1053.86	Lacustrine	Litharenite	X	X		
Condabri 140	CB140-30	511.34	Abandoned Channel				X	Springbok SST
	CB140-31	511.43	Abandoned Channel	Litharenite	X	X		Springbok SST
	CB140-32	585.56	Fluvial Channel				X	
	CB140-33	603.30	Lake with pedogenic overprint				X	
	CB140-34	647.45	Fluvial Channel				X	
	CB140-35	705.40	Marsh				X	
	CB140-37	710.05	Abandoned Channel				X	
	CB140-36	710.15	Abandoned Channel	Argillaceous Mudstone	X	X		
	CB140-38	775.09	Peat				X	
	CB140-39	820.93	Marsh				X	
	CB140-40	873.30	Peat				X	
	CB140-41	873.37	Marsh	Argillaceous Mudstone	X	X		
Condabri 23	CB23-2	335.43	Marsh				X	
	CB23-10	414.50	Crevasse Splay				X	
	CB23-12	436.90	Lacustrine				X	
	CB23-21	523.70	Fluvial Channel				X	
	CB23-24	541.74	Crevasse Splay				X	
	CB23-27	557.44	Crevasse Splay				X	
					6	**6**	**21**	

1 – TS = Thin Section Analysis; 2 – SEM = Scanning Electron Microscopy; 3 – XRD = X-Ray Diffraction;

4.5.1 XRD - Bulk Analysis

The core element of X-ray diffraction (XRD) is related to X-rays scattered by electrons. This phenomenon is referred to as Thomson scattering (Waseda et al. 2011). Scattering occurs when X-ray beams are emitted from matter irradiated with a beam of X photons. The scattered energy is very small but the scattered waves interfere to give rise to diffracted waves with higher intensities. The analysis of the diffraction figure, the analysis of the distribution in space of the diffracted intensity, makes it possible to characterise the structure of the studied material (Guinebretière 2013).

The XRD involved bulk analysis using representative splits of the selected samples. The bulk samples were ground down and the powdered samples analysed using an x-ray diffractometer. The bulk analysis of the raw data was interpreted to identify the mineralogy based on peak profile fitting and whole pattern fitting methods. This analysis yields semi-quantitative analysis of the whole rock and best characterises overall mineralogy and amount of clay in the bulk sample.

Clay analysis requires further preparation of the bulk samples to be crushed and disaggregated to obtain a sample less than 4 microns. Clay minerals were identified, and their approximate weight percentages (wt %) determined by comparison with mixtures of standard clay minerals in known percentages. XRD analysis of the clay size fraction yields the relative abundance of the clay minerals and determines the amount of expandability (amount of swelling clay) in the mixed-layer clays. The amount of discrete smectite and interlayered smectite (swelling clay) in mixed-layer clays was used to determine the percent expandability of the bulk samples.

Table 7: X-Ray Diffraction Data – whole rock and clay mineralogy (Weight %) with the relative clay abundance shown as a percentage of the total clay abundance of <4 microns (Weight %).

WHOLE ROCK MINERALOGY																					CLAY MINERALOGY																			
																					Relative Clay Abundance in Bulk Sample									Relative Clay Abundance (<4 Microns)								
WELL ID	SAMPLE ID	DEPTH (m)	QUARTZ	K-FELDSPAR	PLAGIOCLASE	CALCITE	SIDERITE	ANKERITE/ FE-DOLOMITE	DOLOMITE	PYRITE	BARITE	MAGNETITE	TOTAL NON-CLAY	SMECTITE	ILLITE/SMECTITE (I/S)	ILLITE+MICA	KAOLINITE	CHLORITE	TOTAL CLAY	GRAND TOTAL	SAMPLE ID	DEPTH (m)	% I/S EXPANDABILITY	SMECTITE	ILLITE/SMECTITE (I/S)	ILLITE+MICA	KAOLINITE	CHLORITE	TOTAL EXPANDABLE CLAY	SAMPLE ID	DEPTH (m)	% I/S EXPANDABILITY	SMECTITE	ILLITE/SMECTITE (I/S)	ILLITE	KAOLINITE	CHLORITE	TOTAL CLAY
Condabri-23	CB23-2	335.43	32	5	18	4	2	0	0	0	2	0	63	10	3	2	8	15	37	100	CB23-2	335.43	50	26	8	5	22	39	11	CB23-2	335.43	50	65	21	3	8	4	100
	CB23-10	414.50	20	0	6	26	28	1	0	0	0	0	82	0	0	4	0	15	19	100	CB23-10	414.50	50	0	0	20	0	80	0	CB23-10	414.50	50	23	44	13	15	6	100
	CB23-12	436.90	44	6	11	1	2	0	0	0	2	0	65	1	4	3	15	13	35	100	CB23-12	436.90	50	2	10	7	43	37	3	CB23-12	436.90	50	6	27	6	40	21	100
	CB23-21	523.70	48	0	20	0	0	0	0	0	0	0	69	0	0	10	5	16	31	100	CB23-21	523.70	50	0	0	32	16	52	0	CB23-21	523.70	50	16	21	11	25	27	100
	CB23-24	541.74	40	5	28	4	3	0	0	0	1	1	82	1	0	4	5	7	18	100	CB23-24	541.74	50	5	2	24	29	40	1	CB23-24	541.74	50	72	21	1	4	2	100
	CB23-27	557.44	40	4	12	1	2	2	0	0	2	0	62	2	6	6	11	13	38	100	CB23-27	557.44	50	4	15	17	30	34	4	CB23-27	557.44	50	4	16	11	44	25	100
Condabri-21	CB21-1	699.54	67	2	5	14	0	0	1	0	0	0	90	0	0	0	7	3	10	100	CB21-1	699.54	30	0	0	0	67	33	0	CB21-1	699.54	30	8	10	5	49	30	100
	CB21-2	804.45	36	7	8	1	1	5	0	0	1	0	60	7	8	3	13	10	40	100	CB21-2	804.45	50	16	19	7	33	24	10	CB21-2	804.45	50	37	43	6	8	7	100
	CB21-4	858.90	34	3	11	4	4	2	0	0	2	0	59	10	5	2	9	14	41	100	CB21-4	858.90	50	25	13	6	22	35	13	CB21-4	858.90	50	36	19	5	21	20	100
	CB21-5	917.90	34	4	8	0	0	0	0	0	5	0	50	2	17	0	19	11	50	100	CB21-5	917.90	45	5	35	0	38	22	10	CB21-5	917.90	45	6	41	12	27	14	100
	CB21-7	987.47	38	4	29	4	2	0	0	0	1	1	79	0	0	4	11	7	21	100	CB21-7	987.47	50	0	0	18	51	31	0	CB21-7	987.47	50	61	26	1	8	5	100
	CB21-8	1053.86	30	10	9	9	2	0	5	0	1	0	66	0	1	2	19	12	34	100	CB21-8	1053.86	40	0	3	5	57	35	1	CB21-8	1053.86	40	1	17	12	50	19	100
Condabri-140	CB140-30	511.34	38	4	16	0	0	0	0	0	1	0	60	4	6	14	8	8	40	100	CB140-30	511.34	50	10	16	34	20	20	7	CB140-30	511.34	50	35	53	2	6	5	100
	CB140-32	585.56	26	7	16	28	0	1	4	0	1	0	82	2	1	6	4	7	18	100	CB140-32	585.56	45	9	4	32	20	35	2	CB140-32	585.56	45	57	22	2	12	6	100
	CB140-33	603.30	25	2	9	39	0	2	0	0	2	0	76	0	0	3	9	11	23	100	CB140-33	603.30	50	0	0	14	38	48	0	CB140-33	603.30	50	18	14	9	36	23	100
	CB140-34	647.45	27	11	17	1	0	0	0	0	1	0	56	6	10	6	12	10	44	100	CB140-34	647.45	50	14	22	14	28	22	11	CB140-34	647.45	50	30	47	4	10	10	100
	CB140-35	705.40	36	4	9	0	11	5	0	0	0	0	65	0	3	3	12	16	35	100	CB140-35	705.40	55	1	9	7	35	47	2	CB140-35	705.40	55	7	44	15	16	20	100
	CB140-37	710.05	38	8	10	1	2	0	1	0	1	0	60	1	5	6	12	15	40	100	CB140-37	710.05	55	2	14	16	31	38	4	CB140-37	710.05	55	8	53	15	11	13	100
	CB140-38	775.09	36	4	27	4	1	5	0	0	1	0	78	0	0	5	9	8	22	100	CB140-38	775.09	55	0	0	20	43	37	0	CB140-38	775.09	55	38	18	3	22	18	100
	CB140-39	820.93	36	3	7	8	0	0	0	0	2	0	56	1	8	9	16	10	44	100	CB140-39	820.93	55	3	18	20	36	23	6	CB140-39	820.93	55	8	48	12	23	9	100
	CB140-40	873.30	36	6	10	1	4	0	0	0	1	0	57	1	6	13	12	12	43	100	CB140-40	873.30	50	2	13	29	28	27	4	CB140-40	873.30	50	8	58	10	16	9	100

4.5.2 Total Expandable Clay

Smectites are a group of clay minerals that show expandability, taking up water or organic molecules between their structural layers and also marked cation exchange properties. Smectites form in sedimentary deposits by diagenetic / hydrothermal processes which can either involve transformation of precursor clay or non-clay material or neoformation from solutions or colloids (Deer et al. 1992).

In general, smectite is only found in sedimentary rocks at relatively shallow depths, as smectite generally undergoes diagenesis into illite, illite / smectite (I/S) mixed layers or chlorite with increasing depth and temperature. Most natural samples of illite contain smectite layers (montmorillonite / beidellite) that may be regularly or randomly interstratified. An illite / smectite (I/S) mixed layer aggregate is in fact the most abundant clay mineral constituent of sedimentary rocks (Deer et al. 1992).

The total expandable clay is calculated from the percentage of smectite in the mixed-layer illite / smectite (I/S) clay. The total expandable clay in the XRD table above (Table 7) represents the total amount of expandable clay for the whole rock from smectite and also the expandable clay component from illite / smectite.

The percentage of smectite (expandable) interlayers in the mixed-layer illite-smectite (I/S) clay is determined by the position of the main I/S clay peak in the air-dried pattern and how the peak shifts (to a higher spacing) in the glycolated pattern. The percent expandability represents the total amount of swelling clay in the whole rock sample. This is determined from the amount of discrete smectite and interlayered smectite in mixed-layer clays and how much of these clays are in the whole rock sample. For example, a bulk sample with 25 percent mixed-layer illite-smectite composed of 20 percent interlayered smectite has approximately 5 percent total expandable clay.

4.5.3 Results

The total clay from the bulk analysis ranged from 10% - 50%. The illite / smectite expandability (I/S expandability) from the clay analysis ranged from 30% to a maximum of 55%. The clay mineralogy (<4 microns) showed the smectite range from 1% - 72% and the illite / smectite (I/S) ranged from 10% to 58%. The analysis suggests clays would generally be considered moderately to highly expandable and sensitive to fresh water.

4.6 Scanning Electron Microscope

Scanning electron microscopy is performed at high magnifications, generating high-resolution images, and precisely measures very small features and objects. This has been conducted in the sample set to demonstrate the vertical distribution and variability identified from the core analysis.

Scanning Electron Microscopy (SEM) uses a focused beam of high-energy electrons to generate a variety of signals at the surface of solid specimens. In most SEM microscopy applications, data is collected over a selected area of the surface of the sample and a two-dimensional image is generated that displays spatial variations in properties including a chemical characterisation, texture and orientation of materials.

The SEM is also capable of performing analyses of selected point locations on the sample. This approach is especially useful in qualitatively or semi-quantitatively determining chemical compositions, crystalline structure and crystal orientations.

The energy dispersive X-ray spectroscopy (EDS) detector separates the characteristic X-rays of different elements into an energy spectrum and EDS system software is used to analyze the energy spectrum in order to determine the abundance of specific elements. A typical EDS spectrum is portrayed as a plot of X-ray counts versus energy (in keV).

Energy peaks correspond to the various elements in the sample. Energy Dispersive X-ray Spectroscopy can be used to find the chemical composition of materials down to a spot size of a few microns and to create element composition maps over a much broader raster area. Together, these capabilities provide fundamental compositional information for a wide variety of materials, including polymers and metals.

A small, freshly broken portion of each sample was mounted on a standard SEM mount and sputter-coated with gold or platinum/palladium for approximately 60 seconds. The samples were then placed in a field emission scanning electron microscope equipped with an energy dispersive X-ray spectrometer (EDX) or a cold cathode field emission scanning electron microscope. The samples were examined, and imaged at a range of magnifications to document the morphology of the rock fabric and the pore system.

None of the sand grains show any traces of overgrowth quartz cement, and the only silicification recognized in these samples is the microcrystalline quartz from devitrification of volcanic glass. This type of fine silicification partially supports the framework grains (Figure 35).

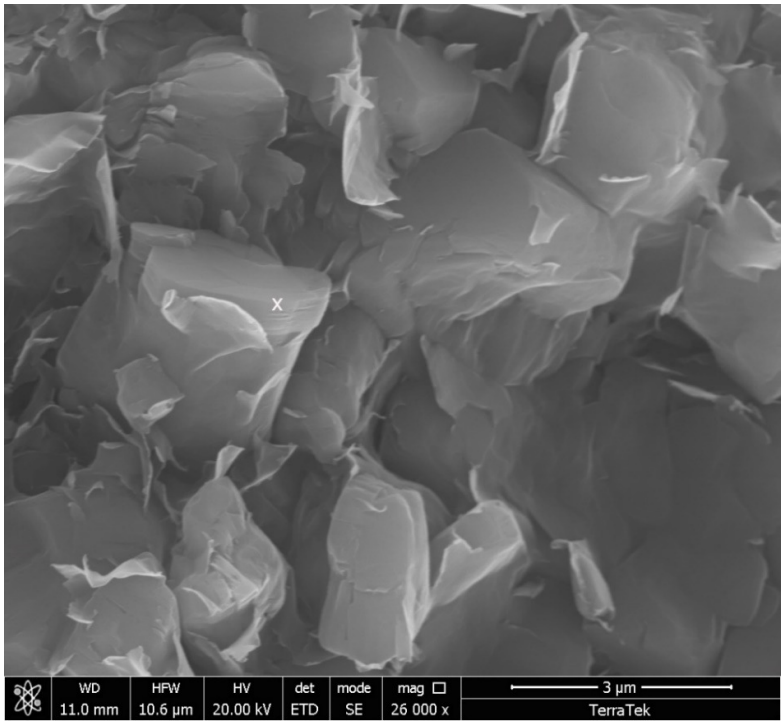

Figure 33: Litharenite sandstone. High magnification view of the argillaceous matrix shows the characteristic webby morphology of smectite clay. XRD indicates subsequent amounts of discrete smectite and smectite rich illite-smectite in the sample. (Scale bar = 3 microns)

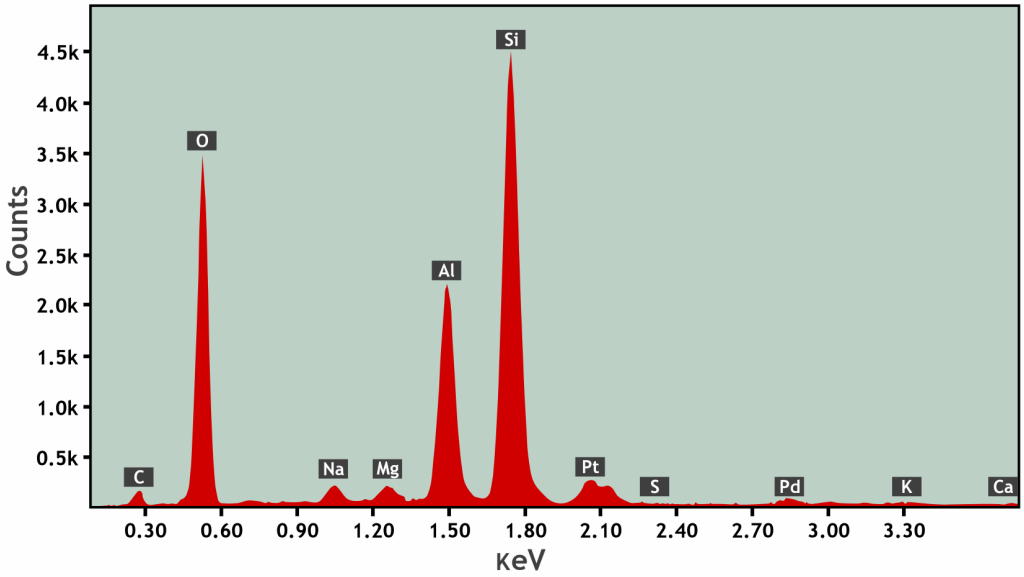

Figure 34: Spot elemental analysis from the litharenite sandstone above. The webby clay reveals an aluminosilicate composition with minor sodium and magnesium that is indicative of smectite.

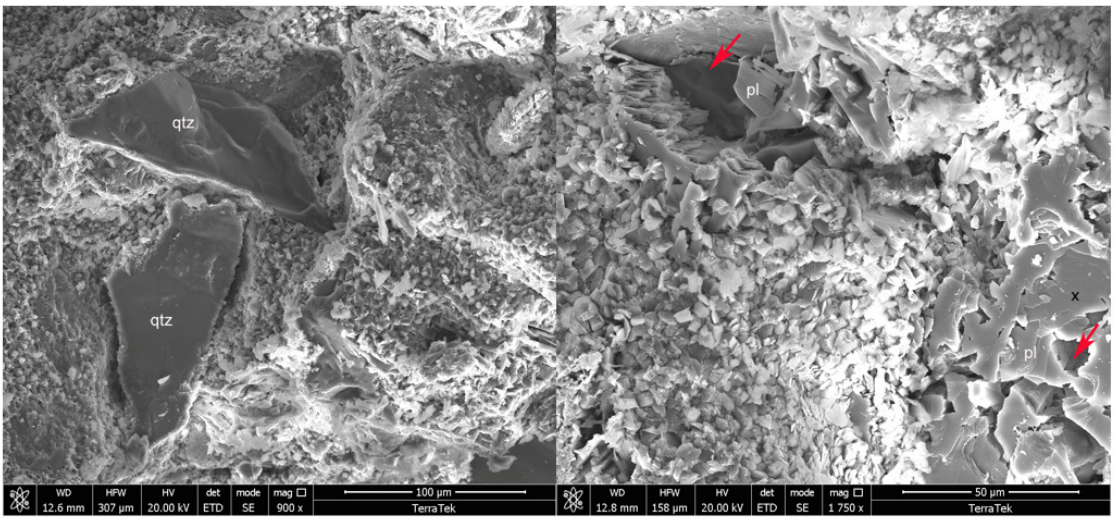

Figure 35: There are no traces of overgrowth quartz cement. The only silification is the microcrystalline quartz from devitrification of the volcanic glass.

4.7 Thin Section Analysis

Unique information regarding reservoir quality, heterogeneity and rock composition can be gained from petrographic analysis of thin sections made from core. Petrographic analysis can be performed on samples from conventional cores, sidewall cores or cutting but the quality with vary considerably (Morton-Thompson and Woods 1993).

The thin sections were taken from core samples and impregnated with a low-viscosity fluorescent red dye epoxy resin under vacuum to highlight porosity. The prepared sections were examined and digitally imaged at various magnifications under plane-polarised light and cross-polarised light.

Based on the textures shown in the thin section analysis from Condabri 21 and Condabri 140, the samples contain an abundance of clay, silica and partially dissolved volcanic grains that are tightly packed between quartz grain crystals.

The plane polarised thin sections showed very fine sandstone to siltstone with floating white quartz grains in a volcanic derived fabric. Most of the grains between the individual quartz grains are composed of glassy volcanic rock fragments that are partially devitrified and altered to chert and clay. Detrital biotite and chloritised mica plates are also present and are associated with ash-flow tuff deposits.

Some samples showed detrital organic particles, which appeared mostly unaltered or immature, and most of the organic material appears to have a continental source. There was also evidence of porous woody fragments and other organic debris that are stringy to fibrous, as well as some that may represent pollen.

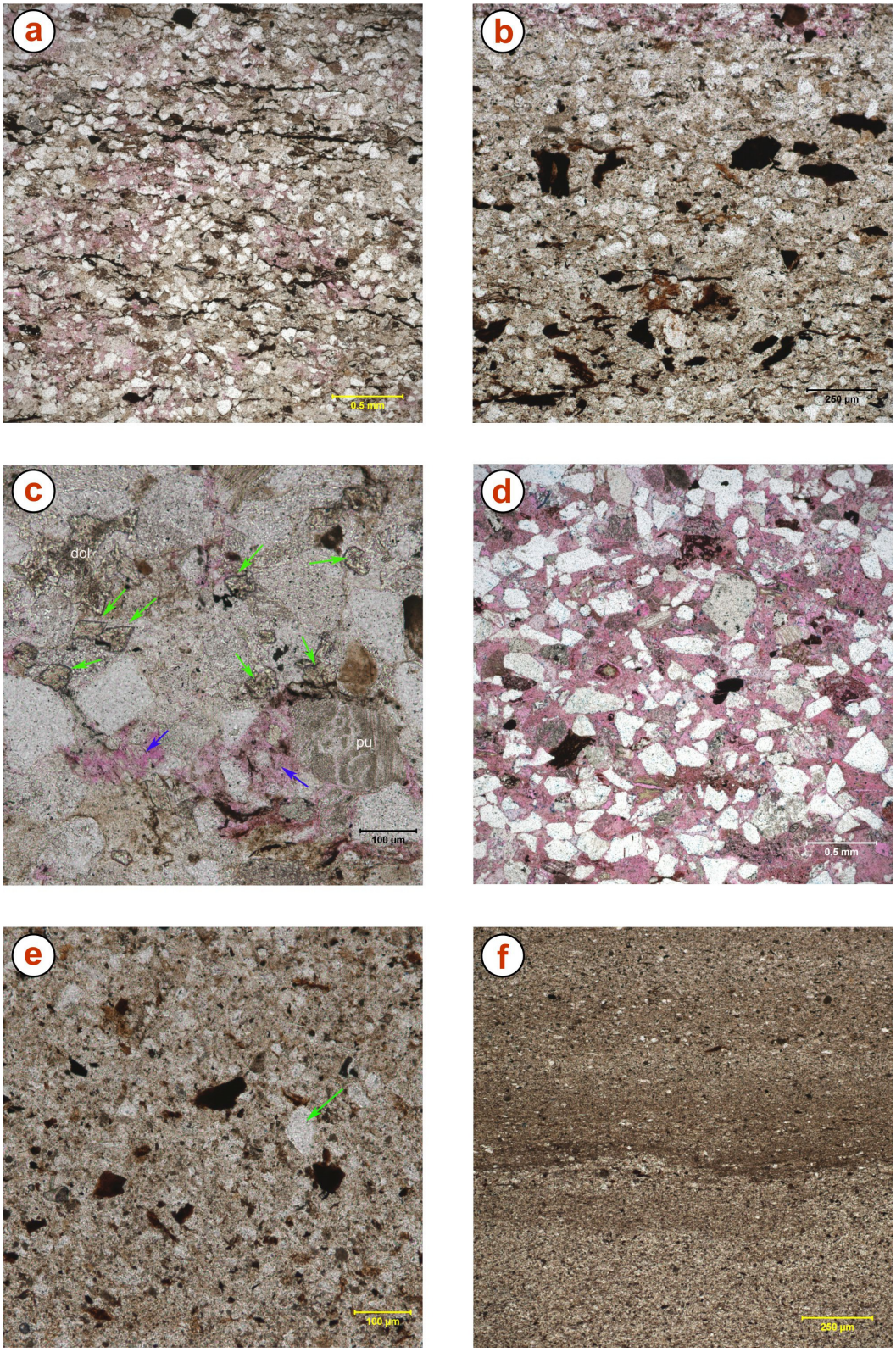

Figure 36: Thin section analysis of six samples from Condabri 21 and Condabri 140, as discussed in detail below.

a) Condabri 21 – Lacustrine facies (804.45 m) litharenite sandstone. A plane polarised light image showing very fine sandstone to siltstone with floating white quartz grains in an unsorted fabric. Most of the grains between the quartz grains are composed of glassy volcanic rock fragments that are partially devitrified and altered to chert and clay. Pink epoxy represents patches of secondary porosity in the siltstone. Long, compressed organic particles occur along bedding planes in silty layers. The sample remained competent after brine saturation and XRD identified 37% smectite from the <4 microns analysis. (Scale bar = 0.5 mm)

b) Condabri 21 – Crevasse splay facies (917.90 m) litharenite siltstone to silty argillaceous mudstone. A plane polarised image showing poorly sorted silt grains and fragments of plant material scattered throughout the mudstone. Much of the clay matrix could be tuffaceous in origin. The sample remained competent after brine saturation and XRD identified 6% smectite from the <4 microns analysis. (Scale bar = 250 microns)

c) Condabri 21 - Sample 21-9 (1053.86 m) litharenite sandstone. Plane polarized light shows the glassy volcanic grains with flow banding and may represent altered pumice fragments (pu). The green arrows point to prismatic football-shaped authigenic siderite crystals. Blue arrows show areas of secondary dissolution porosity within partially leached volcanic grains. The sample remained competent after brine saturation and XRD identified 1% smectite from the <4 microns analysis. (Scale bar = 100 microns)

d) Condabri 140 - Sample 140-3 (511.43 m) litharenite sandstone. Plane polarized light shows poorly sorted tuffaceous sandstone with floating subangular quartz grains or crystals (white), cherty silicified volcanic rock fragments (gray), non-degraded organic particles (orange-brown), and abundant partially devitrified and dissolved fragments of volcanic glass. The magenta epoxy indicates that the volcanic ash grains are mostly dissolved and porous, which accounts for the apparent floating texture of the quartz grains. The sample disaggregated after brine saturation and XRD identified 35% smectite from the <4 microns analysis. (Scale bar = 0.5 mm)

e) Condabri 140 - Sample 140-36 (710.15 m) argillaceous mudstone. Plane polarised light shows moderate amounts of fine quartz (irregular white areas) within the matrix. The quartz and clay within the matrix may represent devitrified volcanic ash, and this could be a tuffaceous mudstone. Other detrital material includes abundant fine organic particles, and plagioclase crystal grains (green arrow) that could also be derived from a volcanic source. The sample partially disaggregated after brine saturation and XRD identified 8% smectite from the <4 microns analysis. (Scale bar = 100 microns)

f) Condabri 140 - Sample 140-41 (873.37 m) argillaceous mudstone. The plane-polarised light shows clay drapes on subtle ripples. If this is a tuffaceous mudstone, then the tuff was water-lain, significantly reworked, and mixed with organic particles during deposition. The sample partially disaggregated after brine saturation and XRD identified 8% smectite from the <4 microns analysis. (Scale bar = 250 microns)

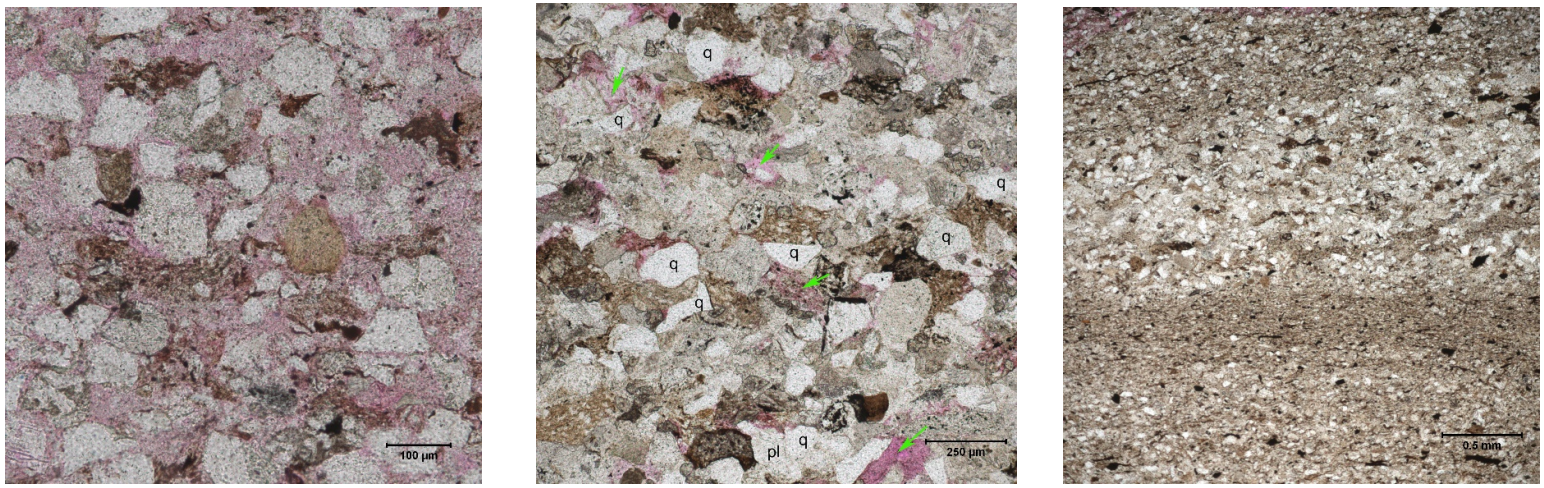

Figure 37: Thin section analysis over various intervals. From left: Condabri 21 (804.45m) - Litharenite sandstone with pink tuffaceous material, white is devitrified glassy volcanic grains; Centre: Condabri 21 (1053.86m) – Litharenite sandstone with green arrows showing partially dissolved volcanic grains. Right: Condabri 21 (917.90m) Litharenite sandstone with no clays evident, however from XRD analysis, this sample returned 50% clay with kaolinite and smectite rich with illite / smectite as the dominant clay types.

4.8 Laser Particle Grain Size Analysis (LPSA)

The particle size distribution of sediments was determined using laser light diffraction to measure the amount and patterns of light scattered by a particle's surface. The measured sizes were summarised into a grain-size scale for sediments showing Wentworth size classes.

Median grain size and sorting were determined from a modal (point count) analysis performed on the sandstone thin section samples. Results for the sandstones indicate median grain sizes of coarse silt to fine sand (4.16 to 2.72Φ; 0.06 - 0.15 mm). Overall, grains are moderately sorted (0.67-0.75Φ). Grain size distribution histograms are primarily unimodal (Figure 38).

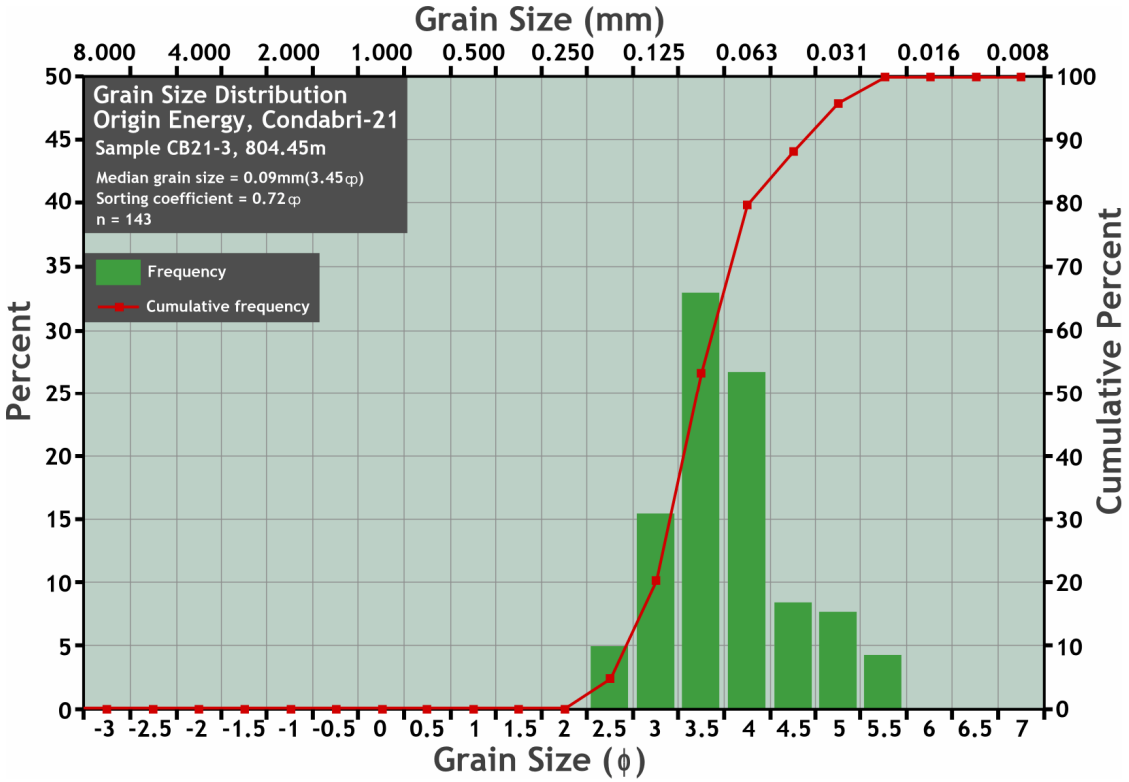

Figure 38: Sample Condabri 21-3 at depth 804.45m. This sample is a very fine sandstone with a litharenite composition.

The volcanic rock fragments are generally rounded to subrounded where the original grain boundaries can be distinguished. Larger glassy pumice fragments are evident as long stretched particles. From the degree of sorting, clay content, lithic components, and grain angularity as indicators of sediment maturity, the sandstones are considered texturally immature to submature. The tuffaceous deposits appear to have been waterlain and minimally reworked.

A moderate amount of natural compaction is observed where the more ductile clay-altered, microporous volcanic rock fragments are compressed between the quartz grains. In places, the tuffaceous material forms a compressed pseudomatrix between the stronger crystal grains. The pseudomatrix occludes primary intergranular pores and primary porosity appears to have been very low. The quartz crystal grains and clayey volcanic rock fragments are organised into laminations and admixed with woody plant material. In places, the quartz grains appear to 'float' where they are surrounded with microporous volcanic grains.

The clay-altered volcanic rock fragments make it difficult to distinguish from the clay-altered ash in the matrix. The compaction of ductile rock fragments, mica flakes and clay aggregates into the adjacent open intergranular pore space create a pseudomatrix. A few of the samples classed as sandstones are mostly matrix-supported and could classified as silty/sandy argillaceous mudstones. From the corresponding XRD samples, the total clay content is considered high, ranging from 34-50% of the whole rock composition. The kaolinite content comprises 8-19% of the sandstone composition and chlorite comprises of 8-11% of the whole rock composition of the siltstone and sandstone samples.

The volcanic overprint is evident in the modal porosity that varies from 10 to 18%, and is mostly represented by completely dissolved, to almost completely dissolved volcanic grains. These are shown as secondary dissolution pores and most are clusters of micropores at the sites of previous grains with poor interconnectivity among the adjacent pores. The main contribution to the overall porosity is from partially blocky grain dissolution pores and clay (or matrix) hosted micropores. Very few open intergranular pores are found in the sandstone samples and only in the coarsest laminations. It is important to note that modal analysis only counts some of the secondary dissolution micropores encountered in thin section.

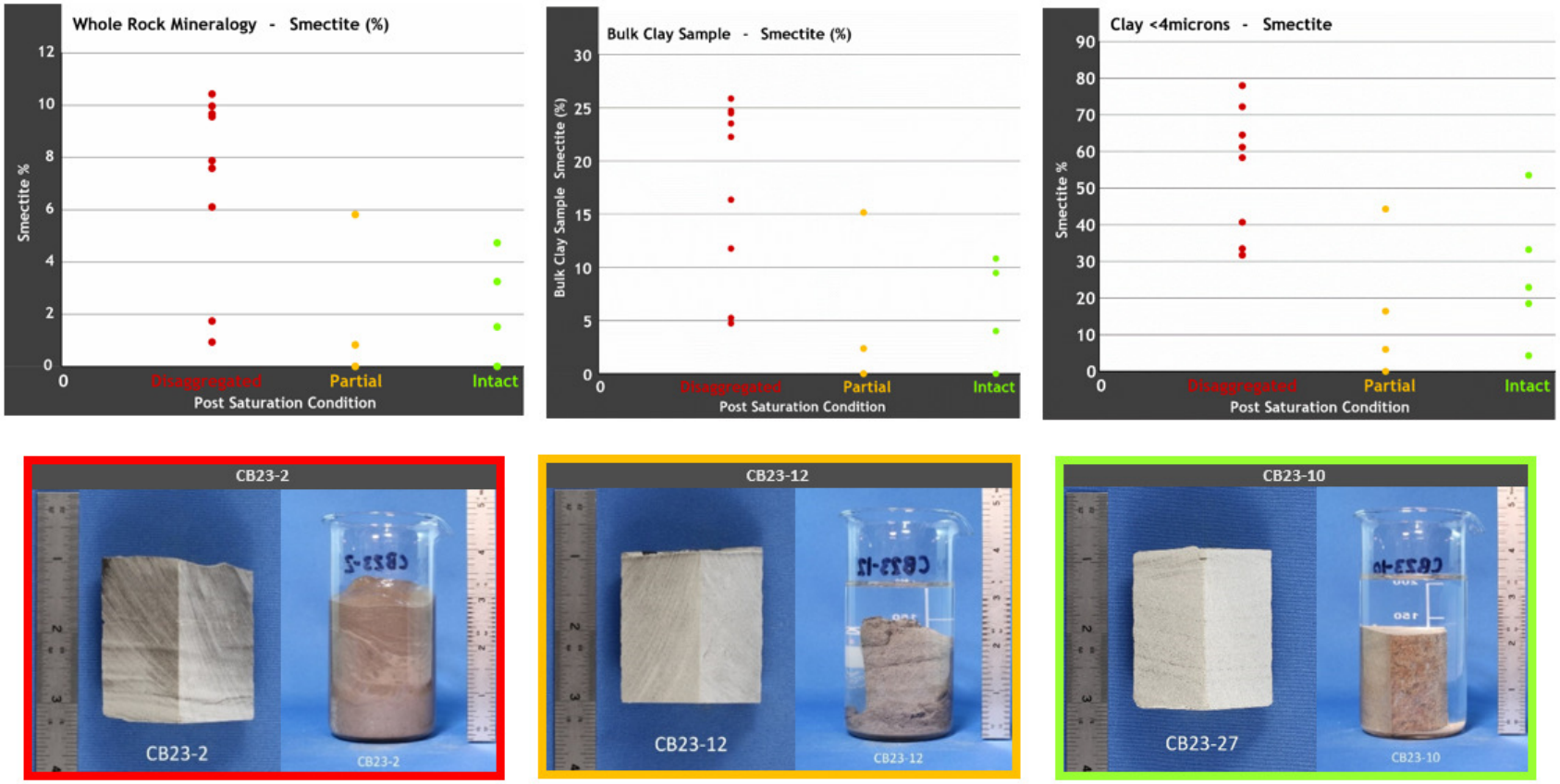

Figure 39: Dissolution analysis (from Chapter 3) plotted with the XRD results from the whole rock mineralogy of smectite percentage from the bulk sample (top left), the relative clay abundance in the bulk sample of smectite percentage (top middle) and the relative clay abundance (<4 microns) of the smectite percentage (top right). From the plotted results, there is no clear threshold of clay content for sample disaggregation.

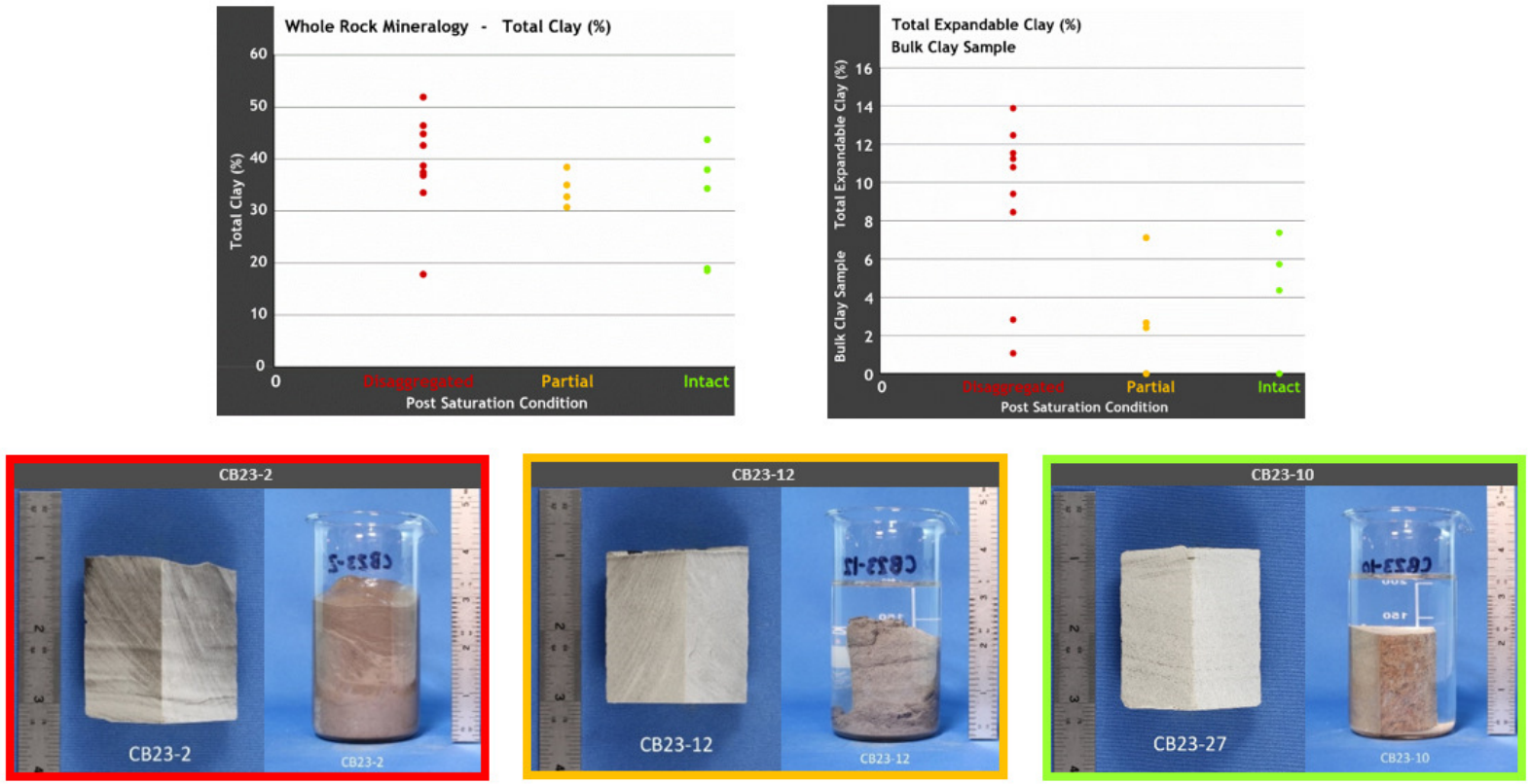

Figure 40: Dissolution analysis plotted with the XRD results of the total clay percentage (top left) and the total expandable clay percentage from the relative clay abundance in bulk samples (top right). From the plotted results, there is no clear threshold of clay content for sample disaggregation.

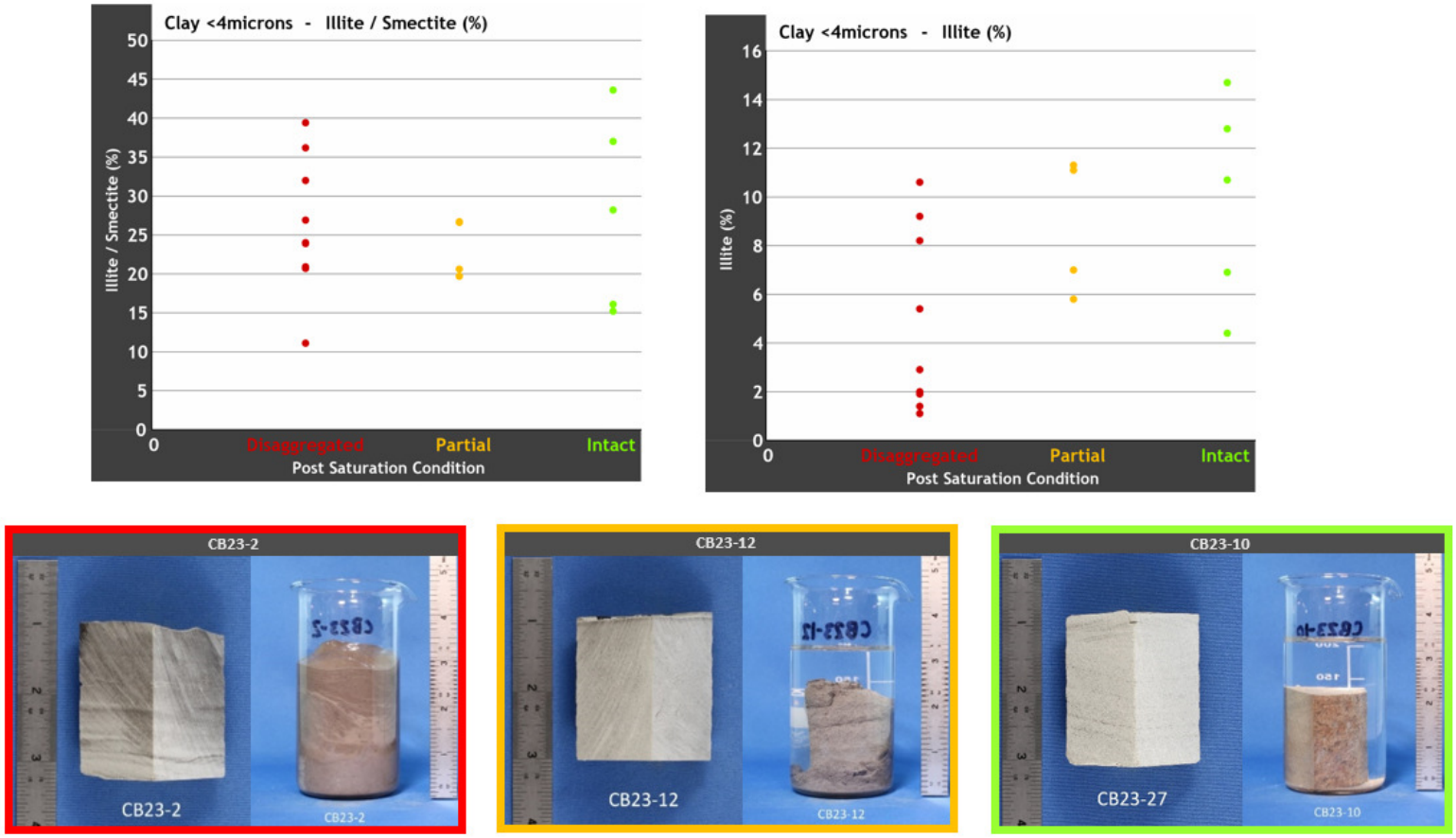

Figure 41: Dissolution analysis (from Chapter 3) plotted with the XRD results from the clay mineralogy (<4 microns) showing the illite / smectite percentage (top left) and the illite percentage (top right). From the plotted results, there is no clear threshold of clay content for sample disaggregation.

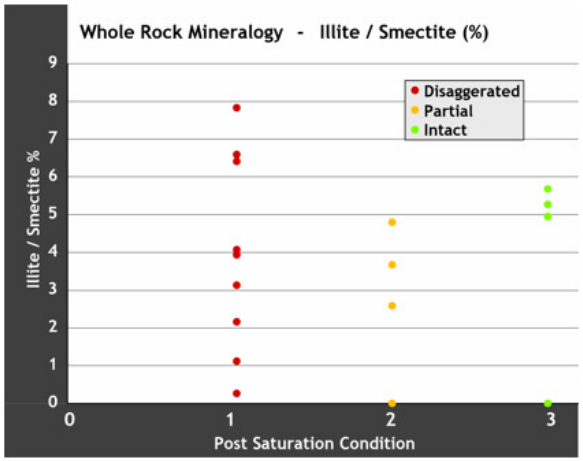

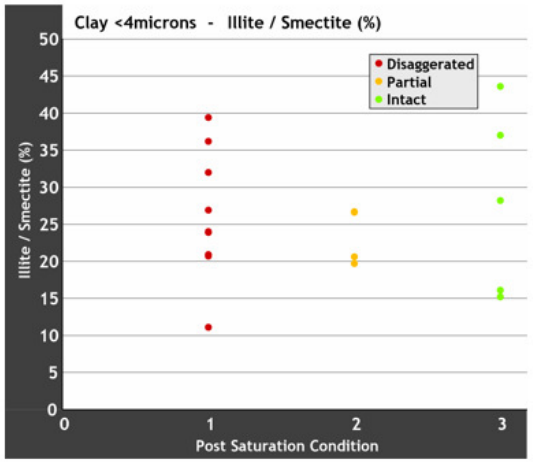

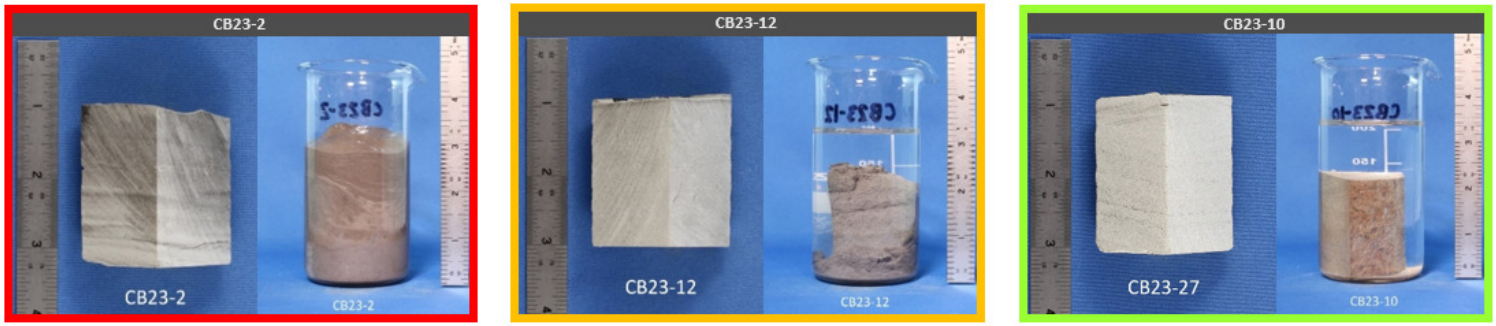

Figure 42: Dissolution analysis (from Chapter 3) plotted with the XRD results from the whole rock mineralogy of the relative clay abundance in bulk sample showing the illite / smectite percentage (top left) and the relative clay abundance (<4 microns) of the illite / smectite percentage (top right). From the plotted results, there is no clear threshold of clay content for sample disaggregation.

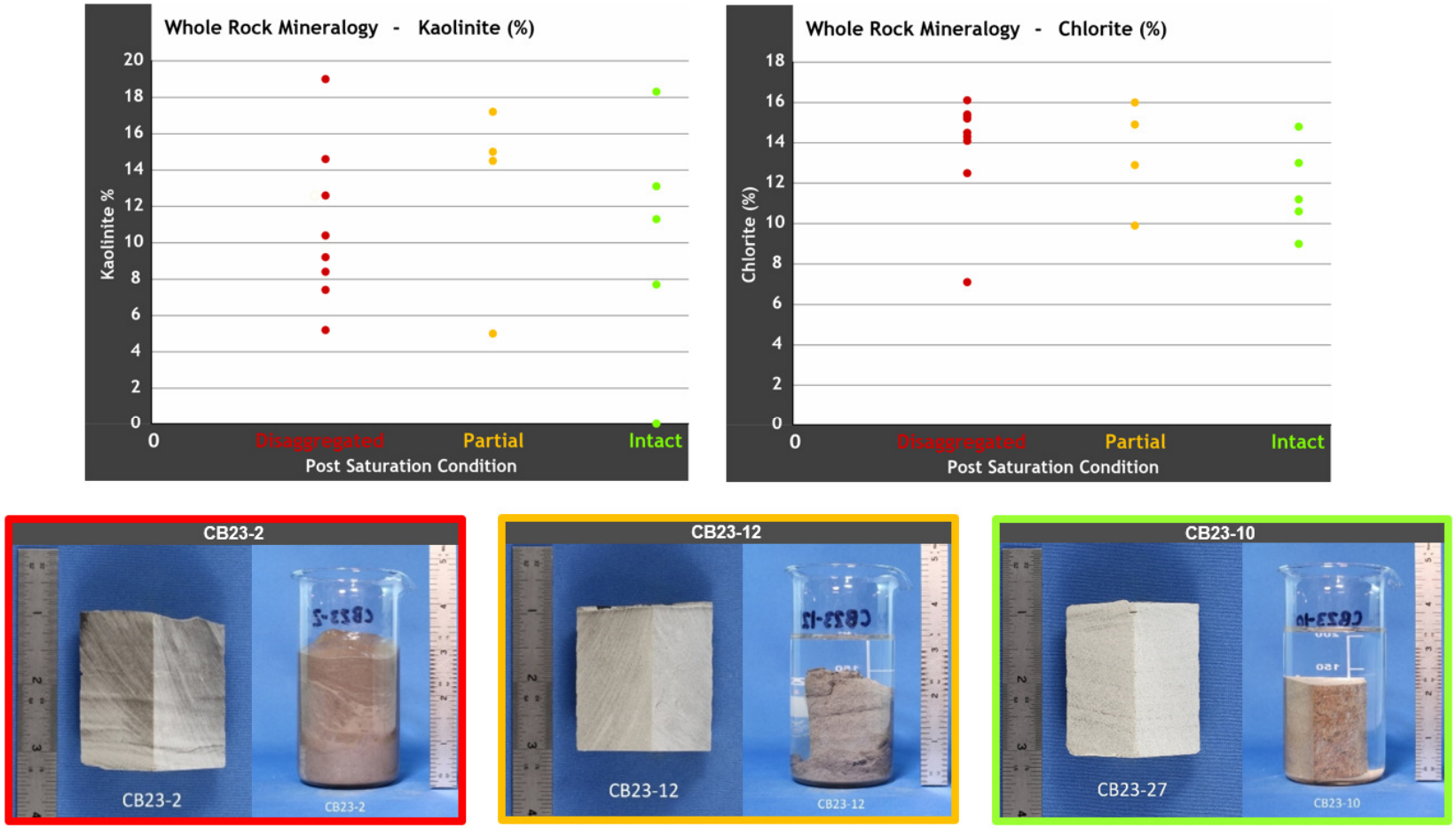

Figure 43: Dissolution analysis (from Chapter 3) plotted with the XRD results from the whole rock mineralogy of the relative clay abundance in bulk sample showing the kaolinite percentage (top left) and the relative clay abundance of the chlorite percentage (top right). From the plotted results, there is no clear threshold of clay content for sample disaggregation.

4.8.1 Results and Discussion

All four of the examined samples showed abundant partially devitrified and clay-altered volcanic rock fragments as texturally immature and submature. The sandstone and siltstone samples were classified as litharenites representing tuffaceous deposits. The sandstone samples are moderately sorted and laminated to rippled. Most samples are consolidated and show evidence for natural compaction and tight grain packing.

The litharenites have displayed poor framework rigidity due the dominant grain type consisting of partially dissolved and altered glassy volcanic rock fragments. Ductile clay-altered rock fragments, detrital mica grains, and partially dissolved microporous grains further decrease framework rigidity. Significant matrix components consist of monocrystalline quartz grains and minor feldspar crystal grains. The quartz grains appear to float and are not cemented together and the feldspar grains are often partially dissolved.

The quartz crystal grains commonly exhibit long to concave-convex contacts with no intergranular porosity as the volcanic grains are tightly packed. Some coarsely crystalline carbonate cements are identified in small quantities and these occlude intergranular pores. Overall, there is no silica cement between quartz framework grains, as the grains are not cemented together by secondary minerals.

Softer detrital components such as the clay-altered volcanic rock fragments, micas, sedimentary rock fragments and both detrital and authigenic clays make up a major portion of each sample. Porosity can be reduced, and compressibility increased, by the occlusion of these components that fill pores and occasionally form thin coatings on grains and line pore throats. With the combination of these components, a ductile pseudomatrix is formed that cushions framework grains from compressive stress.

The subangular quartz crystal grains, from all sandstone samples, are packed between irregularly-shaped and compacted volcanic rock fragments. Stress concentration and grain damage during depletion and reservoir compaction may be possible, because none of the grains are in point contact. In contrast, the grains could possibly absorb stress with their high surface contact areas. However, increased stress could also cause collapse of dissolved and weakened rock fragments.

Authigenic clays, such as kaolinite, smectite, and mixed-layer illite-smectite, partially occlude the rare original intergranular pores represented as the primary pore spaces. The secondary porosity is predominantly identified where glassy fragments have been leached and volcanic lithic fragments have corroded or altered to clay. There are some minor voids left by dissolution of calcite cements and plagioclase grains.

The XRD analysis shows minor potassium feldspar, smectite-rich illite-smectite and smectite as fine devitrified products in a matrix that is composed of microcrystalline quartz. SEM analysis observed that authigenic smectite coats the grains in sandstones, and lines the intergranular pore spaces. The primary intergranular mud appears to have been minimal in the sandstones but argillaceous laminations have abundant detrital and/or authigenic kaolinite. Kaolinite in the matrix occurs in microcrystalline books with stacked crystals, and is coated with webby smectite.

The grain-supported rocks in the Condabri 21 and Condabri 140 wells are not considered typical sandstones. They are dominantly composed of tuffaceous materials with quartz and feldspar grains, representing phenocrysts from volcanic deposition due to the proximity of the Jurassic volcanic arc. Many of the grains were originally composed of volcanic glass and the ash and pumice fragments have devitrified and altered to fine silica and clay. Original grain outlines are difficult to distinguish, and much of the fine matrix may also represent altered tuffaceous material.

Sample CB21-6 (917.90 m) from Condabri 21 is a siltstone gradational into argillaceous mudstone and is composed of 50% clay, according to whole-rock XRD analyses. The deeper selected samples from Condabri 140 (140-36 at 710.15 m and 140-41 at 873.37 m) are matrix supported argillaceous mudstones without significant amounts of silt or sand. Modal analysis was not conducted on these two samples.

It is considered herein that samples with more than 3 - 5% of total expandable clay have a minor sensitivity to fresh water fluids. Samples with 5 – 10% of total expandable clay are considered to have a moderate sensitivity to fresh water fluids. Anything with more than 10% of total expandable clay content is considered to have high to very high sensitivity to fresh water fluids. This definition is broadly used in the petroleum industry and may not be entirely accurate in this area (see later results).

From the dissolution analysis (Chapter 3) plotted with the XRD data (Figure 39, Figure 40, Figure 41, Figure 42, Figure 38), there is no clear threshold of clay content and sample disaggregation. From the plot of the illite / smectite percentage of the whole rock mineralogy, and the illite / smectite percentage from the clay mineralogy (<4 microns), there is no clear threshold behaviour for sample disaggregation.

The scale of each facies is described in metres compared to the resolution of the wireline logs and core analysis that is described in centimetres. This order of magnitude of difference creates complexity when upscaling to correlate for potential prediction of clay percentages within each facies.

The above analyses suggest that clay content (yet not absolute clay percentage) is contributing and potentially controls fines production. The above work suggests that fines occur irrespective of depositional facies. From an oilfield operational point of view the key question is the predictability of fines producing clays from wireline logs. The next chapter presents results of petrophysical analyses based on wireline logs.

Chapter 5 - Petrophysical Analysis

5.1 Introduction

Petrophysical analyses using wireline log data were conducted to analyse rock properties, particularly shale volumes and porosity, to predict reservoir conditions. The key objective of this chapter is to examine whether petrophysical analyses have the capability to predict fines producing lithologies within the WSG.

Many sandstones within the WSG do not display low gamma ray counts because of the volcanic overprint (Scott 2008). Earlier work from Power and Devine (1970) showed the WSG is comprised of less than 20% sandstone in the Surat Basin. The investigations were based on the analysis of electrical and gamma ray data from 166 conventional petroleum wells. Many sandstones were found to display a higher gamma ray count than would be expected for a conventional sandstone signature (Power and Devine, 1970; Scott, 2008).

Yago (1996) conducted a similar investigation for the WSG, but of the 21 wells used in his study, only six wells intersected the entire WSG, and these wells were not cored. Most of the wells reviewed by Yago (1996) contained less than 20% sandstone, which confirms that standard electrical and gamma ray logs do not yield an accurate representation of the sandstone characteristics within the WSG (Scott, 2008).

From the XRD analysis, there is a discrete volume of volcaniclastics evident through the WSG section. These clays may not always be evident, even in thin section analysis. From the previous chapter, it is evident from the SEM that the clays are contained within the sediments of the samples indicated. We are attempting to upscale the information to allow this to be translated in to wireline logs for regional extrapolation.

5.2 Method

The wireline logging suites acquired for Condabri 21 and Condabri 140 for this study consisted of the Schlumberger Platform Express (PEX), which combines gamma ray (GR), two-armed caliper (TAC), spontaneous potential (SP), high resolution density (RHO8), photo-electric (PE), neutron porosity (NPHI) and resistivity (RES). The Schlumberger elemental captured spectroscopy (ECS) log was also run to measure primary elements of silicon (Si), iron (Fe), calcium (Ca), sulphur (S), titanium (Ti), Gadolinium (Gd), chlorine (Cl), barium (Ba) and hydrogen (H).

The focus of this study is to characterise the clays for potential fines production from the interburden clastics, not the coals. A petrophysical analysis was run on each well as part of the initial open-hole evaluation. To exclude the coals, a coal flag was determined from the high-resolution density log, where sequences are flagged as coals, and subsequently excluded, if they have densities of ≤1.75 g/cc.

To focus on the fines producing clastics, the analysis was undertaken in two parts, namely:

- determination of shale volume using different techniques, and;
- use of ECS logs for comparison to XRD data.

5.3 Shale Volume

The volume of shale can be defined as the bulk volume of the rock composed of clay minerals and clay bound water (Crain 2002). The gamma ray log is typically used to calculate shale but the shale volume can be calculated in a number of ways. For this study, four methods have been employed and yielded varying results. The volume of shale (v-shale) calculation was run in Geolog using four different methods.

1. Gamma ray.
2. Density-neutron.
3. Density-sonic.
4. An average from gamma ray and density-sonic methods.

5.3.1 V-Shale from GR

Parameters

	Location	Mode	Comment	Unit	Name	Value
1	Constant	In_Out	Option for VSH from gamma ray	ALPHA*8	OPT_GR	LINEAR
2	Constant	In_Out	Gamma ray matrix (clean)	GAPI	GR_MA	45
3	Constant	In_Out	Gamma ray shale	GAPI	GR_SH	94
4	Constant	In_Out	Option to allow coal logic	LOGICAL	OPT_COAL	Yes
5	Log	Input	Gamma ray log	GAPI	GR	GR_NORM
6	Log	Input	Coal flag	LOGICAL	COAL	TRAFFIC_LIGHTS.COAL
7	Log	Output	VSH from gamma ray	V/V	VSH_GR	VSH_GR
8	Log	Output	Limited volume of shale	V/V	VSH	VSH

Figure 44: The input parameters for the calculated V-shale from gamma ray.

The shale matrix value used was 94 API and the clean matrix (sand) was 45 API. The GR V-shale method uses the following linear equation:

VSH_GR = (GR - GR_MA) / (GR_SH - GR_MA)

The GR_SH and GR_MA are the (100%) shale and clean (0% shale) matrix gamma ray values respectively. If coal is flagged, both VSH_GR and VSH are set to zero. The GR is a robust log and shows very little negative effects from bad hole conditions.

5.3.2 V-Shale from Density-Neutron

The method for calculating VSH_DN is the solution of the following equations for VSH:

RHO = RHO_MA*(1-VSH-PHIE) + RHO_FL*PHIE + RHO_SH*VSH
NPHI = NPHI_MA*(1-VSH-PHIE) + NPHI_FL*PHIE + NPHI_SH*VSH

A spuriously low VSH can result if this method is applied in bad hole conditions. Hydrocarbons may affect these logs, and thus it is important to place zones in wells by lithology and fluid type. If coal is flagged, both VSH_DN and VSH are set to zero.

5.3.3 V-Shale from Density-Sonic

Parameters

	Location	Mode	Comment	Unit	Name	Value
1	Constant	In_Out	Matrix density	G/C3	RHO_MA	2.645
2	Constant	In_Out	Shale density	G/C3	RHO_SH	2.71
3	Constant	In_Out	Fluid density	G/C3	RHO_FL	1
4	Constant	In_Out	Matrix transit time	US/F	DT_MA	50.6291
5	Constant	In_Out	Shale transit time	US/F	DT_SH	100.945
6	Constant	In_Out	Fluid transit time	US/F	DT_FL	188.976
7	Constant	In_Out	Option to allow bad hole logic	LOGICAL	OPT_BH	No
8	Constant	In_Out	Option to allow coal logic	LOGICAL	OPT_COAL	No
9	Log	Input	Density log	G/C3	RHO	HDEN
10	Log	Input	Sonic log	US/F	DT	DTCO
11	Log	Output	VSH from density-sonic	V/V	VSH_DS	VSH_DS
12	Log	Output	Limited volume of shale	V/V	VSH	VSH

Figure 45: The input parameters for the calculated V-shale from density and sonic logs.

The method for calculating VSH_DS is the solution of the following equations for VSH:

RHO = RHO_MA*(1-VSH-PHIE) + RHO_FL*PHIE + RHO_SH*VSH
DT = DT_MA*(1-VSH-PHIE) + DT_FL*PHIE + DT_SH*VSH

The calculation will be affected by bad hole conditions, which will result in a spuriously low VSH. This calculation is less dependent on lithology and fluid

conditions than density-neutron, but it is still advisable to zone by lithology and fluid type. The calculation is poor in highly under compacted formations (e.g. if shallow or overpressured). If the coal is flagged, both VSH_DS and VSH are set to zero.

5.3.4 V-Shale from Average of Gamma Ray and Density-Sonic Methods

The method for calculating VSH_AVG is the solution of the following equations for VSH:

VSH_AVG = (VSH_GR + VSH_DN) / 2

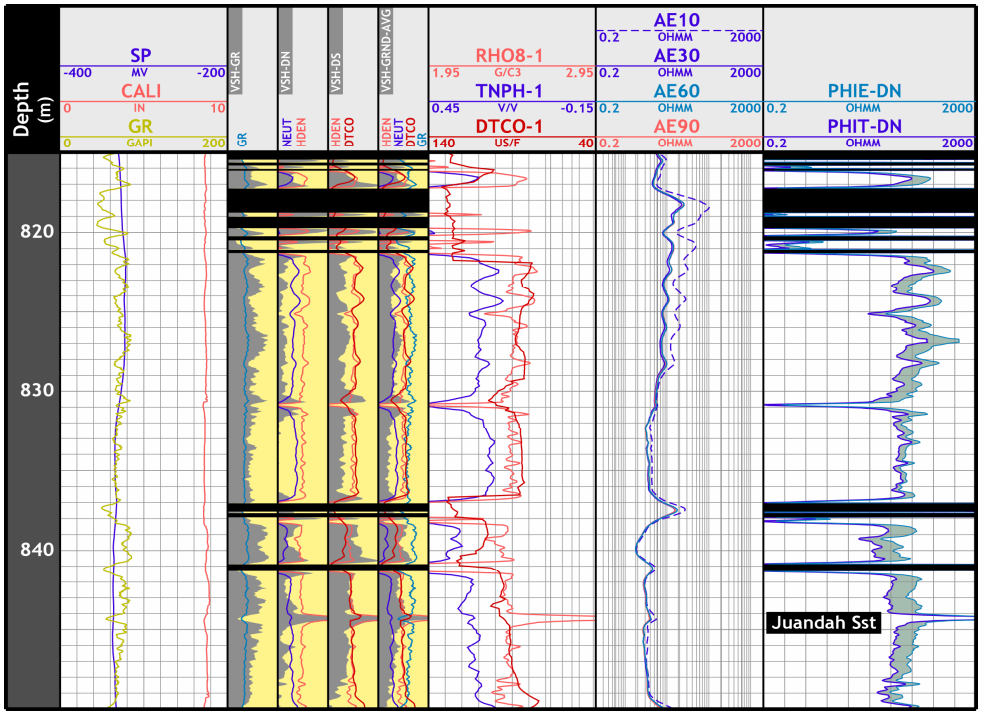

Figure 46: Wireline plot showing calculated V-shale from (left to right) gamma ray, density / neutron, gamma ray and neutron / density average and the density sonic. The respective logs are overlain within each track to show correlations of the calculated v-shale and the logs used. The third v-shale track is the arithmetically calculated average of GR and DS.

5.4 ECS Log Analysis

The Schlumberger elemental captured spectroscopy (ECS) log measures the primary elements of silicon (Si), iron (Fe), calcium (Ca), sulphur (S), titanium (Ti), Gadolinium (Gd), chlorine (Cl), barium (Ba) and hydrogen (H). The ECS tool uses a set of elemental standards to produce relative elemental yields. The relative yields are then converted to dry-weight elemental concentration logs using an oxides closure method. The Schlumberger ECS uses a core chemistry and mineralogical database to calculate matrix properties and quantitative dry-weight lithologies derived from the SpectroLith lithology process.

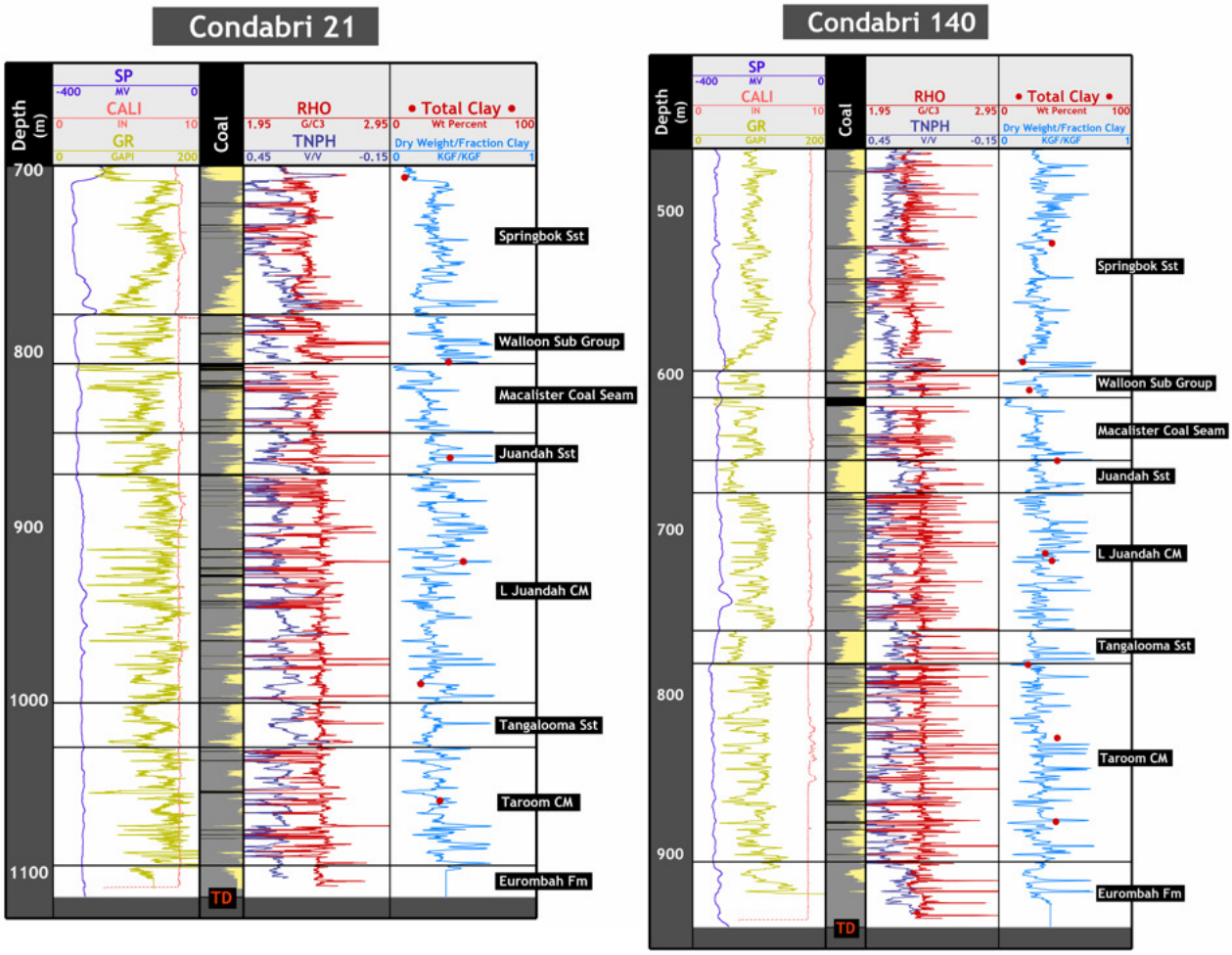

Figure 47: The ECS log estimate of total clay (in weight %) from Condabri 21 (left) and Condabri 140 (right) yields a good match with the XRD analysis data of the total clay (in weight %; red dots).

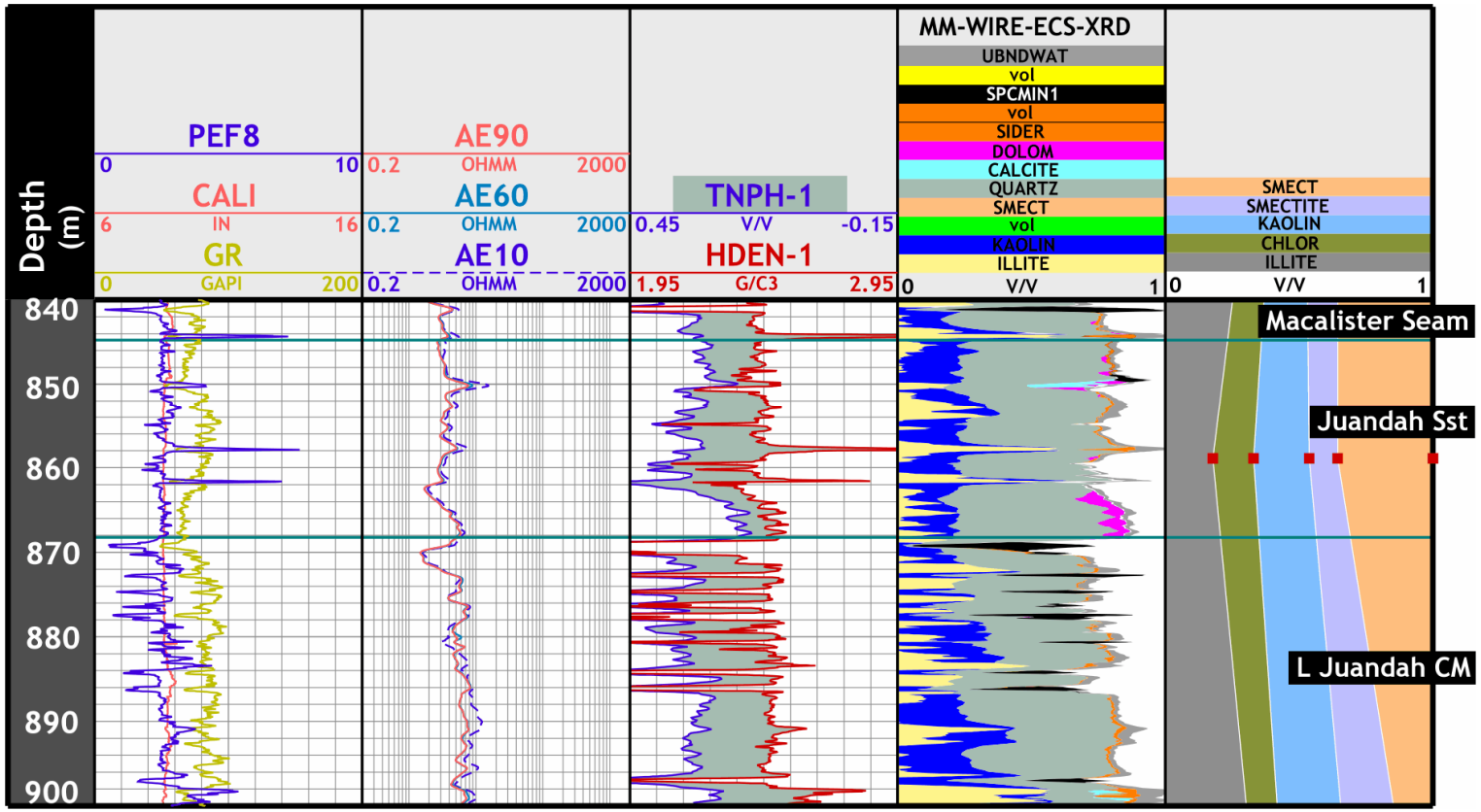

Figure 48: Condabri 21 showing the ECS log in the track, second from right. The far right hand track shows the XRD data (red dots), which indicates 10% smectite. The ECS log shows 0% smectite.

5.5 Results and Discussion

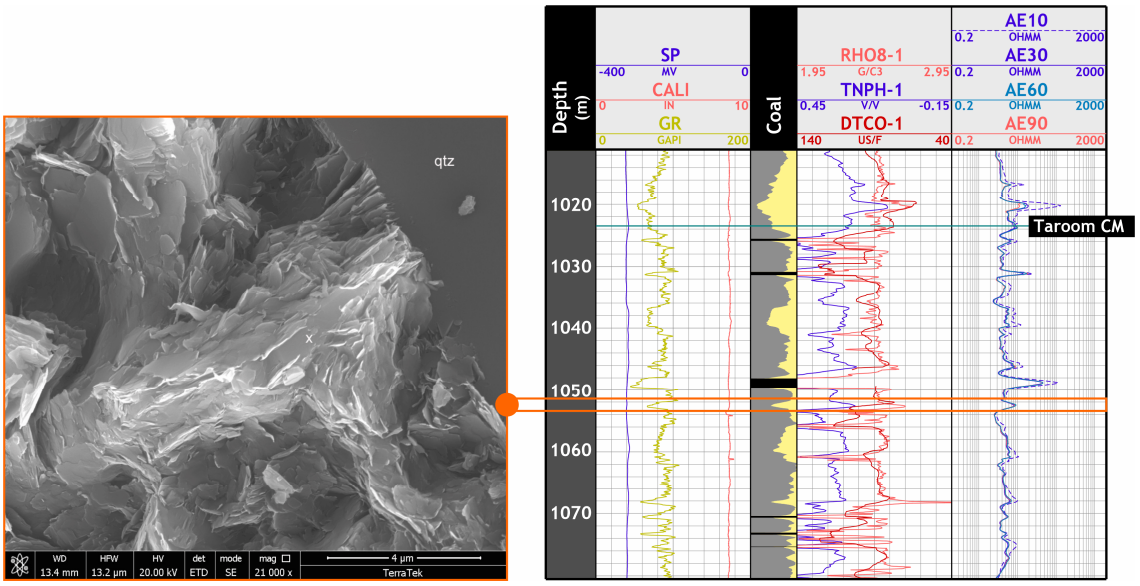

Figure 49: The SEM image (left) shows a litharenite sandstone with flaky to platy clays in the matrix that are squeezed between quartz and other grains (scale bar = 4 microns). The wireline plot (right) shows the interval in red where the SEM sample is from. Although this sample is classed as a sandstone, it is displaying a high GR value (115 – 125 API).

From the four methods used to calculate v-shale, the results were noticeably varied. At a depth interval of 958 – 960 mRT, the v-shale ranged from 4% (density-neutron) to 100% (density-sonic). The density-neutron method calculated a value of 4% and the averaged density-neutron was 7%.

The XRD data shows a much higher percentage of smectite (61%) than is estimated from the ECS log, which shows 0% smectite (Figure 43). This could be attributed to the scale of clay analysis (<4 microns for discrete smectite), whilst the resolution of the ECS log is approximately 6”. The sample resolution compared to the volume measured is shown in Chapter 2 (Figure 23).

Furthermore, the ECS logging tool is designed to measure and characterise 5 distinct elements. The discrete volumes of clays can be misinterpreted due the volcanic overprint within the WSG. The fine fraction of dispersed clays do not have a distinct log signature, or a distinct facies or zone, and these clays are not always obvious in core.

In conclusion, whilst it is understood, from earlier analyses, which lithological compositions (i.e. clay content) are contributing to fines production, these key lithologies could not be reliably predicted by either facies or petrophysical analyses.

Chapter 6 - Rock Strength Testing

6.1 Introduction

This chapter examines the potential contribution of rock strength to fines production. The tests are designed to simulate wellbore conditions to understand if rock strength is an isolated parameter which could potentially contribute to solids production.

In formations of variable strength, the likelihood of fines production in an uncased well can be a function of depletion, drawdown, production rates and bottom hole flowing pressure. In weak formations, reducing production rates can limit fines production prior to significant depletion (Zoback 2007).

Direct measurements of static mechanical parameters and rock strength are only possible by obtaining core samples (Fjaer et al. 2008). As part of the geomechanical analysis, the following four rock strength testing methods were conducted using samples from two wells within the study area:

1. Unconfined Compression Strength (UCS) testing.
2. Triaxial compression testing (single stage and multi-stage).
3. Brazilian (indirect) tensile strength hardness testing.
4. Brinell hardness fluid sensitivity testing.

6.2 Unconfined Compressive Strength Testing (UCS) – Original Samples and Brine Saturated Samples

6.2.1 Method

Unconfined compressive strength (UCS) testing is conducted to determine peak compressive strength from shear failure when loaded under uniaxial compression with no radial stress (Zoback 2007). UCS tests were performed on twelve samples from Condabri 21 and twenty samples from Condabri 140. All samples were vertical plugs taken with the plug axis parallel to the core axis which is perpendicular to bedding. All UCS tests were performed at room temperature with pore pressure drained to the atmosphere. Samples were tested in their original condition. All tests were completed using a standard loading axial strain rate (1 x 10-5 in/in/s).

From the results of Chapter 3 (Dissolution Analysis), the impact of fluid interaction with rock was investigated further in the UCS testing. Competent sister plug samples were taken, with one sample tested in the air-dry (or original) state, and the adjacent sister sample tested following cool oven drying at 50°C (to determine dry mass), then vacuum saturated in synthetic formation water with soaking for a minimum of five days. The samples were saturated in 200 ml of brine with an ionic composition similar to that of the formation water, based on an analysis from the offset well Condabri 16 (Table 1). The total dissolved solids of the synthetic brine were approximately 3600 mg / litre. In some cases, samples were observed to disaggregate during saturation and were not suitable for UCS testing.

6.2.2 Results of Unconfined Compressive Strength Testing (UCS) – Original Samples and Brine Saturated Samples

From the total of 16 samples (six samples from Condabri 21 and ten samples from Condabri 140) exposed to the brine saturation, a total of eight samples disaggregated. A summary of UCS results from Condabri 21 and Condabri 140, including static mechanical properties are presented below (Table 8 and Table 9).

Six samples were tested from Condabri 21, two of which disaggregated during the saturation period. The average UCS for the six original samples was 8,718 psi, and ranged from 5,130 to 14,460 psi. The Young's modulus (YM) averaged 1,740,083 psi and the Poisson's ratio (PR) averaged 0.22.

For the four brine saturated samples that remained intact from Condabri 21, the average UCS was 5,417 psi, and ranged from 1,200 to 10,785 psi. The average Young's modulus was 1,438,100 psi and the average Poisson's ratio was 0.31.

Ten samples were tested from Condabri 140, six of which disaggregated during the saturation period. The average UCS for the ten original samples was 8343 psi ranging from 4240 to 18,510 psi. The Young's modulus averaged 1,688,400 psi and Poisson's ratio averaged 0.23.

For the four brine saturated samples that remained intact for Condabri 140, the average UCS was 7,408 psi ranging from 2,675 to 14,325 psi. The average Young's Modulus was 2,257,775 psi and the average Poisson's Ratio was 0.30.

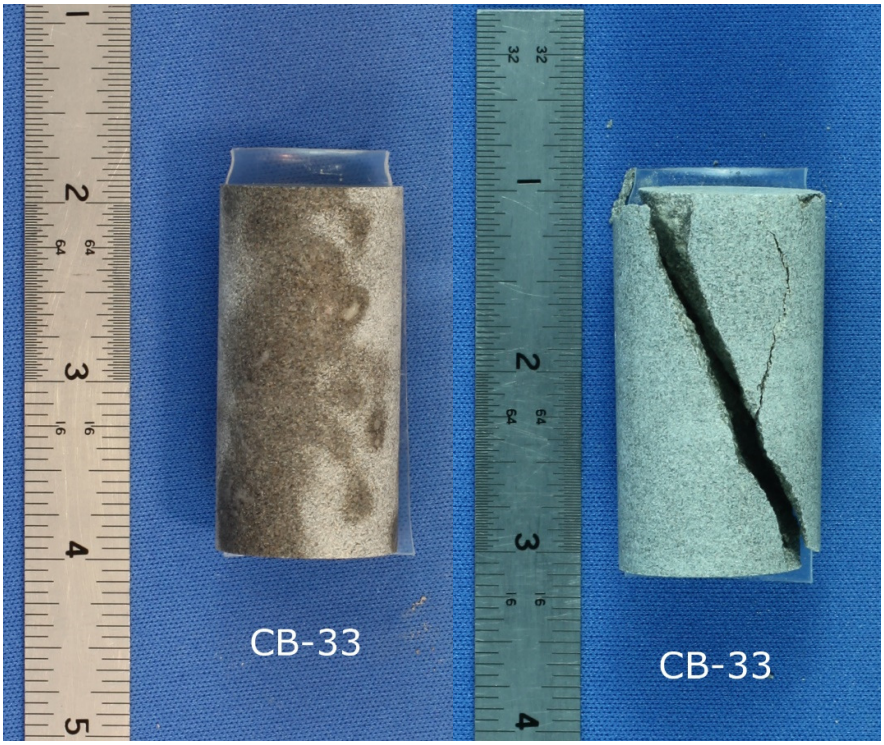

Figure 50: The post saturation sample CB-33 (left) and post saturation sample after UCS test (right). The sample was taken from a depth of 1053.88 m in Condabri 21. The original sample UCS value was 14,460 psi whilst the brine saturated sample had a UCS of 10, 875 psi.

Table 8: A summary of UCS results conducted on six original samples and six brine saturated samples for Condabri 21.

Well	Sample ID	Depth (m)	Original Samples Bulk Density (g/cm^3)	Orientation	Saturation	Effective Confining Pressure (psi)	Effective Compressive Strength (psi)	Static Young's Modulus (psi)	Static Poisson's Ratio
Condabri 21	CB-22	699.54	2.392	Vertical	Original	0	8,910	3,194,800	0.23
	CB-23	699.54	2.457	Vertical	Brine Saturated	0	7,160	2,688,000	0.27
	CB-24	804.45	2.496	Vertical	Original	0	10,615	1,098,000	0.18
	CB-25	804.45	2.490	Vertical	Brine Saturated	0	2,435	195,100	0.42
	CB-26	858.90	2.447	Vertical	Original	0	6,295	867,200	0.19
	CB-27	858.90	N / A	Vertical	Brine Saturated	Sample disaggregated during saturation			
	CB-28	917.90	2.376	Vertical	Original	0	6,895	1,044,300	0.22
	CB-29	917.90	2.406	Vertical	Brine Saturated	0	1,200	114,500	0.29
	CB-30	987.47	2.363	Vertical	Original	0	5,130	1,127,300	0.27
	CB-31	987.47	N / A	Vertical	Brine Saturated	Sample disaggregated during saturation			
	CB-32	1053.88	2.592	Vertical	Original	0	14,460	3,108,900	0.20
	CB-33	1053.88	2.616	Vertical	Brine Saturated	0	10,875	2,754,800	0.26

Table 9: A summary of UCS tests conducted on Condabri 140 consisting of ten brine saturated samples and ten original samples.

Well	Sample ID	Depth (m)	Original Sample Bulk Density (g/cm^3)	Orientation	Saturation	Effective Confining Pressure (psi)	Effective Compressive Strength (psi)	Static Young's Modulus (psi)	Static Poisson's Ratio
Condabri 140	CB-20	511.43	2.226	Vertical	Original	0	4,240	998,200	0.23
	CB-21	511.43	N / A	Vertical	Brine Saturated	Sample disaggregated during saturation			
	CB-18	585.48	2.563	Vertical	Original	0	17,315	4,723,100	0.22
	CB-19	585.48	2.577	Vertical	Brine Saturated	0	14,325	4,449,700	0.28
	CB-16	603.23	2.638	Vertical	Original	0	18,510	4,517,200	0.20
	CB-17	603.23	2.616	Vertical	Brine Saturated	0	8,925	3,493,000	0.38
	CB-14*	647.22	1.662	Vertical	Original	0	5,105	389,000	0.31
	CB-15*	647.22	1.670	Vertical	Brine Saturated	0	2,675	104,700	0.15
	CB-12	705.40	2.473	Vertical	Original	0	6,055	1,052,400	0.21
	CB-13	705.40	N / A	Vertical	Brine Saturated	Sample disaggregated during saturation			
	CB-10	709.78	2.381	Vertical	Original	0	5,860	730,500	0.18
	CB-11	710.03	N / A	Vertical	Brine Saturated	Sample disaggregated during saturation			
	CB-8	775.09	2.357	Vertical	Original	0	5,910	1,272,300	0.25
	CB-9	775.09	N / A	Vertical	Brine Saturated	Sample disaggregated during saturation			
	CB-6	820.93	2.438	Vertical	Original	0	7,080	1,002,100	0.16
	CB-7	820.93	N / A	Vertical	Brine Saturated	Sample disaggregated during saturation			
	CB-3	873.30	2.487	Vertical	Original	0	7,695	898,000	0.13
	CB-4	873.30	N / A	Vertical	Brine Saturated	Sample disaggregated during saturation			
	CB-1	917.50	2.243	Vertical	Original	0	5,660	1,301,200	0.31
	CB-2	917.50	2.390	Vertical	Brine Saturated	0	3,710	983,700	0.37

*These samples are carbonaceous shales adjacent to coals

Table 10: A summary of the XRD analysis from Chapter 4 with the post saturation sample condition.

Well	Sample ID	Depth	Sample Mass Dry (g)	Lithology	Post Saturation Sample Condition	Total Clay (%)	TEC – Total Expandable Clay (%)
Condabri 21	CB-23	699.54	56.27	sandstone	competent	10	0
	CB-25	804.45	58.70	siltstone	competent	40	10
	CB-27	858.90	61.26	siltstone	disaggregated, partial	41	13
	CB-29	917.90	25.29	siltstone	competent	50	10
	CB-31	987.47	62.30	sandstone	disaggregated, total	21	0
	CB-33	1053.88	66.26	sandstone	competent	34	1
Condabri 140	CB-21	511.43	55.92	sandstone	disaggregated, total	40	7
	CB-19	585.50	65.64	sandstone	competent	18	2
	CB-17	603.23	66.90	sandstone	competent	23	0
	CB-15	647.22	16.53	carbonaceous shale	competent	44	11
	CB-13	705.40	52.61	siltstone	disaggregated, partial	35	2
	CB-11	710.03	25.56	mudstone	disaggregated, partial	40	4
	CB-9	775.09	60.60	sandstone	disaggregated, partial	22	0
	CB-7	820.93	53.11	siltstone	disaggregated, partial	44	6
	CB-4	873.30	57.52	mudstone	disaggregated, partial	43	4
	CB-2	917.50	58.49	sandstone	competent	No XRD	No XRD

6.2.3 Brine Analysis following Saturation of UCS Samples

Following the saturation period, the brine in contact with the rock samples from both wells was analysed and showed low levels of several compounds. This indicates that measurable dissolution was taking place from both competent and disaggregated rock samples while in contact with the brine. In particular, totally disaggregated sandstone sample CB-21 (depth 511.43 from well Condabri 140) had higher than normal aluminium (27mg/l) and silicon (76mg/l) concentrations. This is possibly from suspended kaolinite from the disassociated rock.

6.2.4 Discussion Brine Analysis following Saturation of UCS Samples

From the 16 samples exposed to the brine saturation, a total of eight samples disaggregated. The total clay content from the whole rock mineralogy of the disaggregated samples ranged from 10 - 50%. The total expandable clay, determined from the relative clay abundance in bulk sample, ranged from 0 – 13%. The reduction in YM ranged from 6% to 100% (sample disaggregation). The PR ranged from 100% reduction (sample disaggregated) to 133% increase.

One of the four samples that disaggregated from Condabri 21 (siltstone sample CB-27, depth 858.90m) exhibited partial disaggregation and contains total clay of 41% and total expandable clay of 13% from whole rock XRD analysis. Sandstone sample CB-31 (987.47m) exhibited total disaggregation during saturation. From whole rock XRD analysis this sample had total clay of 21% and total expandable clay of 0%. There was an outlier in sample CB-29, which contained 50% total clay content but remained competent after brine saturation. Although the brine saturation reduced the UCS by 83% (original UCS 6,895 psi, brine saturated UCS 1,200 psi), Young's modulus by 89% (original YM 1,044,300 psi, brine saturated YM 114,500 psi) and PR increased by 131% (original PR 0.22, brine saturated PR 0.29).

From the six disaggregated samples from Condabri 140, sandstone sample CB-21 (511.43m) disaggregated totally. From whole rock XRD analysis this sample had total clay of 40% and total expandable clay of 7%. The remaining five samples, which partially disaggregated, were from the deeper depths of 705.40m to 873.30m, and included sandstone, siltstone and mudstone. From whole rock XRD analyses, these samples showed total clay ranging from 22% to 44% and total expandable clay ranging from 0% to 6%.

From the 16 samples from two wells analysed for the brine saturation UCS analysis the following observations were made:

1. Samples with a UCS greater than 8000psi did not disaggregate entirely
2. All samples tested shows signed of water weakening (some only minor), irrespective of expandable clay content.

6.3 Multi-Stage Triaxial Testing – Original Samples and Brine Saturated Samples

6.3.1 Method

Triaxial compression tests ($S_1 > S_2 = S_3 = S_0$) are the most common way of measuring rock strength under conditions which replicate those at depth (Zoback 2007). Multi-stage triaxial compression tests were conducted with concurrent ultrasonic velocity measurements on original vertical samples at room temperature for Mohr-Coulomb failure envelope delineation.

Multi stage testing was chosen where there were insufficient identical samples for single stage testing. Multi stage tests are afflicted with some uncertainty as the same sample is tested repeatedly. Notably peak strength of rocks is somewhat compromised due to repeat testing of one sample. Fractures that develop during testing can affect the results, in particular the late stages of multi-stage testing.

Multi-stage triaxial compression tests were performed on vertical samples from selected depth intervals from Condabri 21 and Condabri 140 at varying confining pressures, in order to construct Mohr stress circles and calculate Coulomb parameters of cohesion and tensile strength. Initially, two triaxial compression tests from Condabri 21 were performed at room temperature with samples tested as received in their effective room dry condition, using a standard loading axial strain rate of 1 x 10-5 in/in/s.

It was subsequently decided to rerun all drained tests in the saturated condition with an elevated pore pressure of 200psi, to ensure saturation during loading. Samples were evacuated then back saturated in a vessel. The fluid was an ionic composition similar to the produced fluid from Condabri 16. The synthetic brine contained approximately 3600 mg / litre of total dissolved solids (Table 1). Sandstone samples were tested with an axial loading strain rate of 1x10-5 in/in/s and mudstone samples were tested with an axial loading strain rate of 2x10-6 in/in/s.

6.3.2 Results of Multi-Stage Triaxial Testing – Original Samples and Brine Saturated Samples

A summary of triaxial compression test results, including static mechanical properties, is presented in Table 11 and Table 12. Coulomb criteria for the evaluated sandstone intervals are summarised in Table 13. Comparisons of static and dynamic values of Poisson's ratio and Young's modulus with increasing confining pressure for vertical plugs from sandstone samples are shown for well Condabri 21 in Table 11. Comparisons for Condabri 140 are shown in Table 12.

Following the water weakening observed from the saturated UCS testing, it was decided to repeat all tests using brine saturation, drained conditions and elevated pore pressure. No significant differences in strength or elastic properties were observed between the dry and saturated samples under confined conditions. In all samples, post-failure behaviour on the final stage (i.e., following peak load) was

typically characterised by a slight to moderate drop in stress, followed by strain softening to a residual stress condition.

Table 11: A summary of Multi-Stage Triaxial Compression tests from Condabri 21 of the brine saturated and original samples tested.

Well	Sample ID	Depth (m)	Original Samples Bulk Density (g/cm^3)	Lithology	Saturation	Orientation	Effective Confining Pressures (psi)	Effective Compressive Strength (psi)	Residual Effective Compressive Strength (psi)	Static Young's Modulus (psi)	Static Poisson's Ratio
Condabri 21	CB21-10	699.61	2.416	Sandstone	Original	Vertical	650	11,680	--	4,538,900	0.27
							1300	14,580	--	4,984,900	0.41
							1950	17,375	7460	4,840,200	0.44
	CB21-11	699.61	2.423	Sandstone	Brine Saturated	Vertical	650	12,665	--	3,533,000	0.23
							1300	16,140	--	4,569,000	0.36
							1950	19,695	9250	4,508,000	0.44
	CB21-21	917.83	2.382	Mudstone	Original	Vertical	855	7285	--	960,200	0.20
							1705	9370	--	1,155,500	0.28
							2560	11,310	8040	1,238,800	0.30
	CB21-22	917.83	2.427	Mudstone	Brine Saturated	Vertical	855	7100	--	844,100	0.19
							1705	9585	--	1,265,000	0.23
							2560	11,980	8810	1,264,000	0.25
	CB21-26	1053.88	2.595	Sandstone	Brine Saturated	Vertical	980	15,455	--	2,895,000	0.18
							1960	18,295	--	3,464,000	0.24
							2940	22,030	11,640	3,476,000	0.26

Table 12: Summary of Multi-Stage Triaxial Compression Tests from Condabri 140 of the brine saturated and original samples tested.

Well	Sample ID	Depth (m)	Original Samples Bulk Density (g/cm^3)	Lithology	Saturation	Orientation	Effective Confining Pressures (psi)	Effective Compressive Strength (psi)	Residual Effective Compressive Strength (psi)	Static Young's Modulus (psi)	Static Poisson's Ratio
Condabri 140	CB140-3	585.48	2.557	Sandstone	Brine Saturated	Vertical	545	18,910	--	4,345,000	0.22
							1090	21,935	--	4,869,000	0.28
							1635	25,985	9885	4,767,000	0.30
	CB140-14	709.95	2.367	Mudstone	Brine Saturated	Vertical	660	6705	--	674,500	0.12
							1320	8475	--	1,058,000	0.17
							1980	10,725	8920	1,003,000	0.19
	CB140-25	917.50	2.243	Sandstone	Brine Saturated	Vertical	655	7285	--	1,413,000	0.20
							1505	9795	--	1,770,000	0.24
							2360	12,005	10,690	1,703,000	0.25
	CB140-26	917.50	2.256	Sandstone	Brine Saturated	Vertical	855	8995	--	1,821,000	0.18
							1705	10,635	--	1,909,000	0.19
							2560	12,380	11,925	1,907,000	0.18

Table 13: Mohr Coulomb Failure Parameters - Multi-Stage Triaxial Compression Tests from Condabri 21 and Condabri 140.

Well	Sample ID	Depth (m)	Lithology	Saturation	Stress Regime	Effective Confining Pressures (psi)			C' (psi)	Φ' (°)	Equation
Condabri 21	CB21-10	699.61	Sandstone	Original	Entire	650	1300	1950	2131	38.8	T' = 0.804σ' +2131
	CB21-11	699.61	Sandstone	Brine Saturated	Entire	650	1300	1950	1965	43.5	T' = 0.948σ' + 1965
	CB21-21	917.83	Mudstone	Original	Entire	855	1705	2560	1722	23.9	T' = 0.443σ' + 1722
	CB21-22	917.83	Mudstone	Brine Saturated	Entire	855	1705	2560	1380	28.8	T' = 0.550σ' + 1380
	CB21-26	1053.88	Sandstone	Brine Saturated	Entire	980	1960	2940	3265	32.8	T' = 0.646σ' + 3265
Condabri 140	CB140-3	585.48	Sandstone	Brine Saturated	Entire	545	1090	1635	2965	47.3	T' = 1.082σ' + 2965
	CB140-14	709.65	Mudstone	Brine Saturated	Entire	660	1320	1980	1315	30.5	T' = 0.588σ' + 1315
	CB140-25	917.50	Sandstone	Brine Saturated	Entire	655	1505	2360	1660	28.0	T' = 0.532σ' + 1660
	CB140-26	917.50	Sandstone	Brine Saturated	Entire	855	1705	2560	2585	19.3	T' = 0.350σ' + 2585

6.3.3 Discussion Multi-Stage Triaxial Testing – Original Samples and Brine Saturated Samples

The average effective compressive strength for Condabri 21 at in-situ stress conditions was 13,594 psi, and for Condabri 140 was 12,710 psi. Average static values from the Condabri 21 samples for YM and PR, determined at in-situ stress conditions, were 3,087,680 psi and 0.30 respectively. In comparison, Condabri 140 showed slightly lower average static values for YM and PR, determined at in-situ stress conditions, of 2,401,500 psi and 0.22 respectively.

A marked difference exists between static and dynamic values for YM and PR from the multi-stage triaxial compression tests. Dynamic values from Condabri 21 samples for YM were approximately 1.2 to 3.7 times higher than corresponding static values, while Condabri 140 showed predominately lower dynamic values for Poisson's ratio that were approximately 0.5 to 1.2 times corresponding static values. Samples from Condabri 140 showed a similar variation for the dynamic and static values for YM and PR. Dynamic values for YM were approximately 1.7 to 3.7 times higher than corresponding static values, while dynamic values for PR were approximately 0.7 to 1.5 times corresponding static values.

Mohr stress circles were used to construct Coulomb failure envelopes for the entire stress range applied. The linear cohesion, determined for the entire stress range applied for Condabri 21 samples, averaged 2093 psi and the friction angle averaged 33.6°. Condabri 140 samples exhibited only slightly different coulomb failure criteria, linear cohesion for the entire stress range averaging 2131 psi and 31.3°.

A summary of triaxial compression test results and coulomb failure criteria, including quasi-static mechanical properties, for the evaluated sandstone interval are summarised in Table 13.

6.4 Brinell Testing for Fluid Sensitivity – Original Samples and Brine Saturated Samples

The Brinell hardness test is an indentation test, which is determined from the ratio of the applied load to the indentation depth. The analysis was conducted on six samples from Condabri 21 and nine samples from Condabri 140 (Table 14). Samples were prepared parallel to bedding, to simulate the fabric of the rock surface exposed to proppant during hydraulic fracturing. Four measurements were obtained at each location, to evaluate consistency and statistical spread.

In addition to hardness measurements, rock heterogeneity along the length of the core samples was assessed via high-resolution, continuous strength measurements (scratch testing) along a typical sample length of approximately 50 mm.

The local strength variability along each sample, and within samples, is indicative of the corresponding variability of surface hardness. This inherent variability in strength and hardness along the sample length should be understood for adequate interpretation of rock-fluid effects during Brinell hardness measurements.

Table 14: Brine saturated fluid sensitivity Brinell Hardness testing matrix.

Serial	Sample ID	Sample Orientation	Depth (m RT)	Test Type
1	CB21-13	Horizontal	699.69	Brinell Hardness
2	CB21-15	Horizontal	804.39	Brinell Hardness
3	CB21-17	Horizontal	859.03	Brinell Hardness
4	CB21-19	Horizontal	917.97	Brinell Hardness
5	CB21-24	Horizontal	987.50	Brinell Hardness
6	CB21-28	Horizontal	1053.86	Brinell Hardness
7	CB140-1	Horizontal	511.50	Brinell Hardness
8	CB140-6	Horizontal	585.59	Brinell Hardness
9	CB140-8	Horizontal	603.31	Brinell Hardness
10	CB140-12	Horizontal	705.27	Brinell Hardness
11	CB140-17	Horizontal	709.99	Brinell Hardness
12	CB140-19	Horizontal	775.16	Brinell Hardness
13	CB140-21	Horizontal	820.80	Brinell Hardness
14	CB140-24	Horizontal	873.37	Brinell Hardness
15	CB140-27	Horizontal	917.42	Brinell Hardness

6.4.1 Method

Brinell hardness fluid sensitivity testing was conducted on each dry sample (original state) and in contact with synthetic brine in order to evaluate the change in both hardness and rock strength over the duration of fluid exposure.

Brinell hardness was measured using a hemispherical indenter of 3.175mm (1/8 in) diameter, and defined by the slope (s) of the load-displacement plot during indentation as follows:

$$BHN = \frac{s}{\pi\left(D - h_c\right)}$$

Equation 1: Brinell Hardness defined by the slope of the load-displacement plot during indentation.

Where D is the diameter of the indenter (mm), h_c is the depth of indentation (mm), and s is the slope (N/mm). Four measurements were obtained at each location, to evaluate median consistency.

Strength measurements were performed using TSI™ scratch testing. TSI™ is a patented scratch test system for continuous measurements of strength by cutting

(scratching) the rock surface. The methodology evaluates the normal and tangential forces required to scratch the rock surface at a constant depth of cut. From these measurements, the intrinsic specific energy and the unconfined compressive strength are calculated.

Fifteen samples from the various examined zones of the Condabri 21 and 140 wells were selected for Brinell hardness fluid sensitivity testing. Each sample was tested dry (i.e., in its original state) and in contact with synthetic brine in order to evaluate the change in both hardness and rock strength over the duration of fluid exposure. The total dissolved solids of the synthetic brine were approximately 3600 mg/litre (Table 1). Table 15 shows test results for all evaluated samples. Values of both Brinell hardness number and TSI™ rock strength for dry and 120 minutes fluid exposure are provided.

6.4.2 Results

Table 15: Brinell Hardness number and Terra Scratch Index at dry and 120 minute fluid exposure

	CB21-13 699.69m		**CB21-15 804.39m**		**CB21-17 859.03m**	
Fluid Type and Contact Time	BHN (kgf/mm^2)	TSI (psi)	BHN (kgf/mm^2)	TSI (psi)	BHN (kgf/mm^2)	TSI (psi)
(dry)	39	16,604	27	10,783	23	9,299
Synthetic Brine (120 mins)	32	13,221	15	6,827	8	6,457

	CB21-19 917.97m		**CB21-24 987.50m**		**CB21-28 1053.86m**	
Fluid Type and Contact Time	BHN (kgf/mm^2)	TSI (psi)	BHN (kgf/mm^2)	TSI (psi)	BHN (kgf/mm^2)	TSI (psi)
(dry)	23	8,821	17	5,915	40	14.,097
Synthetic Brine (120 mins)	14	5,651	8	2,906	35	13,265

	CB140-1 511.50m		**CB140-6 585.59m**		**CB140-8 603.31m**	
Fluid Type and Contact Time	BHN (kgf/mm^2)	TSI (psi)	BHN (kgf/mm^2)	TSI (psi)	BHN (kgf/mm^2)	TSI (psi)
(dry)	14	5,707	41	17,980	37	15,708
Synthetic Brine (120 mins)	5	1,406	37	17,732	32	16,061

	CB140-12 705.27m		**CB140-17 709.99m**		**CB140-19 775.16m**	
Fluid Type and Contact Time	BHN (kgf/mm^2)	TSI (psi)	BHN (kgf/mm^2)	TSI (psi)	BHN (kgf/mm^2)	TSI (psi)
(dry)	24	7,446	21	8,694	24	7,235
Synthetic Brine (120 mins)	13	5,220	5	2,841	15	4,109

Table 15 cont'd.

	CB140-21 820.80m		CB140-24 873.37m		CB140-27 917.42m	
Fluid Type and Contact Time	BHN (kgf/mm^2)	TSI (psi)	BHN (kgf/mm^2)	TSI (psi)	BHN (kgf/mm^2)	TSI (psi)
(dry)	27	8,682	23	9,562	23	7,141
Synthetic Brine (120 mins)	13	5,675	12	6,977	14	5,048

6.5 Brazilian Tensile Strength Hardness Testing – Original Samples

6.5.1 Method

Indirect tensile strength testing (Brazilian method) was conducted on twelve samples (Figure 51) from Condabri 21 and Condabri 140. Results from indirect tensile strength testing are summarised below (Table 16). To determine tensile strength anisotropy, as a result of bedding, tests were performed at each depth interval with applied load both perpendicular and parallel to bedding as per diagram below. All tests were performed on core samples in the original dry condition.

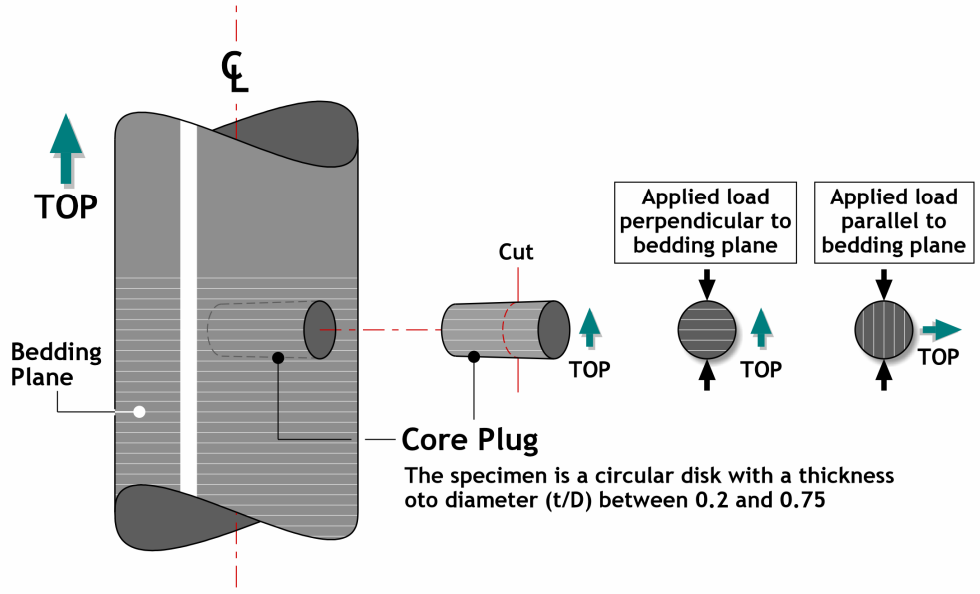

Figure 51: Core samples prepared for Brazilian Tensile strength testing.

6.5.2 Results of Tensile Strength Testing

The results of tensile strength tests for Condabri 21 and Condabri 140 are summarised in Table 16. The indirect tensile strengths in the original samples, tested by loading perpendicular to bedding, ranged from 518 psi to 1078 psi, with an average of 775 psi for Condabri 21, and ranged from 238 psi to 1180 psi, with an average of 633 psi for Condabri 140. Condabri 21 had samples tested with loading parallel to bedding, with results ranging from 230 psi to 1248 psi, with an average of 708 psi. Condabri 140 samples yielded tensile strengths ranging from 388 psi to 872 psi, with an average of 598 psi.

Table 16: Below is a summary of the results of the Indirect Tensile Strength Tests (Brazilian Method). All tests were performed on core samples in the original or air dried state.

Well	Sample ID	Depth (m)	Average Length (in)	Average Diameter (in)	Original Sample Mass (g)	Original Sample Bulk Density (g/cm^3)	Maximum Load (lbf)	Tensile Strength (psi)	Loading Orientation Relative to Bedding
Condabri 21	CB21-12A	699.54	0.530	0.999	16.410	2.411	607.1	730	Perpendicular
	CB21-12B	699.64	0.567	0.999	17.660	2.425	574.3	645	Parallel
	CB21-23A	917.81	0.555	1.000	16.170	2.264	451.4	518	Perpendicular
	CB21-23B	917.81	0.569	0.999	16.810	2.300	205.8	230	Parallel
	CB21-30A	1053.8	0.564	0.999	18.320	2.529	954.0	1078	Perpendicular
	CB21-30B	1053.8	0.494	0.999	15.970	2.517	967.5	1248	Parallel
Condabri 140	CB140-5A	585.56	0.626	0.999	20.390	2.536	1158.7	1180	Perpendicular
	CB140-5B	585.56	0.65	0.999	20.940	2.508	889.8	872	Parallel
	CB140-16A	709.96	0.554	1.000	16.760	2.351	207.1	238	Perpendicular
	CB140-16B	709.96	0.642	0.999	19.650	2.383	536.9	533	Parallel
	CB140-29A	917.48	0.620	0.999	17.740	2.228	467.1	480	Perpendicular
	CB140-29B	917.48	0.598	0.999	17.070	2.222	364.4	388	Parallel

6.5.3 Discussion

All samples tested exhibited significant reduction in Brinell hardness (Table 15) following 120 minutes exposure to synthetic brine. Reduction in hardness ranged from 13% to 65% for Condabri 21 samples and 10% to 76% for Condabri 140 samples.

All samples from Condabri 21 exhibited reduction in unconfined compressive strength, measured by scratch testing, during the soak period. Strength reduction ranged from 3% to 51%. Condabri 140 had two samples exhibit no effective reduction in unconfined compressive strength, measured by scratch testing, during the soak period while the remaining samples did exhibit weakening. Strength reduction ranged from 0% to 75%.

The two samples from Condabri 140 which had no strength reduction could be from the fine scale lithology changes within the crevasse splay (i.e. siltstone compared to sandstone). The alternate interbedded lithology may have shown different strength characteristics.

The sampling intervals were designed to correlate with the facies interpreted in Chapter 3. The WSG section is approximately 300 - 400 m thick. Condabri 21 used three samples over a 350m section with varying results whilst Condabri 140 utilised three samples over a 330m section. A total of three plugs for each well does not capture the heterogeneity within each facies.

From the SEM and thin section analysis, there is evidence of both pore filling and framework supporting distribution of clays in the analysed samples. From a qualitative determination, there is no clear trend from the clay distribution influencing disaggregation from brine saturation.

The key observation is the fact that rock strength deteriorates significantly with rock exposure to fluid, as shown by Brinell hardness test and UCS data. The UCS tests show more disaggregation than the triaxial testing as there is no confinement during testing. For a comprehensive analysis of the geomechanical conditions the in-situ stress conditions will be examined in the next chapter.

Chapter 7 - Geomechanics

7.1 Introduction

There is a subset of CSG production wells within the Walloons Fairway that display signs of fines production. Within this subset, the expression of fines production is highly variable due several factors.

1. The fines production observed to date is not easily defined by traditional methods.
2. In addition to practical experiments, where fluids can influence strength and therefore fines production, these fluids can also change the elastic properties, which, in turn, control stress distribution.
3. It is the relationship between stress and strength that dictates geomechanical behaviour.

Fines production in the broader oilfield is generally understood to be influenced by the:

- rock strength;
- in-situ stresses, and;
- flowing bottom hole pressures (FBHP).

This chapter develops one dimensional wellbore stress models (also termed mechanical earth models), with the purpose of characterising the principal in-situ stresses (maximum horizontal stress (S_{Hmax}), minimum horizontal stress (S_{hmin}) and vertical stress (S_v)). The stress models are then used to assess potential stress influences, in the context of rock strength, to assess the geomechanical influence as root cause on fines production.

7.2 Method

Sonic scanner and density wireline petrophysical log data are particularly useful for determining mechanical properties of a reservoir, as the velocity of compressional waves (V_p) and shear waves (V_s) in conjunction with rock density (ρ), can be utilised to determine the elastic moduli in an elastic, isotropic and homogenous solid (Zoback 2007).

Sonic tools measure the acoustic characteristics of a formation with the log giving a formation's slowness or interval transit time, designated Δt (delta-t) which is the reciprocal of the velocity (Rider and Kennedy 2011). The conventional approach to acoustic logging uses the transmission method, which consists of a transmitter of acoustic energy and a receiver at some distance from it. The acoustic energy is in the frequency range of about 20 kHz, and is transmitted in short bursts rather than continuously. The energy is transmitted through a portion of the rock formation surrounding the borehole (Ellis and Singer 2007).

The transmission method measures the velocity of the compressional (V_p) and shear (V_s) acoustic waves. The velocity measurements are commonly used to relate to formation porosity and lithology. It is also possible to infer and estimate abnormally high pore pressure, and to estimate dynamic mechanical rock properties, from the acoustic measurements (Ellis and Singer 2007).

Image logs provide a computer-created image based on geophysical measurements of electrical conductivity, acoustic reflectivity or formation density, which is then displayed in false colour (Rider and Kennedy 2011). An image log is commonly obtained much higher vertical resolution than other wireline logs. Standard wireline logs are sampled every 15 cm (6”), whereas image logs may sample every 2.5 mm (0.1”). Images can be produced from electrical, acoustic, density, photoelectric, gamma ray and caliper measurements (Rider and Kennedy 2011).

The higher resolution images produced by the wireline electrical tools and are mostly used for detailed, post-drilling geological interpretation, while the slightly lower resolution wireline acoustic images are mostly acquired for borehole geometry and fracture studies. The high resolution, wireline electrical imaging tools are mostly multi-pad (4 – 8 pads) type devices, with an array of small electrodes and are available for both conductive and non-conductive muds that can produce excellent detailed, oriented images. However, pad-type devices only produce an image over the zone in which the pad is in contact with the wellbore wall and, because of this design, there are normally gaps in data coverage between pads in such image logging tool results (Rider and Kennedy 2011). The Schlumberger FMI tool, used to provide resistivity image logs herein, consists of four pads on two orthogonal arms (Figure 42). The pads each have a hinged flap so as to extend the area electrical contact. The FMI runs a continuous vertical record of electrical conductivity. The standard FMI will cover approximately 40% of an 8.5” diameter hole. The FMI creates 192 micro resistivity measurements which are made every 0.1” (2.5mm) (Rider and Kennedy 2011).

For the purposes of this study, image log interpretation was focussed on the interpretation of fractures in the interburden (i.e. non-coal lithology) and stress indicators as the source of solids production. Stress indicators in coals were not considered reliable and were not used for the stress interpretation in this work. Coal is highly resistive and shows a distinct boundary on the FMI log and clean coals are in the range of 500 ohm – 3000 ohms (Crain 2008).

7.3 Image Log Analysis

The methodology used for this study is consistent with earlier work by Brooke-Barnett et al (2015). The image log interpretation was conducted to identify borehole failure caused by in situ stresses. A total of three image logs were interpreted in the study area, which show consistent trends of low differential stress. All three image logs were Schlumberger Formation Microimager (FMI) logs.

In situ stresses are manifested in the wellbore as borehole breakouts and drilling-induced tensile failure (DITF) (Walsh et al. 2010). The Kirsch equations define BOs

as zones of compressive failure due to the redistribution of in situ stress around a wellbore (Kirsch, 1898; Jaeger and Cook, 1979; Brooke-Barnett et al., 2015).

Compressive failure of the wellbore wall causes spalling, and indicates the orientation of minimum principal stress acting on a vertical borehole. This wellbore failure prevents the image log pad contacting the wellbore wall. The resistivity image log then measures the conductivity of drilling fluids, rather than rock, and results in borehole breakouts appearing as two conductive, poorly-resolved, zones of wellbore enlargement running sub-parallel to the wellbore axis and located on opposite sides of the wellbore (Figure 52) (Gough and Bell, 1982; Brooke-Barnett et al., 2015).

DITFs form in the maximum horizontal stress orientation in vertical wells (Zoback 2007). DITFs are observed on resistivity image logs as zones of narrow, conductive, well-resolved and usually sub-axial fractures, that appear on opposite sides of the wellbore (~180° apart) (Brudy and Zoback, 1999; Brooke-Barnett et al., 2015). All boreholes interpreted in this study are considered sub-vertical (borehole deviation < 20°), and, thus, the interpreted azimuths for BO and DITF can be reliably considered to reflect the S_{hmin} and S_{Hmax} orientations respectively (Mastin, 1988; Brooke-Barnett et al., 2015).

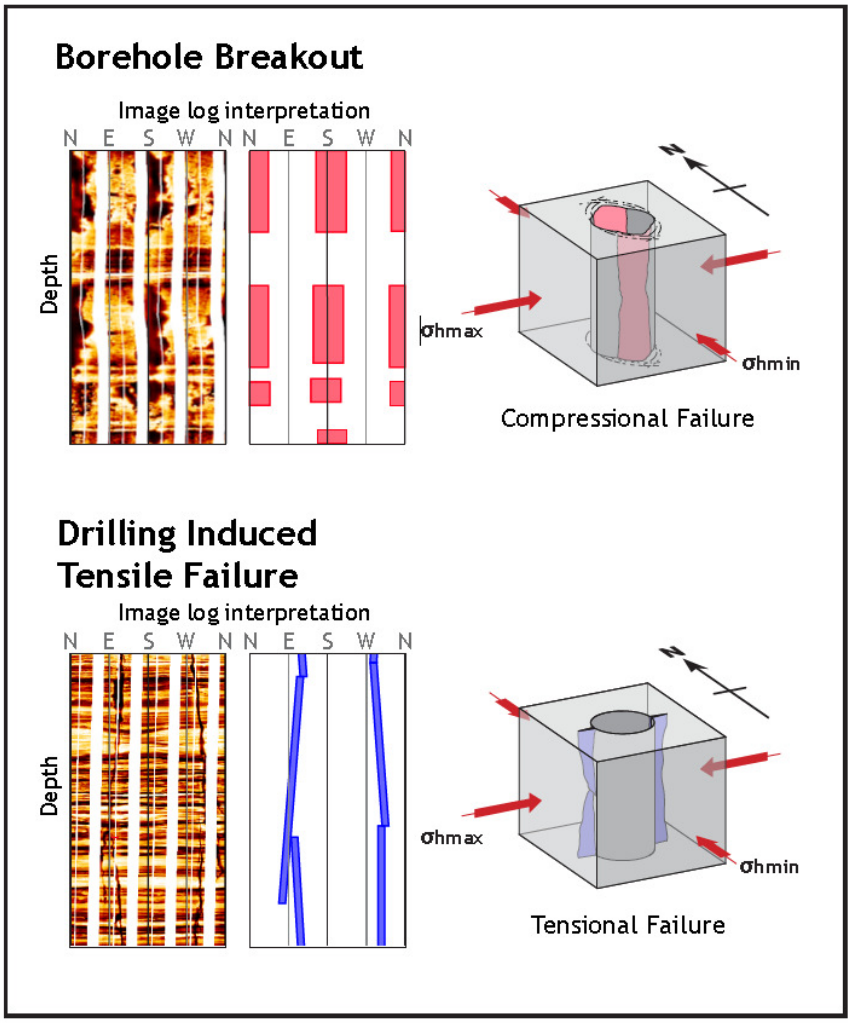

Figure 52: Borehole breakout (BO) shown in an image log (top left) with the two conductive out of focus bands 180º apart and the compressional failure manifested in the wellbore. Drilling Induced Tensile Failure (DITF) (Brooke - Barnett et al. 2015).

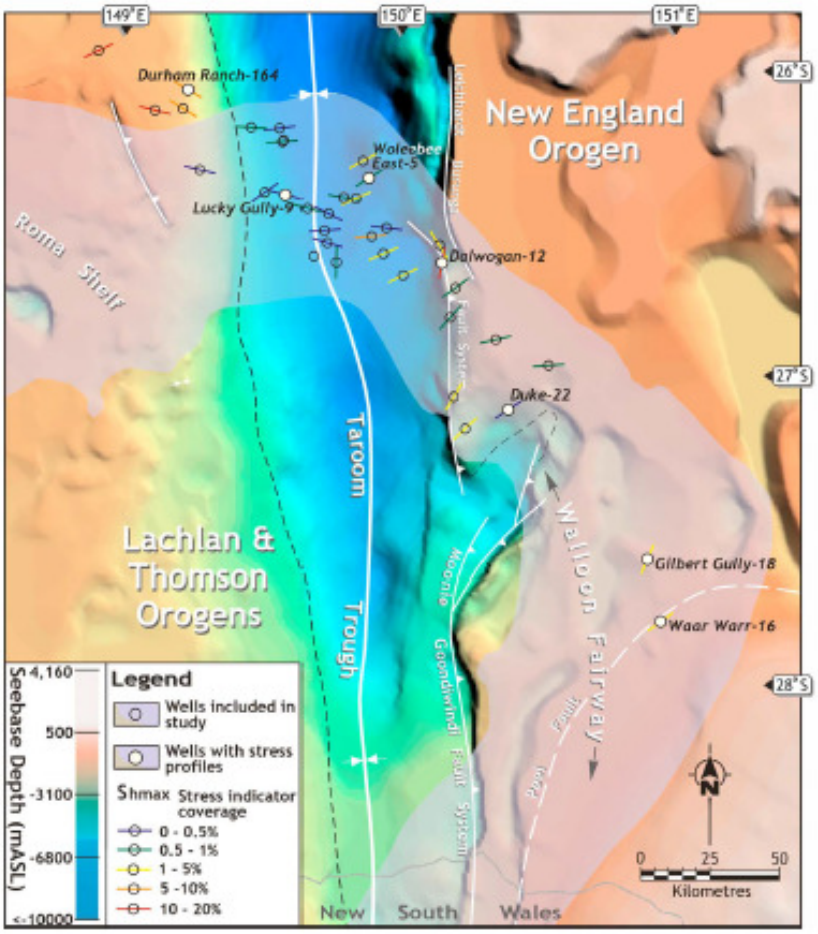

Figure 53: S_{HMax} orientations within the WSG from interpreted image logs. The percentage of image log covered by stress indicators is shown by the bar colour (Brooke - Barnett et al. 2015).

7.4 Mechanical Rock Properties

To calculate the mechanical properties, this study applies the same methodology already successfully tested and used in Brooke-Barnett et al (2015) in the study area.

1. Stresses are derived from well logs using equations 11 and 12.
2. The equations require continuous measurements of five key properties: density, static Young's Modulus, static Poisson's ratio, unconfined compressive strength (UCS) and tensile strength.
3. Density and sonic velocity-based moduli are obtained from wireline data.
4. Static moduli and strength data are only available from several discrete points from rock mechanical laboratory tests on core.

7.5 One-Dimensional Mechanical Earth Models

One-dimensional mechanical earth models for this study were calculated using the same methodology as Brooke-Barnett et al (2015).

1. Full wave sonic data and core measurements are commonly used to derive 'calibrated' models of in-situ stress profiles (Barree et al. 2009).
2. This study uses an elastic model, which is based on linear transverse isotropic elasticity and a failure model that is based on the concept that rocks are in an equilibrium state of shear failure (Thiercelin and Plumb 1994).
3. Continuous logs of elastic rock properties were created using sonic scanner data and calibrated at several discrete points using laboratory tested core samples.
4. The in situ stresses were characterised by determining the orientation and the magnitude of the three principal stresses (S_{Hmax}, S_{hmin} and S_v).
5. The orientation of S_{Hmax} and S_{hmin} were determined using image logs from three wells.
6. The magnitude of S_{Hmax}, S_{hmin} and S_v were estimated using 1D MEMs.

7.5.1 Poisson's Ratio

Poisson's Ratio (v) is the ratio of lateral to longitudinal strain for a sample, and thus describes how much a material that is compressed under a load will expand in a perpendicular direction to that load (Fossen 2010).

There are two methods used herein which provide the static and dynamic Poisson's ratio. The static Poisson ratio (V_{static}) is obtained from unconfined loading test, which directly measure the ratio of radial strain and axial strain (ε_r / ε_z). The dynamic Poisson's Ratio (V_{dyn}) is obtained by measuring the compressional and shear velocities from sonic velocity data and equation 2 below, which provides a readily available estimate of Poisson's ratio, but at smaller strains and higher frequencies than is suitable for geomechanical modelling (Zhang and Bentley 2005).

$$v_{dyn} = \frac{\left(V_p / V_s\right)^2 - 2}{2\left[\left(V_p / V_s\right)^2 - 1\right]}$$

Equation 2: The equation used to determine the Dynamic Poisson's Ratio. Where V_p is compressional sonic velocity in m/s and V_s is shear sonic velocity in m/s.

V_s = Shear Velocity (m/s)
V_p = Compressional Velocity (m/s)
v_{dyn} = Poisson's Ratio (Dynamic)
V_s = Shear Velocity (m/s) = 0, it is characteristic of a gas reservoir;

7.5.2 Young's Modulus

Young's modulus describes the relationship between longitudinal stress and longitudinal strain (E = σ/e) (Fossen 2010). The modulus is an elastic constant needed to characterise the elastic behaviour of an isotropic material (Twiss and Moores 2007). In unconfined compression, the sample shortens parallel to the applied stress. Young's modulus (or the *"stretch modulus"*) describes the behaviour of a rod (or material specific) that is pulled or compressed (Lillie 1999).

$$E_{dyn} = \frac{\rho V_s^{\,2}\left(3V_p^{\,2} - 4V_s^{\,2}\right)}{V_p^{\,2} - V_s^{\,2}}$$

Equation 3: The equation used to calculate the dynamic Young's Modulus. Where ρ is density in kg/m^2, V_p is compressional sonic velocity in m/s and V_s is shear sonic velocity in m/s

P = Density (kg / m^3)

V_s = Compressional Velocity (m/s)

V_p = Shear Velocity (m/s)

E_{dyn} = Young's Modulus (Dynamic)

Values of Young's Modulus (E) and Poisson's Ratio (v) can be determined from core samples (both static and dynamic acoustic tests) and from well log (acoustic measurements). The accuracy and applicability of these derived properties has a direct impact on the calculated stress profile, even when it is calibrated to a single point of measured closure stress. When rock properties and environmental or test conditions affect the apparent mechanical properties, errors in stress and fracture geometry can result (Barree et al. 2009).

From the previous regional work by Brooke-Barnett et al (2015), this study uses the below equations as the dynamic to static conversions:

$$v_{stat} = 0.7 v_{dyn} + 0.06$$

Equation 4: Sandstone static Poisson's ratio. Where V_{dyn} is the dynamic Poisson's Ratio.

$$v_{stat} = 0.7 v_{dyn} + 0.08$$

Equation 5: Siltstone static Poisson's ratio. Where Vdyn is the dynamic Poisson's Ratio.

$$E_{stat} = 0.32 E_{dyn}$$

Equation 6: Sandstone static Young's Modulus. Where Edyn is the dynamic Young's Modulus.

$$E_{stat} = 0.3 E_{dyn}$$

Equation 7: Siltstone static Young's Modulus. Where E_{dyn} is the dynamic Young's Modulus.

$$\varphi = \sin^{-1}\left(\frac{V_p - 1000}{V_p + 1000}\right)$$

Equation 8: Friction Angle (°) [*Lal*, 1999] where Vp is compressional sonic velocity in m/s.

$$UCS = 1200 e^{(-0.036 \Delta t)}$$

Equation 9: Sandstone compressive rock strength (MPa) (McNally 1987). Where Δt is the compressional sonic slowness in μs/ft

7.5.3 Vertical Stress (Overburden)

$$S_V = \int_0^z \rho(z)\, g\, dz$$

Equation 10: Where z is depth below ground level, ρ is density in kg/m2, g is acceleration due to gravity assumed 9.81 m/s2.

7.5.4 Maximum Horizontal Stress

$$S_{Hmax} = \frac{v_{stat}}{1 - v_{stat}}\left(S_V - \alpha P_p\right) + \frac{E_{stat}}{\left(1 - v_{stat}^{\ 2}\right)}\left(\varepsilon_{max} + v_{stat}\varepsilon_{min}\right) + \alpha P_p$$

Equation 11: Maximum Horizontal Stress.

Where v_{stat} is the static Poisson's Ratio, S_v is the vertical stress, α is the Biot's coefficient P_p is the formation pressure, E_{stat} is the static Young's Modulus, ε_{max} is the strain in the maximum horizontal stress direction and ε_{min} is the strain in the minimum horizontal stress direction. The strains (ε_{max} and ε_{min}) could not be measured directly and the values utilised by Brooke-Barnett et al (2015) have been used (ε_{max} = 0.0009 and ε_{min} = 0.0003).

7.5.5 Minimum Horizontal Stress

$$S_{Hmin} = \frac{v_{stat}}{1 - v_{stat}}\left(S_V - \alpha P_p\right) + \frac{E_{stat}}{\left(1 - v_{stat}^{\ 2}\right)}\left(\varepsilon_{min} + v_{stat}\varepsilon_{max}\right) + \alpha P_p$$

Equation 12: Minimum horizontal stress.

Where v_{stat} is the static Poisson's Ratio, S_v is the vertical stress, α is the Biot's coefficient P_p is the formation pressure, E_{stat} is the static Young's Modulus, ε_{max} is the strain in the maximum horizontal stress direction and ε_{min} is the strain in the minimum horizontal stress direction.

7.6 Model Calibration

7.6.1 Fracture Tests

To calculate the mechanical properties, this study applies the same methodology as Brooke-Barnett et al (2015).

1. Fracture tests are a generic name for various tests that isolate a section of a borehole, initiate tensile failure within that section, and monitor pressure decline as the fracture closes under tectonic stress. Examples include extended leak-off tests (XLOTs), Diagnostic Fracture Injection Tests (DFITs) and minifracture tests.
2. Closure pressures (Pc) derived from fracture tests are indicative of the minimum principal stress at the test depth (Hubbert and Willis 1957; Zoback 2007).
3. Within a reverse tectonic regime, fracture closure pressures are more likely to be indicative of the S_v, whereas in a strike-slip or normal tectonic regime, closure pressures give a reasonable approximation of the SHmin due to the orientation of the fracture propagated during the fracture test (Brudy and Zoback 1999; Zoback 2007).
4. Pc values were estimated by investigating the change in pressure response from the isolated section over time using G-function derivative analysis and log-log derivative analysis (Barree et al. 2007).

7.6.2 Borehole Failure

To calculate the mechanical properties, this study applies the same methodology as Brooke-Barnett et al (2015).

1. Borehole failure are useful for constraining horizontal stress orientation, but can also be used to constrain the magnitude of stresses acting on a borehole if there is suitable knowledge of rock mechanical properties and failure criteria.
2. Borehole breakout (BHBO) represents areas where the compressional rock strength has locally been exceeded by the redistribution of in situ stresses around the borehole wall (Bell 1990; Zoback et al. 1985).
3. Conversely, DITFs represent areas where the tensional rock strength has locally been exceeded (Aadnoy 1990).
4. The possible range of stress conditions necessary to match observed borehole failure can be predicted if there are sufficient constraints on mechanical properties, S_v, Pp, and mud weight at a given depth (Moos and Zoback 1990).
5. Maximum and minimum limits for S_{Hmax} and S_{hmin} were based on incidences of BHBO and DITF, as well as lithology, mechanical rock properties, Pp, Pm, and S_v at the depth of borehole failure occurrence
6. These limits are also dependent on rock failure envelope parameters
7. A modified Lade failure criterion, a coefficient of sliding friction (μs) of 0.6, and a coefficient of internal friction (μ_i) of 1 were initially used for calibration points. However due to the significant amount of variability of in situ stress conditions over the Surat Basin, core data was used, where available.

Although there are very few independent stress indicators from the image logs in Condabri 21, the stress regime is estimated to change over the well, and display the following stress regimes with depth.

1. Reverse fault regime (σH > σh > σV) from 200 mRT (surface casing) to 410mRT.
2. Strike-slip regime (σH > σV > σh) from 410 mRT – 1020 mRT.
3. Normal fault regime (σV > σH > σh) from 1020 mRT – 1110 mRT.

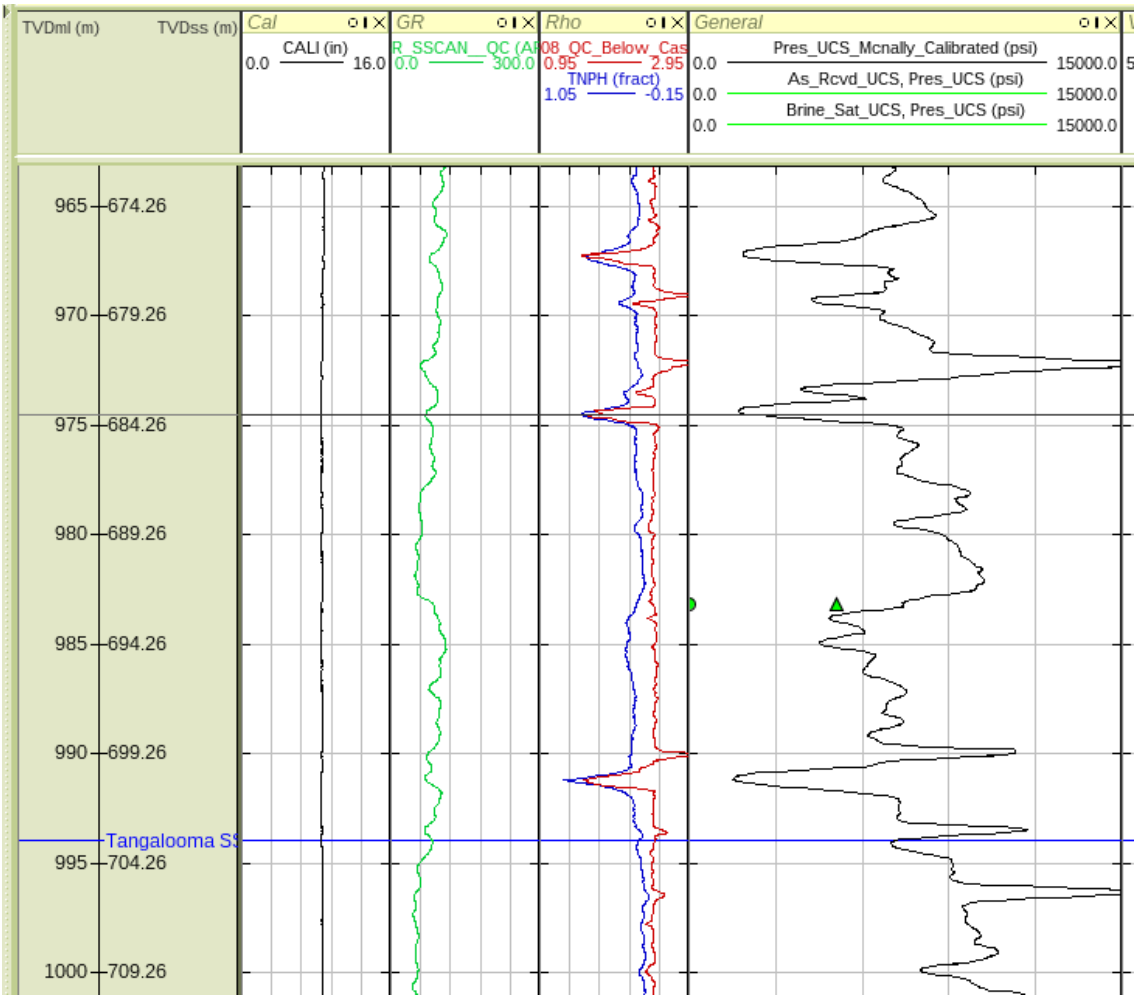

Figure 54: A plot from Condabri 21 of the wireline data (from left to right), Caliper (black), GR (green), Neutron (blue) / Density (red), calculated rock strength (black) using the McNally equation with the original sample UCS (green triangle) and the brine saturated UCS (green circle). A UCS value of 0 psi is used for the brine saturated samples that disaggregated.

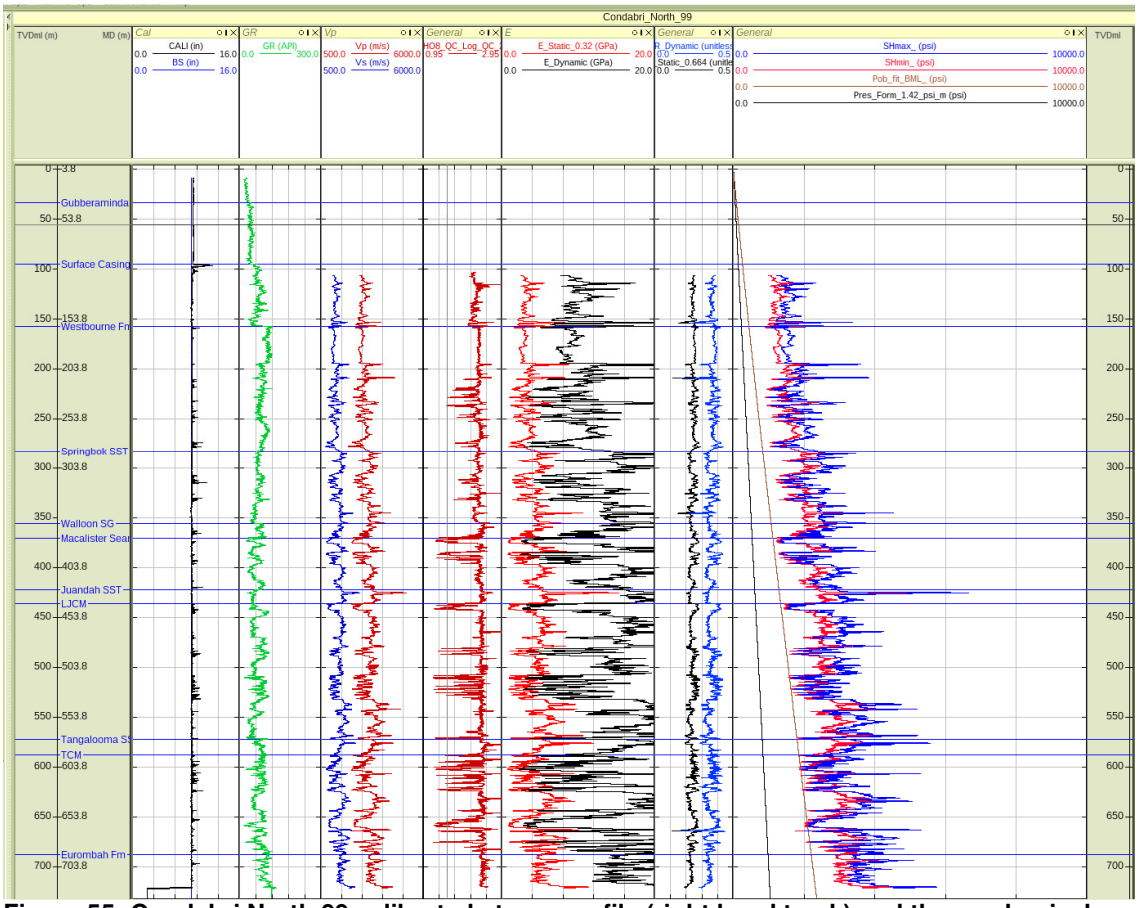

Figure 55: Condabri North 99 calibrated stress profile (right hand track) and the mechanical parameters used to calculate the stress profile.

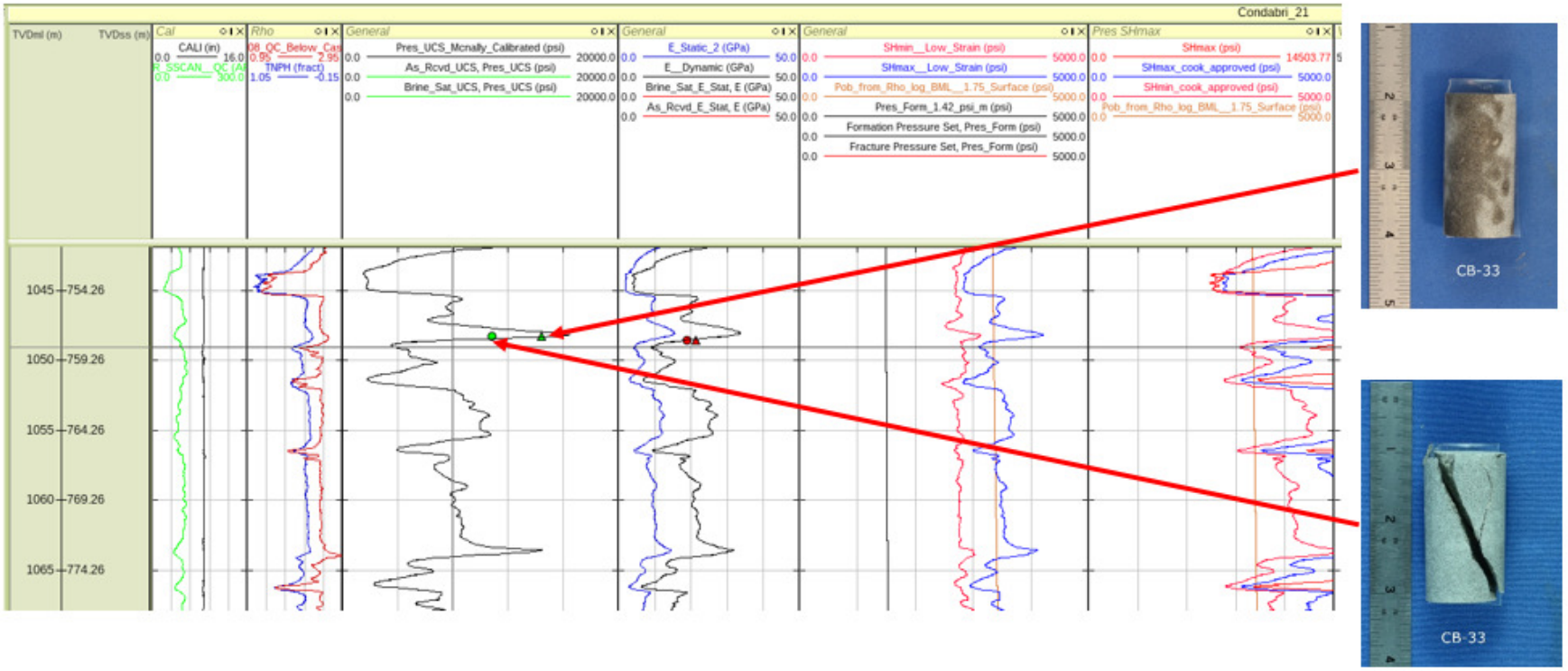

Figure 56: A plot from Condabri 21 of the wireline data (from left to right), Caliper (black), GR (green), Neutron (blue) / Density (red), calculated rock strength (black) using the McNally equation with the as-received UCS (green triangle) and the brine saturated UCS (green circle). The brine saturated sample remained competent with a variation in the UCS from 14,460 psi (original sample) to 10,875 psi (brine saturated). From the FMI interpretation, the wellbore is shown to be in an area of low differential stress. However, the fluid saturation impacts the mechanical properties.

7.7 Results

In the context of regional stress analyses (Flottmann et al. 2013; Brooke‐Barnett et al. 2015; Tavener et al. 2017), the WSG of the Condabri Field is considered a low differential stress area, as the differential stresses are between 200 - 600 psi, whereas in other areas, the differential stresses can be up to 2000 psi. The stress regimes also fit with regional trends for correlation with depth. The stress regimes observed in Condabri 21 shows a reverse fault regime (200 - 410mRT), strike-slip regime (410 – 1020 mRT) and a normal fault regime (1020 – 1110 mRT).

In addition, rock mechanics tests in Chapter 6 clearly demonstrated that post-drill fluid saturation (exposure) has a fundamental influence on rock strength – even in samples that do not disaggregate. From the uncalibrated MEM, the stress state is lithology dependent.

7.8 Discussion

The key finding of stress analysis conducted herein is that the WSG in the Condabri area has a present-day horizontal differential stress in the range of 200 – 600 psi. This is a relatively low horizontal differential stress regime, in the context of the differential stresses in the region (Brooke‐Barnett et al. 2015). This is in line with the observation that there are very few indicators (breakout and/or DITFs) of elevated horizontal differential stresses in image logs (mud weight is consistently at 8.7 – 9.1 ppg throughout drilling).

A comparison of stress models (Figure 57) demonstrates the variation in the rock properties between original and brine saturated samples. Both models use the regional low difference stress variations of 300 psi. The friction angle used for the brine saturated sample assumes a conservative reduction of 10º. The assumption is that the friction angle is lowered significantly in the brine saturated cores as shown by reduced UCS evident in scratch tests on brine saturated samples.

The key finding is there is little obvious evidence for fines production coming from primarily stress induced mechanical failure. The fines production is primarily due to chemically induced disaggregation, rather than stress concentration around the wellbore.

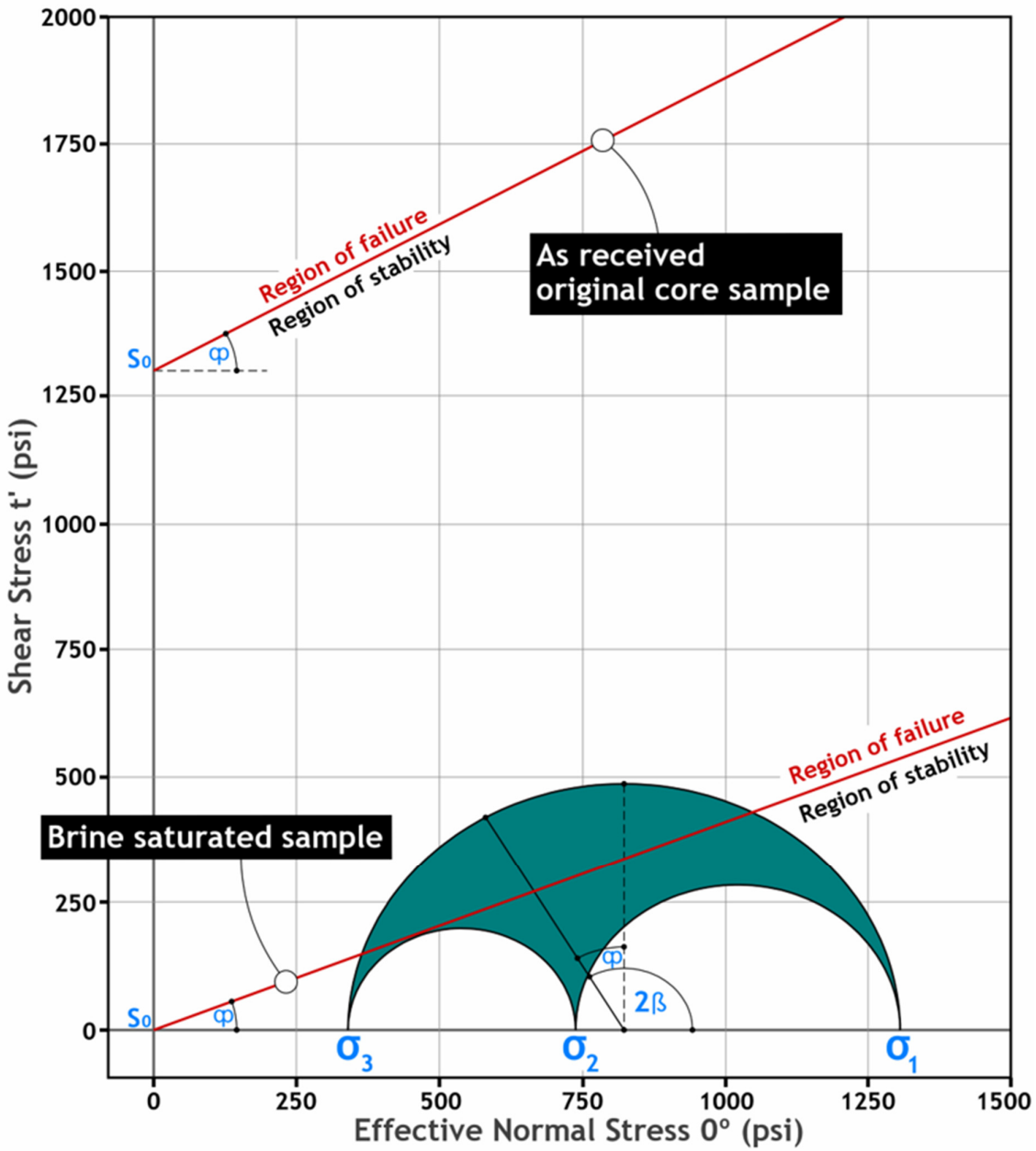

Figure 57: Condabri 140 at 700mRT showing the stress model for the interburden from the original core samples. The Mohr's circle demonstrates how close the as received (in their effective room dry condition) original core samples are to shear failure in this zone compared to the brine saturated sample under the same stress conditions.

The low differential stresses, in context of the established rock strength results (see Chapter 6), make it somewhat unlikely that differential stresses are a main contributing factor controlling rock disintegration leading to excessive fines production. However, there is a noticeable impact on the mechanical properties after rocks have been interacted with produced water. The interaction of fluid weakened rocks with in-situ stresses may enhance disintegration under in-situ stresses. High rock strength in unaltered rocks (i.e. not subjected to fluid rock interaction) and low differential ambient stresses make it unlikely that stress-rock interaction is a primary cause for rock disintegration and fines production. Notably flowing bottom hole pressures remain basically hydrostatic in the early phases of CSG production.

Chapter 8 – Discussion, Implications, Conclusions

8.1 Discussion

The objective of the study was to identify root causes and potential mitigation options of fines production in the Walloons Sub Group (WSG) of the Jurassic Surat Basin in southeast Queensland, Australia. Fines production is evidenced by accumulation of fine grained clastic material in separators of many Coal Seam Gas (CSG) wells, as documented in the Introduction to this thesis (Figure 1). The initial approach was to characterise fines production in context of geomechanical parameters (i.e. rock strength, in-situ stresses, flowing bottom hole pressures). However, it became progressively clear that fines production is dominated by disaggregation of rock influenced by clays which are abundantly present throughout the WSG. Clays were deposited as part of volcaniclastic sediments that were deposited due to volcanic activity that prevailed throughout the deposition of the WSG, as documented in the Geological Summary of Chapter 2.

Chapter 3 documents the impact fluid-rock interaction; simple laboratory experiments show the fundamental impact of reconstituted brine (resembling produced water) on interburden rocks leading to disaggregation of interburden rocks under static (i.e. non-flowing) wellbore conditions. Soak tests of interburden rock material with various additives show that KCl of sufficient concentration (>3%) results in a degree of rock stabilisation and prevention of disaggregation. Whilst the in principal phenomenon of fines generation appears relatively easy to document, the obvious challenge is to understand whether fines production can be understood in context of facies types or specific interburden lithologies. This would potentially allow use of wireline logs to predict lithologies of facies more or less prone to rock disaggregation and targeting i.e. lithology or facies specific fines mitigation and/or inhibition of fines production.

Core facies logging and petrographic analyses presented in Chapter 4 in combination with petrophysical analyses presented in Chapter 5 suggest that fines production is not related to a specific depositional facies, and importantly not related to a specific clay type as shown by XRD analyses. Furthermore, analyses presented in Chapter 5 suggest that the fines fractions of dispersed clays do not result in a distinct wireline log signature, even when using ‘high-end’ compositional (ECS) wireline logs, which are not normally run as part of the standard wireline logging suite used in CSG wells. Moreover, the disaggregation of interburden cannot be clearly attributed to a specific volume of clay contained in the rock.

Rock strength testing (Chapter 6) shows that rock strength deteriorates significantly with rock exposure to fluid, as shown by Brinell hardness test and Unconfined Compressive Strength (UCS) testing. The results of rock strength testing in combination with in-situ stress characterisation from image logs (breakouts and drilling induced tensile fractures; DITFs) are used to calibrate rock property derived stress logs which together form the foundation of the geomechanical analyses presented in Chapter 7. The geomechanics and rock strength analyses suggest that in-situ horizontal differential

stress is likely relatively low, and that the interburden rocks are not prone to significant stress-induced failure. Thus, there appears to be no clear contribution of present-day stresses to rock disaggregation and fines production.

Essentially the results of this thesis suggest that fines production in the WSG of the Surat Basin is not controlled by geomechanical influences, but fines production is much rather an effect of rock fluid interaction leading to disaggregation of clays, which are present in varying abundance throughout the WSG.

8.2 Implications and way-forward options

As fines producing lithologies cannot be readily identified form wireline logs it appears more sensible to concentrate on mitigation methods that allow bulk exclusion of fines from wellbore and gathering system. This includes completing wells with blank casing (instead of pre-perforated casing), cementing and then perforating coals to deploy skin fracs for reconnection. The results presented here further suggest that short term stabilisation can be achieved by displacing fluid in wells to KCl provides an effective and cheap option, to inhibit rock disaggregation of interburden, thus intermittently stabilizing CSG wells.

Future well designs (including horizontal wells) have to concentrate primarily on fines exclusion, rather than post drill mitigation of fines production. In context of the results presented here future research on fines inhibition has to aim at (a) stabilizing the interburden to inhibit fines production and (b) to allow access to the coal permeability system (fractures and cleats). Any chemical additive aiming at permanently stabilizing the interburden in producing CSG wells has to achieve interburden stabilization without obstructing the coal permeability system. Alternatively access to coal permeability can be achieved by mechanically reconnecting coals to the wellbore (e.g. perforating).

8.3 Conclusions

The key conclusions of this work are as follows:

1. Interburden rocks in the Walloons Subgroup (WSG) of the Surat Basin, southeast Queensland, Australia are affected by significant solids production
2. Fluid rock interaction is the primary mechanism leading rock disintegration resulting in fines production
3. Clay mineral content and swelling of clays is the primary mechanism for rock disintegration and fines production in the WSG
4. Core facies log and petrographic analysis show that volcanogenic clay minerals occur in all interburden rocks of the WSG regardless of facies type; clays are not always obvious in core. The volcaniclastic sediments observed would be consistent with the volcanic arc influenced deposition environment.
5. Petrophysical analysis show that discrete volumes of clays can be misinterpreted or misread due to wireline logging tool resolution constraints.
6. Rock strength testing shows that rock strength deteriorates significantly with rock exposure to fluid, as shown by Brinell hardness test and UCS data.

7. The geomechanical models and rock strength analyses suggest that in-situ horizontal differential stress is likely relatively low, and that the interburden is not observing significant stress-induced failure. Thus, there appears to be no clear contribution of present-day stresses to rock disaggregation and fines production.

Appendix A

Stress strain curves from multi-stage triaxial testing.

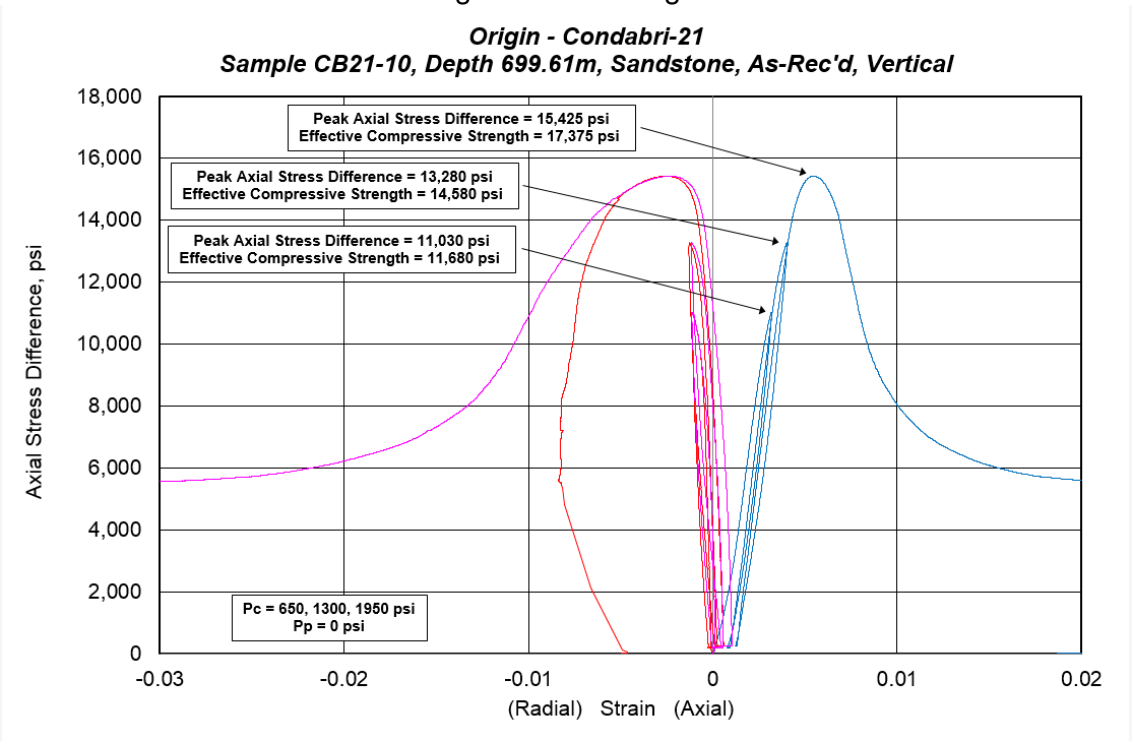

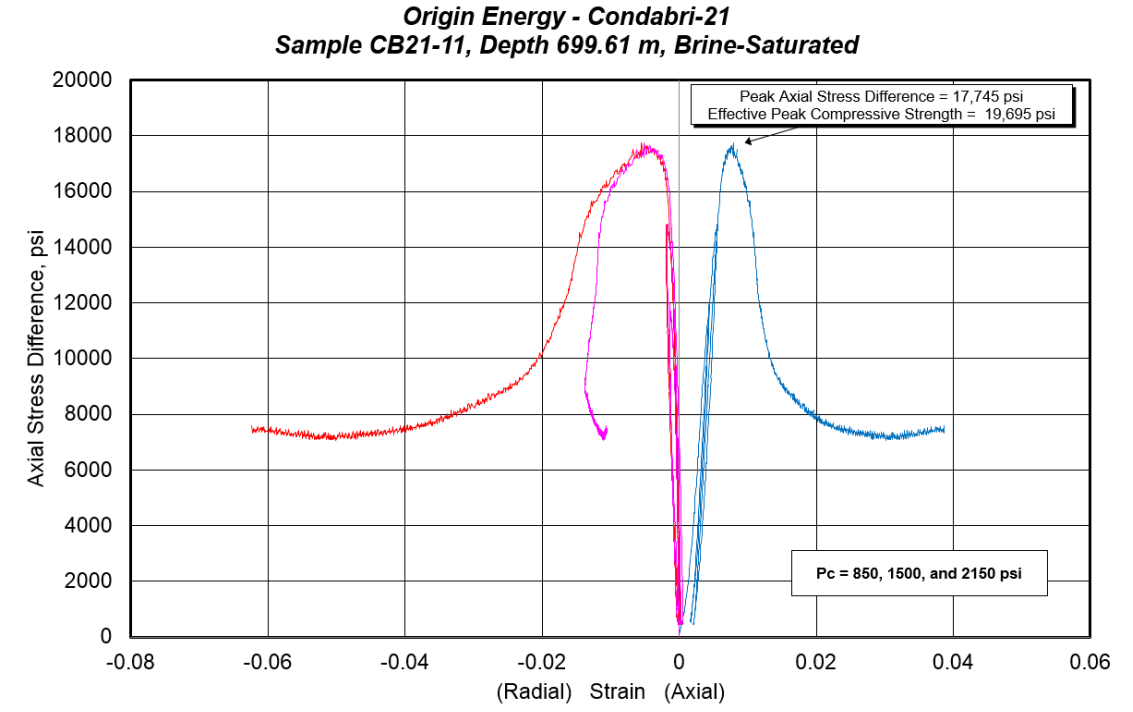

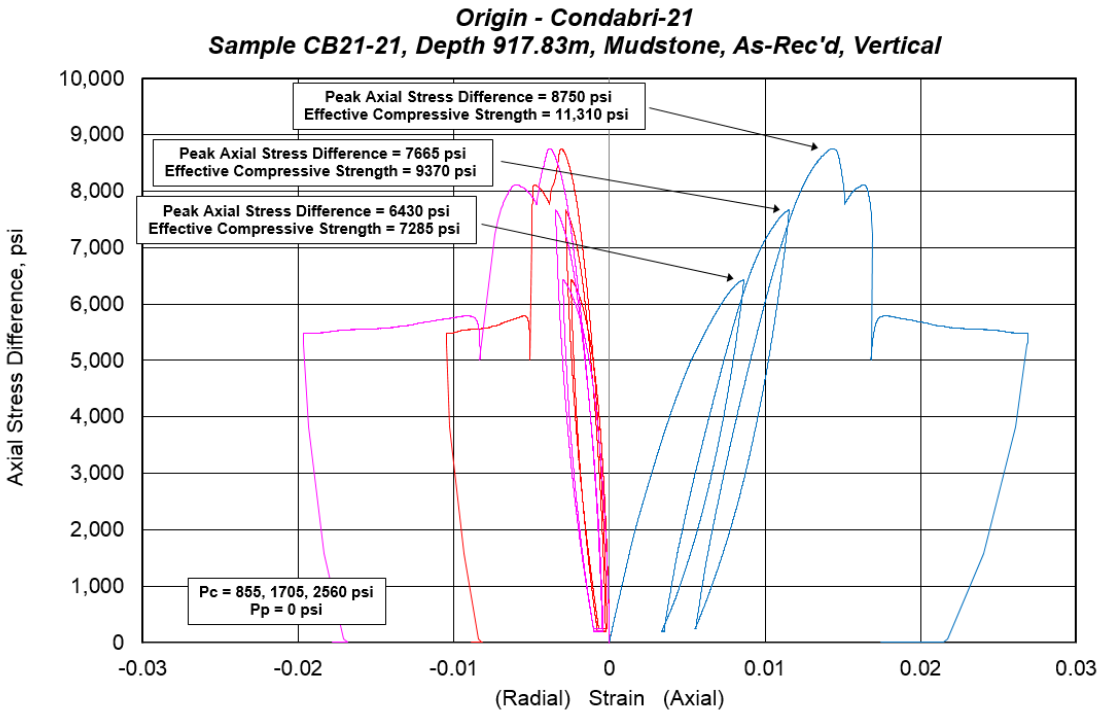
Origin - Condabri-21
Sample CB21-21, Depth 917.83m, Mudstone, As-Rec'd, Vertical
Peak Axial Stress Difference = 8750 psi
Effective Compressive Strength = 11,310 psi
Peak Axial Stress Difference = 7665 psi
Effective Compressive Strength = 9370 psi
Peak Axial Stress Difference = 6430 psi
Effective Compressive Strength = 7285 psi
Pc = 855, 1705, 2560 psi
Pp = 0 psi
Axial Stress Difference, psi
10,000
9,000
8,000
7,000
6,000
5,000
4,000
3,000
2,000
1,000
0
-0.03
-0.02
-0.01
0
0.01
0.02
0.03
(Radial) Strain (Axial)

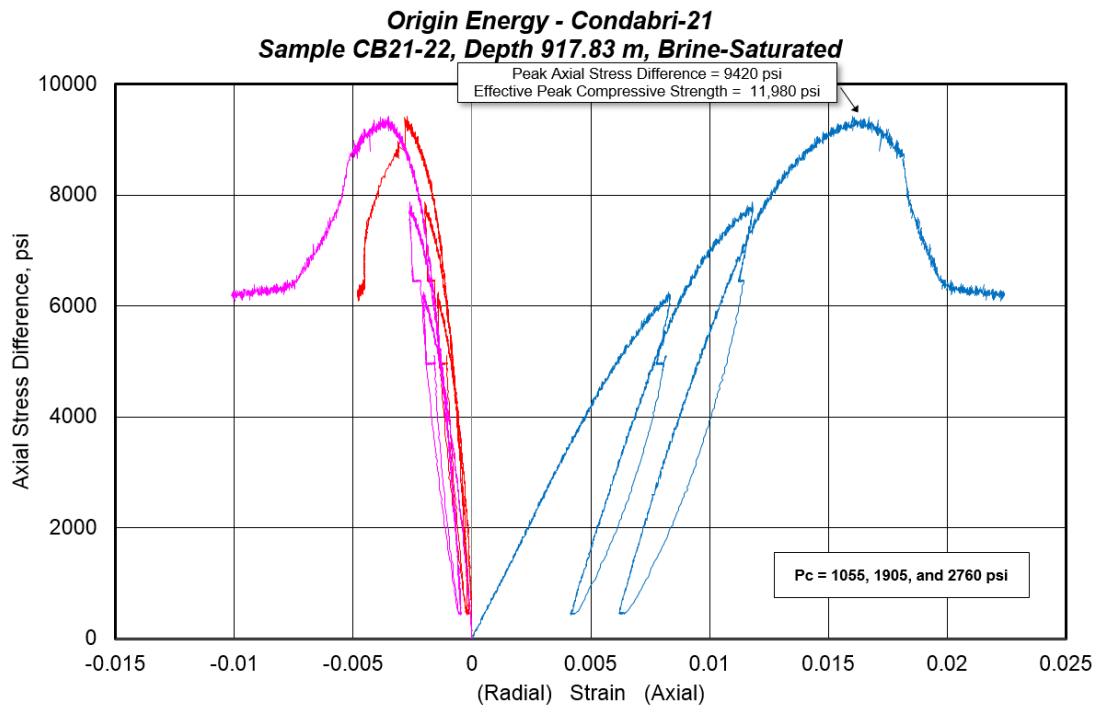
Origin Energy - Condabri-21
Sample CB21-22, Depth 917.83 m, Brine-Saturated
Peak Axial Stress Difference = 9420 psi
Effective Peak Compressive Strength = 11,980 psi
Pc = 1055, 1905, and 2760 psi
Axial Stress Difference, psi
10000
8000
6000
4000
2000
0
-0.015
-0.01
-0.005
0
0.005
0.01
0.015
0.02
0.025
(Radial) Strain (Axial)

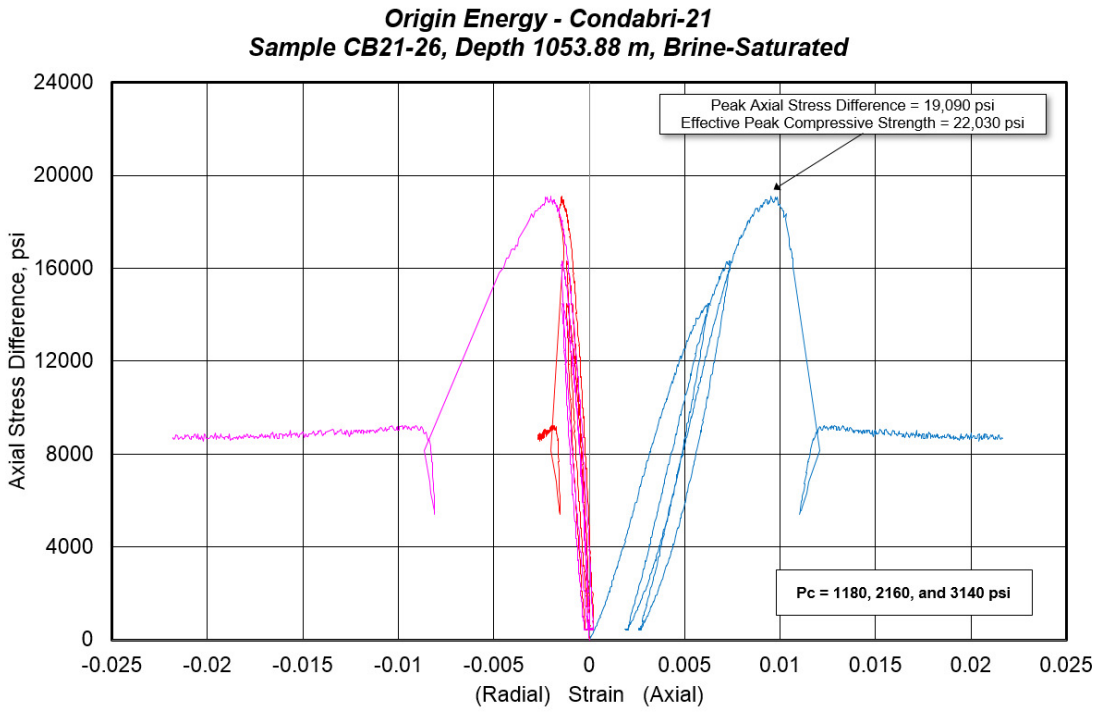
Origin Energy - Condabri-21
Sample CB21-26, Depth 1053.88 m, Brine-Saturated
Peak Axial Stress Difference = 19,090 psi
Effective Peak Compressive Strength = 22,030 psi
Pc = 1180, 2160, and 3140 psi
Axial Stress Difference, psi
24000
20000
16000
12000
8000
4000
0
-0.025
-0.02
-0.015
-0.01
-0.005
0
0.005
0.01
0.015
0.02
0.025
(Radial) Strain (Axial)

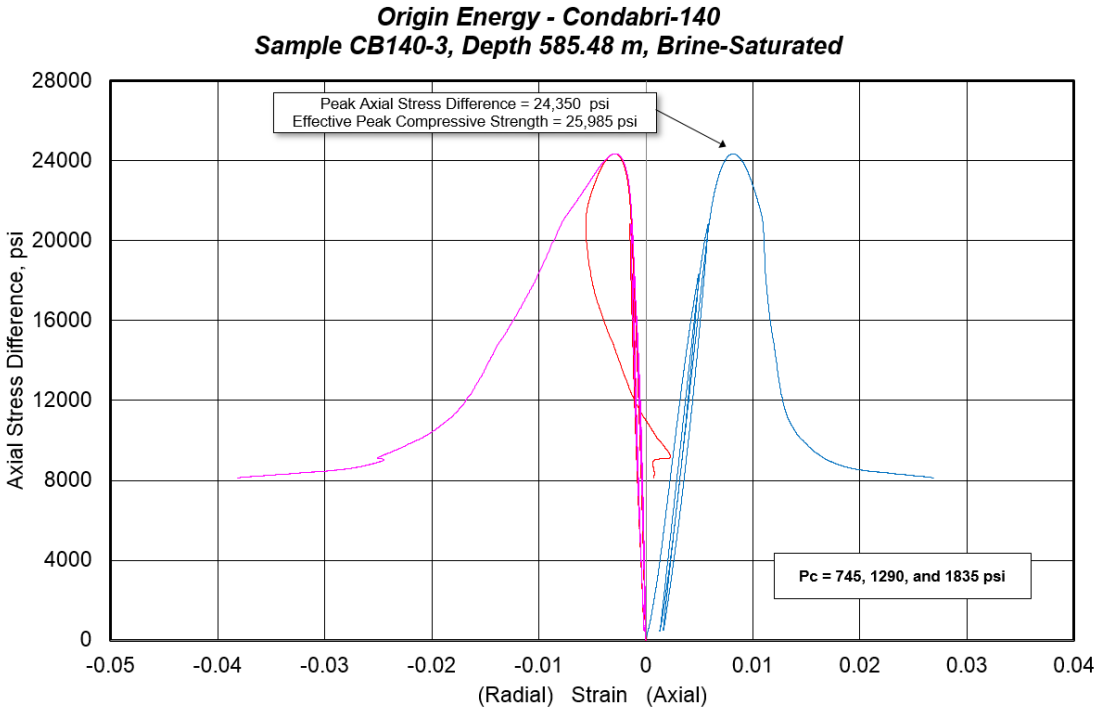
Origin Energy - Condabri-140
Sample CB140-3, Depth 585.48 m, Brine-Saturated
Peak Axial Stress Difference = 24,350 psi
Effective Peak Compressive Strength = 25,985 psi
Pc = 745, 1290, and 1835 psi
Axial Stress Difference, psi
28000
24000
20000
16000
12000
8000
4000
0
-0.05
-0.04
-0.03
-0.02
-0.01
0
0.01
0.02
0.03
0.04
(Radial) Strain (Axial)

Origin Energy - Condabri-140
Sample CB140-14, Depth 709.95 m, Brine-Saturated

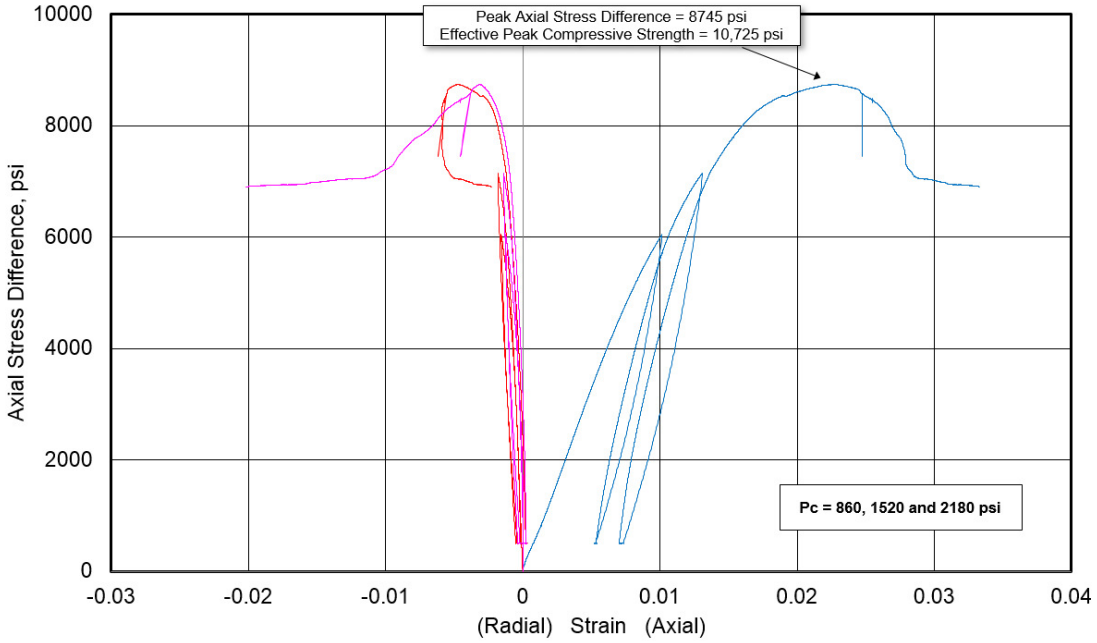

Origin Energy - Condabri-140
Sample CB140-25, Depth 917.50 m, Brine-Saturated

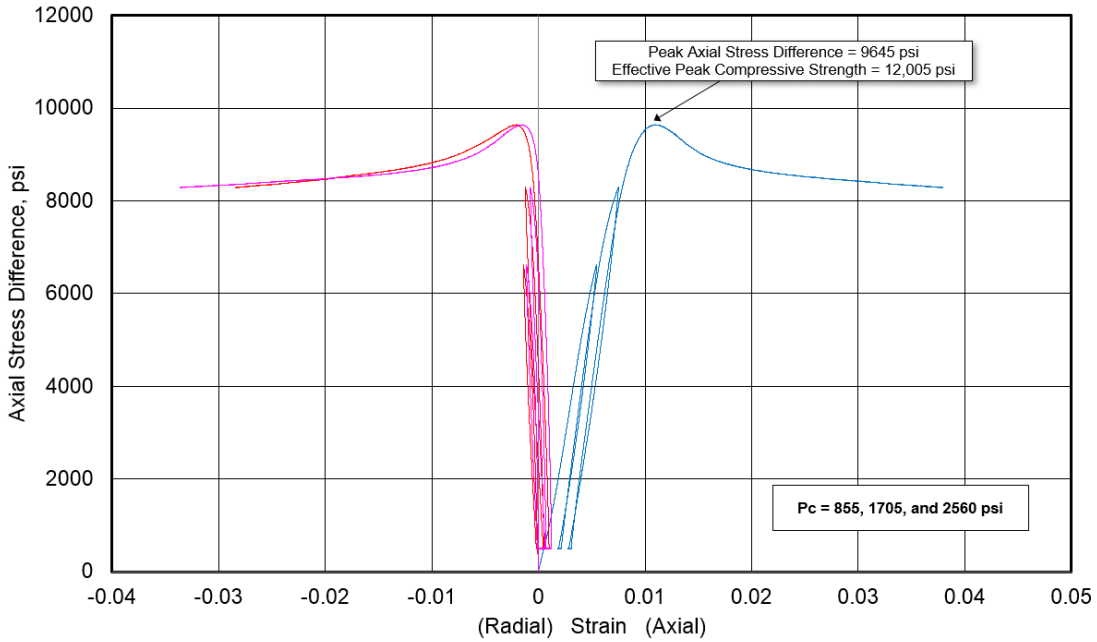

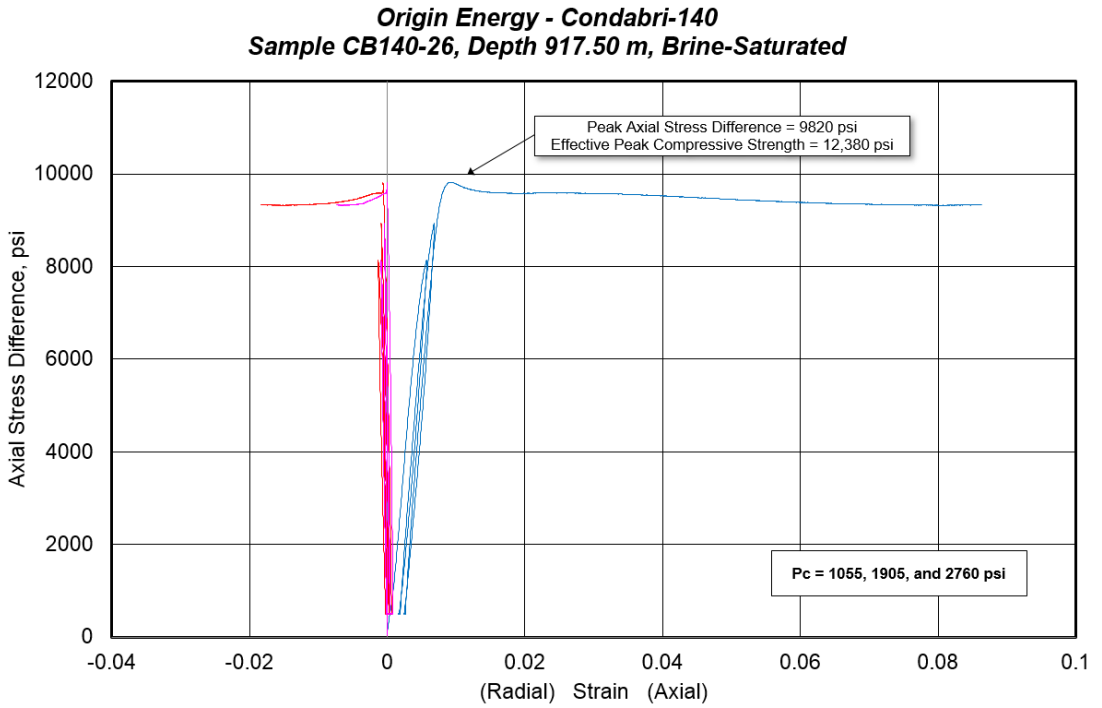
Origin Energy - Condabri-140
Sample CB140-26, Depth 917.50 m, Brine-Saturated
Peak Axial Stress Difference = 9820 psi
Effective Peak Compressive Strength = 12,380 psi
Pc = 1055, 1905, and 2760 psi
Axial Stress Difference, psi
12000
10000
8000
6000
4000
2000
0
-0.04
-0.02
0
0.02
0.04
0.06
0.08
0.1
(Radial) Strain (Axial)

Appendix B

Dynamic mechanical properties determined during multi-stage triaxial compression testing.

Well	Sample ID Depth (m) Lithology	Axial Stress Difference (psi)	Confining Pressure (psi)	Pore Pressure (psi)	Effective Mean Stress (psi)	As-Tested Density (g/cm^3)	P-Wave Velocity (ft/s)	S-Wave Velocity (ft/s)	Poisson's Ratio	Young's Modulus (10^6 psi)	Bulk Modulus (10^6 psi)	Shear Modulus (10^6 psi)
Condabri-21	CB21-10 As-received 699.61 Sandstone	4	650	0	651	2.421	11,702	7467	0.16	4.208	2.042	1.819
		1595	650	0	1182	2.423	13,802	8001	0.25	5.211	3.433	2.090
		2809	650	0	1586	2.423	14,621	8283	0.26	5.662	3.993	2.240
		4992	650	0	2314	2.424	15,030	8515	0.26	5.985	4.221	2.368
		7152	650	0	3034	2.424	15,271	8603	0.27	6.129	4.395	2.418
		10587	650	0	4179	2.424	15,346	8554	0.27	6.092	4.505	2.390
		199	1300	0	1366	2.425	13,311	8040	0.21	5.124	2.973	2.112
		1688	1300	0	1863	2.426	14,446	8293	0.25	5.638	3.824	2.248
		2993	1300	0	2297	2.426	14,978	8445	0.27	5.907	4.226	2.331
		4744	1300	0	2881	2.426	15,225	8547	0.27	6.066	4.395	2.388
		8274	1300	0	4058	2.427	15,553	8604	0.28	6.195	4.682	2.421
		12116	1300	0	5339	2.426	15,568	8572	0.28	6.162	4.721	2.402
		249	1950	0	2033	2.428	14,031	8329	0.23	5.574	3.415	2.270
		1776	1950	0	2542	2.428	14,423	8441	0.24	5.779	3.698	2.331
		3732	1950	0	3194	2.429	14,932	8542	0.26	6.002	4.113	2.388
		7755	1950	0	4535	2.429	15,259	8602	0.27	6.138	4.392	2.422
		12760	1950	0	6203	2.429	15,338	8560	0.27	6.109	4.501	2.398
		15346	1950	0	7066	2.425	15,450	8215	0.30	5.746	4.860	2.205
		5556	1950	0	3802	2.380	14,306	7526	0.31	4.755	4.141	1.817

Well	Sample ID Depth (m) Lithology	Axial Stress Difference (psi)	Confining Pressure (psi)	Pore Pressure (psi)	Effective Mean Stress (psi)	As-Tested Density (g/cm^3)	P-Wave Velocity (ft/s)	S-Wave Velocity (ft/s)	Poisson's Ratio	Young's Modulus (10^6 psi)	Bulk Modulus (10^6 psi)	Shear Modulus (10^6 psi)
Condabri-21	CB21-11 Brine Saturated 699.61 Sandstone	29	850	197	662	2.429	14,730	8511	0.25	5.924	3.939	2.371
		884	850	200	945	2.430	15,099	8779	0.24	6.282	4.100	2.524
		3054	850	197	1671	2.432	15,622	9240	0.23	6.888	4.266	2.798
		6474	850	197	2811	2.433	15,889	9424	0.23	7.155	4.395	2.912
		9993	848	197	3981	2.434	15,960	9528	0.22	7.283	4.383	2.977
		552	1502	200	1486	2.434	15,374	9174	0.22	6.754	4.071	2.760
		2920	1500	200	2273	2.435	15,694	9364	0.22	7.040	4.245	2.877
		7688	1500	200	3862	2.436	15,906	9527	0.22	7.269	4.331	2.979
		12,275	1500	200	5391	2.435	15,976	9563	0.22	7.327	4.375	3.001
		14,774	1500	200	6224	2.433	16,019	9463	0.23	7.234	4.499	2.936
		484	2149	200	2110	2.436	15,450	9321	0.21	6.923	4.032	2.852
		2703	2149	197	2853	2.437	15,633	9384	0.22	7.044	4.169	2.891
		7175	2151	197	4346	2.437	15,843	9524	0.22	7.251	4.271	2.979
		11,648	2149	200	5831	2.437	15,972	9498	0.23	7.265	4.427	2.962
		15,643	2151	200	7166	2.436	15,984	9474	0.23	7.242	4.458	2.946
		17,271	2151	200	7708	2.431	15,910	9292	0.24	7.022	4.521	2.829
		7439	2149	200	4428	2.348	15,018	8464	0.27	5.745	4.114	2.267

Well	Sample ID Depth (m) Lithology	Axial Stress Difference (psi)	Confining Pressure (psi)	Pore Pressure (psi)	Effective Mean Stress (psi)	As-Tested Density (g/cm^3)	P-Wave Velocity (ft/s)	S-Wave Velocity (ft/s)	Poisson's Ratio	Young's Modulus (10^6 psi)	Bulk Modulus (10^6 psi)	Shear Modulus (10^6 psi)
Condabri-21	CB21-21 As-received 917.83 Mudstone	2	855	0	856	2.387	9143	6089	0.10	2.627	1.099	1.193
		554	855	0	1040	2.388	9311	6127	0.12	2.701	1.179	1.208
		1032	855	0	1199	2.389	9445	6153	0.13	2.757	1.247	1.219
		1809	855	0	1458	2.390	9675	6175	0.16	2.840	1.377	1.228
		2797	855	0	1787	2.391	9988	6220	0.18	2.950	1.553	1.247
		4264	855	0	2277	2.393	10,261	6252	0.20	3.038	1.715	1.261
		5654	855	0	2740	2.395	10,508	6266	0.22	3.102	1.874	1.267
		201	1705	0	1772	2.394	10,055	6231	0.19	2.977	1.592	1.253
		967	1705	0	2027	2.395	10,061	6240	0.19	2.984	1.591	1.257
		1719	1705	0	2278	2.396	10,165	6222	0.20	3.000	1.669	1.250
		2598	1705	0	2571	2.396	10,285	6245	0.21	3.043	1.737	1.259
		3403	1705	0	2839	2.397	10,452	6270	0.22	3.096	1.835	1.270
		5622	1705	0	3579	2.399	10,692	6314	0.23	3.175	1.977	1.288
		7124	1705	0	4080	2.400	10,797	6316	0.24	3.199	2.050	1.290
		253	2560	0	2644	2.399	10,350	6323	0.20	3.108	1.740	1.293
		1431	2560	0	3037	2.400	10,422	6289	0.21	3.105	1.807	1.279
		2284	2560	0	3321	2.401	10,491	6306	0.22	3.132	1.845	1.287
		4587	2560	0	4089	2.403	10,769	6364	0.23	3.230	2.006	1.311
		5741	2560	0	4474	2.403	10,867	6387	0.24	3.266	2.063	1.321
		8119	2560	0	5266	2.405	11,022	6404	0.25	3.309	2.164	1.329
		5486	2560	0	4389	2.380	10,850	6247	0.25	3.134	2.107	1.252

Well	Sample ID Depth (m) Lithology	Axial Stress Difference (psi)	Confining Pressure (psi)	Pore Pressure (psi)	Effective Mean Stress (psi)	As-Tested Density (g/cm^3)	P-Wave Velocity (ft/s)	S-Wave Velocity (ft/s)	Poisson's Ratio	Young's Modulus (10^6 psi)	Bulk Modulus (10^6 psi)	Shear Modulus (10^6 psi)
Condabri-21	CB21-22 Brine Saturated 917.83 Mudstone	263	1051	200	939	2.434	9966	6138	0.19	2.952	1.610	1.236
		2674	1054	200	1745	2.439	10,431	6230	0.22	3.120	1.876	1.276
		3159	1051	200	1904	2.440	10,492	6246	0.23	3.144	1.909	1.283
		4499	1054	200	2353	2.443	10,651	6273	0.23	3.198	2.007	1.295
		6206	1051	197	2923	2.446	10,846	6265	0.25	3.233	2.153	1.293
		477	1904	200	1863	2.443	10,555	6226	0.23	3.146	1.965	1.276
		1850	1901	200	2318	2.444	10,668	6257	0.24	3.192	2.029	1.289
		2653	1904	197	2591	2.445	10,731	6278	0.24	3.220	2.063	1.298
		3474	1904	200	2862	2.446	10,767	6298	0.24	3.242	2.078	1.307
		4847	1901	197	3319	2.447	10,928	6327	0.25	3.295	2.178	1.320
		6973	1904	197	4031	2.450	11,064	6339	0.26	3.332	2.272	1.327
		473	2759	200	2717	2.448	10,741	6293	0.24	3.236	2.063	1.306
		2181	2759	200	3286	2.449	10,872	6320	0.24	3.282	2.143	1.318
		3805	2756	200	3825	2.451	10,990	6351	0.25	3.329	2.213	1.332
		4508	2759	200	4062	2.452	11,059	6363	0.25	3.350	2.257	1.337
		5228	2756	200	4299	2.452	11,112	6370	0.26	3.367	2.292	1.341
		6550	2756	200	4740	2.454	11,190	6381	0.26	3.390	2.345	1.346
		7287	2756	200	4986	2.454	11,245	6387	0.26	3.405	2.383	1.349
		8057	2759	200	5245	2.455	11,295	6391	0.26	3.418	2.419	1.352
		9246	2756	200	5638	2.458	11,339	6368	0.27	3.410	2.467	1.343
		6182	2759	200	4620	2.452	11,107	6259	0.27	3.281	2.351	1.294

Well	Sample ID Depth (m) Lithology	Axial Stress Difference (psi)	Confining Pressure (psi)	Pore Pressure (psi)	Effective Mean Stress (psi)	As-Tested Density (g/cm^3)	P-Wave Velocity (ft/s)	S-Wave Velocity (ft/s)	Poisson's Ratio	Young's Modulus (10^6 psi)	Bulk Modulus (10^6 psi)	Shear Modulus (10^6 psi)
Condabri-21	CB21-26 Brine Saturated 1053.88 Sandstone	27	1179	200	988	2.601	13,423	8323	0.19	5.768	3.078	2.428
		1183	1181	200	1375	2.603	13,539	8332	0.20	5.820	3.183	2.435
		3686	1181	200	2210	2.605	13,780	8407	0.20	5.971	3.357	2.481
		6704	1181	200	3216	2.607	14,031	8486	0.21	6.129	3.542	2.529
		9464	1181	200	4136	2.608	14,292	8535	0.22	6.261	3.765	2.560
		11,807	1181	202	4914	2.609	14,443	8561	0.23	6.335	3.898	2.577
		13,830	1179	200	5588	2.610	14,596	8564	0.24	6.384	4.055	2.579
		472	2161	200	2118	2.607	13,732	8376	0.20	5.934	3.338	2.465
		2462	2159	202	2777	2.608	13,876	8410	0.21	6.013	3.452	2.485
		5865	2161	200	3916	2.610	14,222	8494	0.22	6.204	3.730	2.537
		9267	2159	200	5048	2.611	14,467	8555	0.23	6.339	3.930	2.575
		12,670	2159	200	6182	2.612	14,646	8575	0.24	6.414	4.099	2.588
		15,302	2161	200	7062	2.613	14,805	8593	0.25	6.479	4.251	2.600
		532	3139	200	3116	2.610	13,986	8446	0.21	6.086	3.534	2.509
		3260	3141	200	4028	2.611	14,155	8496	0.22	6.188	3.663	2.539
		6759	3139	200	5192	2.613	14,468	8556	0.23	6.345	3.933	2.577
		10,290	3139	200	6369	2.614	14,648	8597	0.24	6.441	4.086	2.603
		13,693	3141	200	7505	2.615	14,683	8624	0.24	6.481	4.102	2.620
		16,646	3136	200	8485	2.616	14,791	8642	0.24	6.533	4.201	2.632
		18,957	3139	200	9258	2.617	14,888	8602	0.25	6.521	4.338	2.610
		8717	3139	200	5844	2.598	14,818	8371	0.27	6.210	4.417	2.453

Well	Sample ID Depth (m) Lithology	Axial Stress Difference (psi)	Confining Pressure (psi)	Pore Pressure (psi)	Effective Mean Stress (psi)	As-Tested Density (g/cm^3)	P-Wave Velocity (ft/s)	S-Wave Velocity (ft/s)	Poisson's Ratio	Young's Modulus (10^6 psi)	Bulk Modulus (10^6 psi)	Shear Modulus (10^6 psi)
Condabri-140	CB140-3 Brine Saturated 585.48 Sandstone	988	744	199	874	2.560	14,224	9192	0.14	6.655	3.094	2.915
		4404	744	200	2012	2.562	15,094	9407	0.18	7.225	3.793	3.055
		8718	743	200	3449	2.564	15,436	9503	0.19	7.455	4.072	3.119
		12,973	745	200	4869	2.565	15,677	9514	0.21	7.562	4.323	3.129
		16,747	744	201	6125	2.566	15,778	9505	0.22	7.591	4.443	3.123
		506	1289	201	1256	2.563	14,602	9233	0.17	6.870	3.437	2.944
		3732	1288	202	2330	2.564	15,086	9349	0.19	7.175	3.835	3.019
		8560	1287	202	3938	2.565	15,484	9476	0.20	7.451	4.148	3.103
		13,469	1287	202	5575	2.566	15,697	9477	0.21	7.534	4.379	3.105
		18,211	1289	202	7158	2.567	15,828	9478	0.22	7.584	4.522	3.107
		19,426	1289	202	7562	2.567	15,878	9461	0.22	7.583	4.591	3.096
		505	1827	202	1793	2.563	14,776	9281	0.17	6.987	3.574	2.975
		5042	1828	201	3307	2.565	15,268	9448	0.19	7.341	3.942	3.085
		9807	1829	202	4896	2.566	15,589	9471	0.21	7.489	4.268	3.101
		14,590	1829	202	6491	2.567	15,806	9461	0.22	7.559	4.513	3.096
		19,314	1830	201	8068	2.568	15,939	9483	0.23	7.629	4.641	3.111
		22,740	1829	202	9207	2.568	15,983	9442	0.23	7.601	4.726	3.085
		24,280	1829	202	9721	2.564	15,772	9268	0.24	7.338	4.638	2.968
		8229	1829	202	4370	2.534	15,188	8679	0.26	6.469	4.447	2.572

Well	Sample ID Depth (m) Lithology	Axial Stress Difference (psi)	Confining Pressure (psi)	Pore Pressure (psi)	Effective Mean Stress (psi)	As-Tested Density (g/cm^3)	P-Wave Velocity (ft/s)	S-Wave Velocity (ft/s)	Poisson's Ratio	Young's Modulus (10^6 psi)	Bulk Modulus (10^6 psi)	Shear Modulus (10^6 psi)
Condabri-140	CB140-14 Brine Saturated 709.95 Mudstone	1742	852	194	1239	2.384	8779	5702	0.14	2.371	1.083	1.044
		2972	851	194	1648	2.387	9074	5724	0.17	2.465	1.244	1.054
		3366	851	195	1779	2.389	9191	5752	0.18	2.509	1.299	1.065
		4120	852	194	2031	2.390	9274	5778	0.18	2.544	1.336	1.075
		5426	851	195	2465	2.394	9623	5830	0.21	2.654	1.526	1.096
		507	1519	193	1495	2.391	9189	5747	0.18	2.508	1.301	1.064
		2221	1519	193	2066	2.393	9336	5781	0.19	2.562	1.373	1.078
		3519	1520	193	2500	2.395	9532	5815	0.20	2.627	1.477	1.091
		4674	1520	194	2884	2.396	9667	5858	0.21	2.682	1.540	1.108
		5688	1520	194	3222	2.398	9807	5872	0.22	2.720	1.622	1.114
		6688	1520	193	3556	2.401	9933	5900	0.23	2.764	1.690	1.126
		7000	1520	193	3660	2.402	9983	5919	0.23	2.787	1.713	1.134
		508	2169	193	2145	2.396	9561	5853	0.20	2.655	1.477	1.106
		2367	2169	193	2765	2.398	9686	5859	0.21	2.687	1.553	1.109
		4290	2169	193	3406	2.401	9832	5895	0.22	2.742	1.629	1.124
		5382	2169	193	3770	2.403	9953	5926	0.23	2.786	1.691	1.137
		6363	2168	193	4096	2.404	10,039	5949	0.23	2.819	1.736	1.147
		7379	2169	193	4435	2.407	10,134	5973	0.23	2.855	1.787	1.157
		8473	2169	194	4800	2.411	10,244	5961	0.24	2.872	1.870	1.154
		6922	2169	194	4282	2.405	10,093	5813	0.25	2.742	1.841	1.095

Well	Sample ID Depth (m) Lithology	Axial Stress Difference (psi)	Confining Pressure (psi)	Pore Pressure (psi)	Effective Mean Stress (psi)	As-Tested Density (g/cm^3)	P-Wave Velocity (ft/s)	S-Wave Velocity (ft/s)	Poisson's Ratio	Young's Modulus (10^6 psi)	Bulk Modulus (10^6 psi)	Shear Modulus (10^6 psi)
Condabri-140	CB140-25[27] Brine Saturated 917.50 Sandstone	1390	853	197	1119	2.257	10,432	6507	0.18	3.043	1.593	1.287
		2706	852	197	1558	2.258	10,821	6675	0.19	3.235	1.756	1.356
		4145	852	196	2037	2.260	11,050	6764	0.20	3.344	1.861	1.393
		5485	852	197	2484	2.261	11,141	6779	0.21	3.376	1.914	1.400
		6555	853	195	2843	2.261	11,174	6783	0.21	3.387	1.935	1.402
		507	1697	196	1670	2.262	10,700	6671	0.18	3.207	1.681	1.356
		1970	1698	195	2159	2.263	10,955	6745	0.19	3.315	1.810	1.387
		3750	1698	194	2753	2.264	11,132	6831	0.20	3.411	1.882	1.424
		5457	1697	194	3321	2.265	11,224	6863	0.20	3.455	1.928	1.438
		6880	1698	195	3796	2.266	11,318	6890	0.21	3.495	1.979	1.449
		7880	1699	196	4130	2.267	11,291	6866	0.21	3.475	1.974	1.440
		507	2554	195	2528	2.266	10,786	6750	0.18	3.278	1.698	1.391
		2076	2554	193	3053	2.267	10,945	6820	0.18	3.361	1.765	1.421
		3826	2554	198	3632	2.269	11,150	6852	0.20	3.435	1.887	1.435
		5483	2555	200	4182	2.270	11,243	6884	0.20	3.479	1.933	1.449
		7049	2554	197	4706	2.271	11,352	6900	0.21	3.516	2.001	1.457
		8301	2556	195	5128	2.271	11,402	6899	0.21	3.529	2.037	1.457
		9634	2549	191	5569	2.271	11,352	6794	0.22	3.449	2.060	1.413
		8303	2554	194	5127	2.202	11,063	6282	0.26	2.955	2.071	1.171

Well	Sample ID Depth (m) Lithology	Axial Stress Difference (psi)	Confining Pressure (psi)	Pore Pressure (psi)	Effective Mean Stress (psi)	As-Tested Density (g/cm^3)	P-Wave Velocity (ft/s)	S-Wave Velocity (ft/s)	Poisson's Ratio	Young's Modulus (10^6 psi)	Bulk Modulus (10^6 psi)	Shear Modulus (10^6 psi)
Condabri-140	CB140-26 Brine Saturated 917.50 Sandstone	30	1053	201	862	2.267	9357	6332	0.08	2.639	1.042	1.224
		405	1057	200	992	2.267	9533	6353	0.10	2.714	1.132	1.233
		1632	1056	200	1400	2.269	10,297	6624	0.15	3.078	1.453	1.342
		3416	1058	195	2001	2.271	10,784	6803	0.17	3.312	1.670	1.416
		5203	1057	198	2593	2.272	11,025	6879	0.18	3.423	1.790	1.449
		6736	1055	198	3102	2.273	11,130	6923	0.18	3.478	1.837	1.468
		7846	1057	198	3475	2.274	11,177	6877	0.20	3.465	1.896	1.449
		502	1896	196	1867	2.273	10,404	6725	0.14	3.161	1.468	1.385
		2563	1896	196	2555	2.274	10,737	6816	0.16	3.310	1.634	1.424
		4481	1897	195	3195	2.276	11,019	6892	0.18	3.434	1.781	1.457
		6316	1896	196	3805	2.277	11,183	6931	0.19	3.502	1.872	1.474
		7937	1897	196	4347	2.278	11,246	6907	0.20	3.506	1.930	1.464
		8931	1896	195	4678	2.279	11,264	6894	0.20	3.505	1.951	1.460
		502	2755	195	2727	2.276	10,605	6807	0.15	3.267	1.554	1.421
		2694	2755	197	3455	2.278	10,824	6861	0.16	3.364	1.670	1.444
		4621	2756	200	4096	2.279	11,068	6921	0.18	3.468	1.801	1.471
		6443	2756	192	4713	2.280	11,218	6954	0.19	3.530	1.886	1.486
		9309	2755	194	5665	2.283	11,316	6940	0.20	3.552	1.964	1.482
		9762	2756	194	5816	2.285	11,335	6887	0.21	3.527	2.009	1.461
		9808	2754	196	5827	2.287	11,323	6869	0.21	3.516	2.013	1.454
		9470	2755	195	5716	2.366	11,082	6401	0.25	3.264	2.173	1.306

References

Aadnoy, B. S., 1990, Inversion technique to determine the in-situ stress field from fracturing data: Journal of Petroleum Science and Engineering, v. 4, p. 127-141.

Barree, R. D., V. L. Barree, and D. Craig, 2007, Holistic fracture diagnostics: Rocky Mountain Oil & Gas Technology Symposium.

Barree, R. D., J. V. Gilbert, and M. Conway, 2009, Stress and rock property profiling for unconventional reservoir stimulation: SPE Hydraulic Fracturing Technology Conference.

Bell, J. S., ed., 1990, The stress regime of the Scotian Shelf offshore eastern Canada to 6 kilometers depth and implications for rock mechanics and hydrocarbon migration: Rock at Great Depth: Rotterdam, Netherlands, Balkemia.

Boult, P. J., E. Lanzilli, B. H. Michaelsen, D. M. McKirdy, and M. J. Ryan, 1998, A New Model for the Hutton/Birkhead Reservoir/Seal Couplet and the Associated Birkhead-Hutton(!) Petroleum System: APPEA Journal, v. 38, p. 724 - 743.

Boyd, R., S. Dewar, A. Aouad, B. Pidgeon, and L. Sammons, 2016, Sedimentology and Stratigraphy of the Walloon Subgroup, Surat Basin, Australia: AAPG Annual Convention and Exhibition.

Bradshaw, M., and M. Yeung, 1992, Palaeogeographic Atlas of Australia.

Brakel, A. T., T. J.M., A. T. Wells, and M. G. Nicoll, 2009, Sequence stratigraphy and fill history of the Bowen Basin, Queensland: Australian Journal of Earth Sciences, v. 56, p. 401 - 432.

Brooke-Barnett, S., T. Flottmann, P. K. Paul, S. Busetti, R. Hennings, and R. Reid, 2012, Influence of basement structures on stress regimes in the Surat and Bowen Basins, southeast Queensland, Eastern Australian Basin Symposium IV, Brisbane, QLD, p. 4.

Brooke‐Barnett, S., T. Flottmann, P. K. Paul, S. Busetti, P. Hennings, R. Reid, and G. Rosenbaum, 2015, Influence of basement structures on in situ stresses over the Surat Basin, southeast Queensland: Journal of Geophysical Research: Solid Earth, v. 120, p 4946-4965.

Brudy, M., and M. Zoback, 1999, Drilling-induced tensile wall-fractures: implications for determination of in-situ stress orientation and magnitude: International Journal of Rock Mechanics and Mining Sciences, v. 36, p. 191-215.

Caritat, P. D., and J. Braun, 1992, Cyclic Development of Sedimentary Basins at Convergent Plate Margins - 1. Structural and Tectono-Thermal Evolution of Some Gondwana Basins of Eastern Australia: Journal of Geodynamics, v. 16, p. 241 - 282.

Cook, A. G., and J. J. Draper, 2013, Surat Basin, *in* P. A. Jell, ed., Geology of Queensland: Brisbane, Queensland, Geological Survey of Queensland, p. 533 - 539.

Crain, E., 2002, Crain's petrophysical handbook, Spectrum 2000 Mindware Limited.

Crain, E. R., 2008, Crain's Petrophysical Handbook, Rocky Mountain House, Alberta Canada.

Deer, W. A., R. A. Howie, and J. Zussman, 1992, An Introduction to the Rock Forming Minerals, Longman.

Donchak, P. J. T., 2013, New England Orogen, *in* P. A. Jell, ed., Geology of Queensland, Queensland Government, p. 468 - 470.

Dowla, N., A. Hayatdavoudi, A. Ghalambor, C. Okoye, and C. Alcocer, 1990, Laboratory investigation of saturation effect on mechanical properties of rocks: SPWLA 31st Annual Logging Symposium.

Elliott, L. G., 1989, The Surat and Bowen Basins: APEA Journal 1989, v. 29, p. 398 - 416.

Elliott, L. G., 1993, Post-Carboniferous Tectonic Evolution of Eastern Australia: APEA Journal 1993, p. 215 - 236.

Ellis, D., and J. Singer, 2007, Well Logging for Earth Scientists: The Netherlands, Springer, 692 p.

Exon, N., and D. Burger, 1981, Sedimentary cycles in the Surat Basin and global changes of sea level: Bureau of Mineral Resources Journal of Australian Geology and Geophysics, v. 6, p. 153-159.

Exon, N. F., 1976, Geology of the Surat Basin in Queensland: Bureau of Mineral Resources Bulletin, v. 166.

Exon, N. F., and B. R. Senior, 1976, The Cretaceous of the Eromanga and Surat Basins: BMR Journal of Australian Geology and Geophysics, v. 1, p. 33 - 50.

Fielding, C. R., 1993, Middle Jurassic Walloon Coal Measures in the Type Area, the Rosewood-Walloon Coalfield, SE Queensland: Australian Coal Geology, v. 9, p. 4 - 16.

Fielding, C. R., 1996, Mesozoic Sedimentary Basins and Resources in Eastern Australia - A Review of Current Understanding: Geological Society of Australia, v. 43, p. 180 - 185.

Fielding, C. R., A. R. G. Gray, G. I. Harris, and J. A. Salomon, 1990, The Bowen Basin and overlying Surat Basin. *In Finlayson* D.M. *ed. The Eromanga-Brisbane Geoscience Transect: a guide to basin development across Phanerozoic Australia in southern Queensland.* : Bureau of Mineral Resources, Geology and Geophysics, Bulletin., v. 232, p. 105 - 116.

Fielding, C. R., J. Kassan, and J. J. Draper, 1996, Geology of the Bowen and Surat Basins, Eastern Queensland: Australasian Sedimentologists Group Field Guide Series No. 8: Brisbane, Conference Publications.

Fjaer, E., R. M. Holt, P. Horsrud, A. M. Raaen, and R. Risnes, 2008, Petroleum Related Rock Mechanics (Second Edition).

Flottmann, T., S. Brooke-Barnett, R. Trubshaw, S. K. Naidu, E. Kirk-Burnnand, P. Paul, S. Busetti, and P. Hennings, 2013, Influence of In-Situ Stresses on Fracture Stimulations in the Surat Basin, Southeast Queensland, SPE Unconventional Resources Conference and Exhibition - Asia Pacific, Brisbane, Australia, Society of Petroleum Engineers, p. 14.

Fossen, H., 2010, Structural Geology: New York, USA, Cambridge University Press, 463 p.

Gallagher, K., 1990, Permian to Cretaceous subsidence history along the Eromanga-Brisbane Geoscience Transect. *In Finlayson* D.M. *ed. The Eromanga-Brisbane Geoscience Transect: a guide to basin development across Phanerozoic Australia in southern Queensland.*: Bureau of Mineral Resources, Geology and Geophysics, Australia, v. Bulletin 232, p. 133 - 151.

Gallagher, K., T. A. Dumitru, and A. J. W. Gleadow, 1994, Constraints on the vertical motion of eastern Australia during the Mesozoic.: Basin Research, v. 6, p. 77 - 94.

Gough, D., and J. Bell, 1982, Stress orientations from borehole wall fractures with examples from Colorado, east Texas, and northern Canada: Canadian Journal of Earth Sciences, v. 19, p. 1358-1370.

Green, P., K. L. Hoffmann, T. J. Brain, A. R. G. Gray, and C. G. Murray, 1997, The Surat and Bowen Basins, south-east Queensland.: Queensland Minerals and Energy Review Series.

Guinebretière, R., 2013, X-ray diffraction by polycrystalline materials, John Wiley & Sons.

Hamilton, S. K., J. S. Esterle, and R. Sliwa, 2014, Stratigraphic and depositional framework of the Walloon Subgroup, eastern Surat Basin, Queensland: Australian Journal of Earth Sciences.

Harrington, H. J., 1989, Permian coals of eastern Australia, Australian Government Publishing Service.

Hawlader, H. M., 1990, Diagenesis and reservoir potential of volcanogenic sandstones - Cretaceous of the Surat Basin, Australia: Sedimentary Geology, v. 66, p. 181 - 195.

He, F., and P. J. Conaghan, 1994, Diagensis of Jurassic and Lower Cretaceous sandstones of the Eromanga Basin in New South Wales: AGSO Journal of Australia Geology and Geophysics, v. 15, p. 191 - 215.

Hillis, R. R., and S. D. Reynolds, 2003, In situ stress field of Australia: Geological Society of Australia Special Publication, v. 22, p. 49 - 58.

Hoffman, K. L., J. M. Totterdell, O. Dixon, G. A. Simpson, A. T. Brakel, A. T. Wells, and J. L. Mckellar, 2009, Sequence Stratigraphy of Jurassic Strata in the lower Surat Basin succession, Queensland: Australian Journal of Earth Sciences, v. 56, p. 461 - 476.

Holcombe, R., C. Stephens, C. Fielding, D. Gust, T. Little, R. Sliwa, J. McPhie, and A. Ewart, 1997, Tectonic evolution of the northern New England Fold Belt: Carboniferous to Early Permian transition from active accretion to extension, v. 19, Special Publication of the Geological Society of Australia.

Holcombe, R. J., 2013, Cross sections showing tectonic evolution of the northern New England Orogen during Devonian - Jurassic *in* P. A. Jell, ed., Geology of Queensland: Brisbane, Queensland, Geological Survey of Queensland, p. 469.

Hubbert, M. K., and D. G. Willis, 1957, Mechanics of hydraulic fracturing: Trans. Soc. Pet. Eng. AIME, v. 210, p. 153 - 163.

Jaeger, J., and N. Cook, 1979, Fundamentals of rock mechanics, 2nd edition, Chapman and Hall, New York, 593 p.

Jell, P. A., ed., 2013, Geology of Queensland: Queensland, State of Queensland.

Jell, P. A., J. J. Draper, and J. McKellar, 2013, Great Australian Superbasin, *in* P. A. Jell, ed., Geology of Queensland: Brisbane, Queensland, Geological Survey of Queensland, p. 516 - 517.

Jones, G. D., and R. B. Patrick, 1981, Stratigraphy and coal exploration geology of the northeast Surat Basin: Coal Geology, Journal of the Coal Geology Group, Geological Society of Australia, v. 1, p. 153-163.

Khaksar, A., A. Younessi, and M. Jami, 2015, Prediction and Management of Solids Production in Typical Surat Basin Coal Seam Gas Reservoirs, Eastern Australia.: APPEA Conference 2015.

Kirsch, E. G., 1898, Die theorie der elastizität und die bedürfnisse der festigkeitslehre, Springer.

Korsch, R., C. J. Boreham, J. M. Totterdell, R. D. Shaw, and M. G. Nicoll, 1998, Development and petroleum resource evaluation of the Bowen, Gunnedah and Surat Basins, Eastern Australia: The APPEA Journal, v. 38, p. 199-237.

Korsch, R. J., and J. M. Totterdell, 2009, Subsidence history and basin phases of the Bowen, Gunnedah and Surat Basins, eastern Australia: Australian Journal of Earth Sciences, v. 56, p. 335 - 353.

Korsch, R. J., J. M. Totterdell, D. L. Cathro, and M. G. Nicoll, 2009a, Early Permian East Australian Rift System: Australian Journal of Earth Sciences, v. 56, p. 381 - 400.

Korsch, R. J., J. M. Totterdell, T. Fomin, and M. G. Nicoll, 2009b, Contractional structures and deformational events in the Bowen, Gunnedah and Surat Basins, eastern Australia: Australian Journal of Earth Sciences, v. 56, p. 477 - 499.

Leblang, G. M., P. A. Rayment, and M. Smyth, 1981, The Austinvale coal deposit - Wandoan. A palaeoenvironmental analysis: Geological Society of Australia, Coal Geology Group Journal, v. 1, p. 185 - 195.

Lillie, R., 1999, Whole Earth Geophysics: An Introductory Textbook for Geologists and Geophysicists, 361 p.

Martin, M. A., M. Wakefield, M. K. MacPhail, T. Pearce, and H. E. Edwards, 2013, Sedimentology and stratigraphy of an intra-cratonic basin coal seam gas play: Walloon Subgroup of the Surat Basin, eastern Australia: Petroleum Geoscience, v. 19, p. 21 - 38.

Mastin, L., 1988, Effect of borehole deviation on breakout orientations: Journal of Geophysical Research: Solid Earth, v. 93, p. 9187-9195.

McKellar, 1998, Late Early to Late Jurassic Palynology, Biostratigraphy and Palaeogeography of the Roma Shelf Area, Northwest Surat Basin, Queensland, Australia, University of Queensland, Brisbane.

McNally, G. H. N., 1987, Estimation of coal measures rock strength using sonic and neutron logs: Geoexploration, v. 24, p. 381-395.

Moos, D., and M. D. Zoback, 1990, Utilization of observations of well bore failure to constrain the orientation and magnitude of crustal stresses: application to continental, Deep Sea Drilling Project, and Ocean Drilling Program boreholes: Journal of Geophysical Research: Solid Earth, v. 95, p. 9305-9325.

Morton-Thompson, D., and A. M. Woods, 1993, Development Geology Reference Manual: AAPG Methods in Exploration Series, No. 10, AAPG.

Murphy, A., 2012, Greater Talinga Area Stratigraphic Study, Origin Energy Internal Report: APLNG, Brisbane, Origin Energy.

Murray, C. G., 1997, Basement Terranes Beneath the Bowen and Surat Basins, Queensland, *in* P. M. Green, ed., The Surat and Bowen Basins, south-east Queensland. Queensland Minerals and Energy Review Series: Brisbane, Queensland, Queensland Department of Mines and Energy.

Olsen, T., R. Steel, K. Hogseth, T. Skar, and S. L. Roe, 1995, Sequential Architecture in a fluvial succession: sequence stratigraphy in the Upper Cretaceous Mesaverde Group, Price Canyon, Utah.: Journal of Sedimentary Research, v. B65, p. 265 - 280.

Pidgeon, B., 2012, Walloons Coal Measures Deposition Model, Origin Energy Internal Report.

Plumb, R. A., 1994, Influence of composition and texture on the failure properties of clastic rocks: Society of Petroleum Engineers, p. 13 - 20.

Power, P. E., and S. B. Devine, 1970, Surat Basin, Australia - Subsurface Stratigraphy, History and Petroleum: AAPG, v. 54, p. 28.

Qui, K., J. R. Marsden, J. Alexander, A. Retnanto, A. O. Abdelkarim, and M. Shatwan, 2006, Practical Approach to Achieve Accuracy In Sanding Prediction: Society of Petroleum Engineers.

Rahmati, H., M. Jafarpour, S. Azadbakht, A. Nouri, H. Vaziri, D. Chan, and Y. Xiao, 2013, Review of sand production prediction models: Journal of Petroleum Engineering, v. 2013.

Rajabi, M., M. Tingay, O. Heidbach, R. Hillis, and S. Reynolds, 2017, The present-day stress field of Australia: Earth-Science Reviews.

Richardson, R. M., 1992, Ridge forces, absolute plate motions, and the intraplate stress field: Journal of Geophysical Research: Solid Earth, v. 97, p. 11739-11748.

Rider, M., and M. Kennedy, 2011, The Geological Interpretation of Well Logs (Third Edition): Third Edition: Scotland, Rider-French Consulting Ltd.

Rohead-O'Brien, H., 2011, Reservoir Quality of the Tangalooma Sandstone, Walloon Coal Measures - Surat Basin, Queensland: A Lithological and Compositional Investigation: Research thesis, The University of Adelaide, Adelaide, Australia, 81 p.

Sandiford, M., 2016, http://jaeger.earthsci.unimelb.edu.au/Images/images.html..

Scott, S. G., 2008, The geology, stratigraphy and coal seam gas characteristics of the Walloon subgroup-northeastern Surat Basin, James Cook University.

Scott, S. G., B. Anderson, P. Crosdale, J. Dingwall, and G. Leblang, 2004, Revised geology and coal seam gas characteristics of the Walloon Subgroup - Surat Basin, Queensland: Eastern Australasian Basins Symposium II, p. 345 - 355.

SEEBASE™, O., 2005, Study 2005: FrOG Tech Pty Ltd.

Shanley, K. W., and P. J. McCabe, 1994, Perspectives on the sequence stratigraphy of continental strata: AAPG Bulletin, v. 78, p. 544 - 568.

Swarbrick, C. F. J., 1973, Stratigraphy and Economic Potential of the Injune Creek Group in the Surat Basin: Geological Survey of Queensland, v. Report 79.

Tavener, E., T. Flottmann, and S. Brooke-Barnett, 2017, In situ stress distribution and mechanical stratigraphy in the Bowen and Surat basins, Queensland, Australia: Geological Society, London, Special Publications, v. 458, p. 31-47.

Thiercelin, M. J., and R. A. Plumb, 1994, Core-Based Predictions of Lithologic Stress Contrasts in East Texas Formations: Society of Petroleum Engineers, v. 21847.

Turner, S., L. B. Bean, M. Dettmann, J. L. McKellar, S. McLoughlin, and T. Thulborn, 2009, Australian Jurassic sedimentary and fossil successions: current work and future prospects for marine and non-marine correlation: GFF, v. 131, p. 49-70.

Twiss, R. J., and E. M. Moores, 2007, Structural Geology (Second Edition): United States of America, Susan Finnemore Brennan.

Veevers, J. J., 1984, Phanerozoic earth history of Australia: Oxford, Clarendon Press.

Veevers, J. J., J. G. Jones, and C. M. Powell, 1982, Tectonic Framework of Australia's sedimentary basins.: The APEA Journal, v. 22, p. 283 - 300.

Walsh, J., S. Bose, B. Sinha, S. Sunaga, T. Endo, and H. Valero, 2010, A dispersion-based method for measuring dipole shear anisotropy: SPWLA 51st Annual Logging Symposium.

Waschbusch, P., R. J. Korsch, and C. Beaumont, 2009, Geodynamic modelling of aspects of the Bowen, Gunnedah, Surat and Eromanga Basins from the perspective of convergent margin processes: Australian Journal of Earth Sciences, v. 56, p. 309 - 334.

Waseda, Y., E. Matsubara, and K. Shinoda, 2011, X-ray diffraction crystallography: introduction, examples and solved problems, Springer Science & Business Media.

Yago, J. V. R., 1996, Basin Analysis of the Middle Jurassic Walloon Coal Measures in the Great Artesian Basin, Australia, University of Queensland, 69 p.

Yago, J. V. R., and C. R. Fielding, 1996, Sedimentology of the Middle Jurassic Walloon Coal Measures in the Great Artesian Basin, eastern Australia, Mesozoic geology of the eastern Australia Plate Conference, Brisbane, Geological Society of Australia, p. 574 - 575.

Zeinijahromi, A., A. Vaz, and P. Bedrikovetsky, 2012, Well impairment by fines migration in gas fields: Journal of Petroleum Science and Engineering, v. 88 - 89, p. 125 - 135.

Zhang, J., and L. Bentley, 2005, Factors determining Poisson's ratio, CREWES Research Report.

Zoback, M., 2007, Reservoir Geomechanics, Cambridge University Press.

Zoback, M. D., D. Moos, L. Mastin, and R. N. Anderson, 1985, Well bore breakouts and in situ stress.